Thesis

Tests of Lorentz Invariance with an Optical Ring Cavity

Yuta Michimura

Department of Physics
University of Tokyo

October 2014

Abstract

A search for Lorentz violation in electrodynamics was performed by measuring the resonant frequency difference between two counterpropagating directions of an optical ring cavity. Our cavity contains a dielectric element, which makes our cavity sensitive to the parity-odd violations. The laser frequency is stabilized to the counterclockwise resonance of the cavity, and the transmitted light is reflected back into the cavity for resonant frequency comparison with the clockwise resonance. This double-pass configuration enables a null experiment and gives high common mode rejection of environmental disturbances.

The cavity was rotated to modulate the Lorentz violation signal. From the analysis of a year-long observational data containing 1.7 million cavity rotations, we found no evidence for dipole and hexapole components of anisotropy at the level of $\delta c/c \lesssim 10^{-15}$. This result was more than an order of magnitude stringent than previous best cavity limits, and was the first limit on hexapole components.

Within the framework of the Standard Model Extension (SME), our result put the first constraints on parity-odd higher order Lorentz violations. Absolute sensitivity to the SME camouflage coefficients $(\overline{c}_F^{(d)})_{jlm}^{(0E)}$ of dimension 6 is improved by a factor of a million over existing parity-even microwave cavity bounds. Sensitivity to dimension 8 violations is improved by 14 orders of magnitude.

Thesis Supervisor: Masaki Ando (Associate Professor)
Thesis Title: Tests of Lorentz Invariance with an Optical Ring Cavity

要旨

光リング共振器の時計回りの共振周波数と反時計回りの共振周波数を比較することで、電磁気学における Lorentz 不変性の破れの探査を行った。我々の共振器には光路の一部に屈折率を変える媒質が入っており、これによって奇パリティな Lorentz 不変性の破れに感度を持たせた。共振器に入射するレーザー光の周波数は反時計回りの共振周波数に安定化し、共振器の透過光を打ち返して再入射することで時計回りの共振周波数との差を取る。このダブルパス構成により本実験は null 測定になっている。また、この構成では環境変動に伴う雑音に対し、高い同相雑音除去が効くため、優れた構成になっている。

我々は共振器を回転させることで、Lorentz 不変性の破れ信号を変調した。1 年に渡る 1.7×10^6 回転分の観測データの解析を行ったが、$\delta c/c \lesssim 10^{-15}$ の精度で、異方性の双極子成分と六重極成分が存在するという証拠は見つからなかった。この結果は、これまでの共振器による上限値に比べて 1 桁以上厳しいものである。また、六重極成分に対しては初めての上限値である。

拡張標準理論 (SME) の枠組みでは、我々の結果は Lorentz 不変性の高次の破れのうち、奇パリティ成分に初の上限値をつけたことになる。既に存在するマイクロ波共振器による偶パリティ成分への上限値に比べて、質量次元 $d = 6$ の SME のカモフラージュ係数 $(\overline{c}_F^{(d)})_{jlm}^{(0E)}$ に対して、6 桁厳しい上限値をつけた。また、$d = 8$ の係数に対しては、14 桁厳しい上限値をつけた。

指導教員: 安東正樹 (准教授)
論文題目: 光リング共振器を用いたローレンツ不変性の検証

Acknowledgements

This work has been supported by a number of people. Here, I wish to express my appreciation for their support.

First of all, I would like to thank my former supervisor Kimio Tsubono for his incredible support. I cannot count how many times I knocked on the door of his office since I proposed to do this experiment. He was always the first person to report the progress and to ask when I cannot decide which way to go. He never presented his thoughts directly, but his advice based on his years of experience in experiments and education was full of implications. Also, whenever I need new things for the experiment, he always let me purchase and I never had serious financial problems. He kept encouraging me even after his retirement. I am proud of being one of his students.

I am greatly obliged to my supervisor Masaki Ando as well. It was his idea which brought the armchair experimental principle into the actual experimental apparatus like this. Historically, this experiment was started from his suggestion to do something interesting with a monolitically assembled optical system. The experimental details have been eventually changed from his original plan, but I might not have got into this world of odd-parity Lorentz violation without his original suggestion. We had countless discussions and emails about the experimental strategy and the data analysis. I also have to thank him for hiring me and waiting for my thesis patiently.

It was very fortunate for me to have many splendid supervisors besides my official supervisors.

Yoichi Aso supervised me since I was an undergraduate student. I firstly learned about optical interferometry, control theory, mechanical system design, scientific computing, and many other experimental techniques from him. When

I consulted him on the experiment, he always gave me exact solutions, or bright ways to specify what is wrong. His rich knowledge and logical way to perform experiments have greatly influenced and inspired me. I also admire his style as a researcher. It was very lucky for me to work with him also in the Japanese gravitational wave detector project KAGRA.

Noriaki Ohmae taught me almost everything – from locking of the cavities to optics manufacturers or drawing software easy to use. He has not only an extensive knowledge, but also a capacity for leadership. I consulted him whenever I had small troubles since I started this experiment. Annoyedly but kindly, he gave me appropriate advice based on his rich experience every time. I also respect him for his quick replies to emails. He gave me a lot of comments and suggestions via emails when revising this thesis. I owe him very much that I almost feel embarrassed.

Alan Kostelecký pointed out the physical meaning of this experiment in his framework of the Standard Model Extension (SME) when I was visiting Indiana University for the Sixth Meeting on CPT and Lorentz Symmetry (CPT'13). The data analysis for the higher order Lorentz violation would not be started without his indication.

Matthew Mewes theoretically analyzed the apparatus in the framework of SME. I have made a lot of emails asking about SME since we first met at CPT'13. His answers were always clear even for experimentalists, and discussions with him were essential for this thesis. He also gave me a lot of information about the theoretical background and motivation for this work. It was a nice experience for me to write a paper with him. I am glad to meet him at CPT'13 and being able to start collaborating with him.

Shigemi Otsuka and Yoshikatsu Nanjo from the machine shop made many special parts needed for this experiment. They were impressively quick at making things and I never had to delay the schedule waiting for them. I occasionally had to hurry up because they were so quick. They also gave me advice when designing and redesigning some parts. I'm filled with gratitude for their kind support.

Norikatsu Mio gave me helpful information about the bidirectional optical cavity, based on his experience with similar experiments. I am also thankful to him for his valuable comments on the physical meaning of this experiment.

Shigenori Hiramatsu gave me useful suggestions about the power circuit for the motor. He often encouraged me when he was a visiting researcher at our group and it was also helpful for me.

I appreciate invaluable comments and information from many other researchers: Koji Arai, Rana Adhikari, Nicolas Smith-Lefebvre, Evan Hall, Kiwamu Izumi, Akitoshi Ueda, Tomotada Akutsu, Ryutaro Takahashi, Soichiro Isoyama, Kenta Hotokezaka, Atsushi Nishizawa, Kentaro Somiya, Shigenori Moriwaki, Wei-Tou Ni, Stephan Schiller, Ralf Lehnert, Kent Yagi and so on. It was always fun to discuss about my experiment and future prospects with those people.

I also have to thank KAGRA collaborators for keeping me away from KAGRA work during the thesis work. I feel especially sorry for Seiji Kawamura, Yoichi Aso, Tomotada Akutsu, and Osamu Miyakawa.

I am also glad to work with many exciting and talented colleagues in our group at the University of Tokyo.

Wataru Kokuyama introduced me the very first paper which stimulated us to do this experiment. At one group meeting, I asked this question: "It would be interesting if we can measure the difference between the speed of light propagating in opposite directions. But are there any way to measure it?" Wataru was the first man to search for some papers and passed me the very first paper. Although he already left our group now, he occasionally gave me some links to interesting papers on this research. If this thesis has somewhat of a wide perspective, that is because of him. He always gave positive response to my experiment, and it was also reassuring for me.

Nobuyuki Matsumoto helped me developing the optical system and took care of the apparatus when I was going on trips. The year-long observation could not be done without him. He also helped me doing the data analysis. It was fortunate for me to have a controversialist like Nobuyuki. Discussions with him were always suggestive and stimulating.

Kenshi Okada was another man I discussed with a lot. He was always chasing his unlimited dream in his unique approach and his style was very thrilling to me. I also have to thank Kenshi for sponsoring multiple celebration parties for us whenever we reached important milestones.

Ayaka Shoda has something that I don't have, and I learned a lot working with her since we were undergraduate students. I think it is a rare good luck that a gifted person like her was in the same year in our group.

I also enjoyed working and discussing with Takafumi Ushiba, Kazunori Shibata, Yuya Kuwahara and Kentaro Komori. Their enthusiasm stimulated me so much. Takafumi put the right amount of pressure on me by frequently asking me about the progress of my thesis. Kazunori helped me when ordering some electrical components.

The office staff members Ami Ito, Michiko Kudoh and Miki Ueda should not be forgotten here. They always supported me by taking care of paperwork when purchasing something, attending meetings, going on trips, and so on. I could concentrate on my research without being overwhelmed by a lot of paperwork because of them. Many staff members from the department office and the faculty office also helped me very much doing paperwork for submitting this thesis.

I appreciate assistance from people from companies as well.

Yasuto Narisawa from Nikkidenso helped me with selecting the appropriate motor for this experiment, and with adjusting the parameters related to the power supply and the motor servo.

People from Okamoto Optics including Yoshiyasu Sasama processed the silicon piece, which was the key to the experiment.

Robert Detulong from Nagase kindly provided a potting agent for filling a hole of the vacuum enclosure.

I also received information and suggestion about selecting products and designing the experimental apparatus from many other people: Tamotsu Tamada, Reo Otani, Toshinobu Matsumoto (Sigma Koki), Toshiyuki Horikoshi, Mikio Sakamoto (Japan Laser), Norihisa Tanaka (Sunplus Trading), Masanori Yamada (Niki Glass), Ryosuke Yamaguchi (THK), Yuki Iezawa (High-Tech), and so on.

This work was financially supported by JSPS Grant-in-Aid for Scientific Research (A) No. 22244049 and Grant-in-Aid for JSPS Fellows No. 25·10386. I also acknowledge financial support from ALPS (Advanced Leading Graduate

Course for Photon Science) program at the University of Tokyo.

Masahiro Teshima, Yasushi Suto, Makoto Minowa, Hirofumi Sakai, and Masato Shiozawa were the reviewers of this thesis. Their comments at the review are quite valuable not only for this thesis, but also for the future research.

Finally, I would like to thank my parents for their continuous encouragement and support.

It is virtually impossible to list up all the supporters of this research. This thesis could not be finished without contribution from everyone, even if some are indirect and obscure. I am grateful to all of you for your support. Thank you.

Contents

Glossary

Symbols

i	imaginary unit $i = \sqrt{-1}$
c	speed of light $c = 299792458$ m/s
h	Planck's constant $h = 6.626 \times 10^{-34}$ Js
k_{B}	Boltzmann constant $k_{\mathrm{B}} = 1.381 \times 10^{-23}$ J/s
e	elementary charge $e = 1.602 \times 10^{-19}$ C
v	speed with respect to the preferred frame
γ	Lorentz factor $\gamma = 1/\sqrt{1 - v^2}$
λ	laser wavelength
ν	laser frequency [Hz] ($\nu = c/\lambda$)
ω	laser angular frequency [rad/sec] ($\omega = 2\pi\nu$)
ω_{rot}	angular frequency of the cavity rotation [rad/sec]
$\omega_{\oplus}$	angular frequency of the Earth's rotation [rad/sec]
$\delta\nu$	cavity resonant frequency difference [Hz]
f	Fourier frequency [Hz]
n	refractive index
L	cavity round-trip (geometric) length
L_{opt}	cavity round-trip optical path length
$\mathcal{F}$	cavity finesse
θ	polar angle in the SCCEF
ϕ	azimuth angle in the SCCEF
χ	colatitude of the laboratory
$T_{\oplus}$	time from the vernal equinox in 2000
m_{r}	harmonic order for the cavity rotational frequency
$m_{\oplus}$	harmonic order for the sidereal frequency
$\overline{y}_l^m$	spherical coefficient
$(\overline{c}_F^{(d)})_{jlm}^{(0E)}$	SME camouflage coefficient
d	mass dimension of SME Lorentz violating operator

Acronyms

ADC	analog-to-digital converter
AR	anti-reflective, anti-reflection
BS	beam splitter
CMB	cosmic microwave background
CMRR	common mode rejection ratio
CPT	charge, parity, and time
DC	direct current
DFB	distributed feedback (laser)
FP	Fabry-Perot (cavity)
FSR	free spectral range
F/V	frequency to voltage
FWHM	full width at half maximum
GPS	global positioning system
HC	Hänsch-Couillaud (method)
HR	high-reflection
HWP	half-wave plate
LV	Lorentz violation
mSME	minimal Standard Model Extension
PBS	polarizing beam splitter
PC	personal computer
PD	photodetector, photodiode
PDH	Pound-Drever-Hall (method)
PI	photo interrupter
PZT	lead zirconate titanate (piezoelectric transducer)
QWP	quarter-wave plate
RMS	root mean square
SCCEF	Sun centered celestial equatorial frame
SME	Standard Model Extension
UGF	unity gain frequency

Chapter 1
Introduction

Special Relativity is based upon two postulates, the special principle of relativity and the principle of the constancy of the speed of light. Starting from these two postulates, Einstein revealed that Lorentz transformation, not Galilean transformation, is the space-time coordinate transformation [1]. Special Relativity was the first theory to propose that Lorentz invariance is the universal symmetry of space-time and is valid not only for the Maxwell's equations of electrodynamics, but also for other laws of physics. Since Einstein's first paper, wide variety of experimental tests have been carried out for more than 100 years, but no one could find any violation [2, 3, 4]. As a consequence, Lorentz invariance underlies all the theories of fundamental interactions, such as the Standard Model of particle physics and General Relativity.

However, theoretical works towards the unification of fundamental interactions, such as string theories or loop quantum gravity, have led to the idea that Lorentz invariance may only be approximate at attainable energies [5, 6, 7]. Also, the observed anisotropy of the cosmic microwave background (CMB) suggests a possible preferred frame in the Universe [8]. We could say that the dipole component of the CMB anisotropy comes from red and blue shifts from our velocity with respect to the CMB rest frame. If the CMB rest frame is the preferred frame, which is denied by Special Relativity, our vision of the Universe will be turned upside down.

There are almost no quantitative predictions at what level we can observe Lorentz violation. For example, Ref. [13] suggests Lorentz violation at 10^{-17} level, but this number only comes from the ratio between the Planck mass and the electroweak scale. Thus, we should perform experimental searches for Lorentz violations with increasing precision. Even if we could not find

any violation within the experimental precision, we can restrict possible new theories.

Here, we test Lorentz invariance by testing the isotropy of the speed of light using an optical ring cavity. Especially, we have tested if the speed of light propagating in one direction and that in the opposite direction are the same. This *one-way* test cannot be done with usual electromagnetic interferometers or cavities used for previous Michelson-Morley type experiments. This is because usual interferometers or cavities have closed paths for electromagnetic wave and can only measure the average speed of light propagating back and forth.

We have solved this problem by placing a piece of dielectric material along one side of the optical path of a triangular optical ring cavity. If there is a difference between the speed of light propagating in opposite directions, the resonant frequencies for the clockwise direction and the counterclockwise direction will be shifted in opposite signs. Thus, we measured the resonant frequency difference between two counterpropagating directions with double-pass configuration to get the Lorentz violation signal. This double-pass configuration enables a null measurement of the resonant frequency difference. Also, this differential measurement is highly insensitive to environmental disturbances because the effects of cavity length fluctuations are common to both resonances.

This thesis is organized as follows: Chapter 2 introduces test theories of Special Relativity and Lorentz invariance, and reviews previous tests of Lorentz invariance, particularly in electrodynamics or photons. Chapter 3 describes the experimental principle of testing Lorentz invariance with an optical ring cavity. Also, noise sources and noise requirements for improving previous upper limits on Lorentz violation are discussed. Chapter 4 describes the experimental setup and shows that our apparatus fulfilled the requirements. Chapter 5 explains how to extract Lorentz violation parameters from the data taken and gives the result of the data analysis. Chapter 6 concludes the results of this work and gives future prospects of this research.

The author of this thesis tried to make this thesis readable for nonexperts of the Standard Model Extension. Details of the analysis within the frame

work of the Standard Model Extension are described in Appendix A.

We note here that the tests of Lorentz invariance in photons have also been done very precicely with gamma ray astronomy, taking advantage of cosmological distances. From polarization measurements and light-curve measurements of light from gamma ray burts, there are tight constraints on the vacuum birefringence [56, 64] and the vacuum dispersion [65, 68]. However, anisotropy in the speed of light arises from the different kind of Lorentz violation, which is hard to search with gamma ray astronomy.

The author of this thesis designed and developed the experimental apparatus, performed the year-long observation run, and did the data analysis. Nobuyuki Matsumoto helped developing the optics and kept the laser frequency to be locked during the observation run. Matthew Mewes theoretically analyzed the apparatus in the framework of the Standard Model Extension. Masaki Ando provided the idea of making use of double-pass configuration. Noriaki Ohmae, Wataru Kokuyama, and Yoichi Aso gave important advice on optics and noise sources. Kimio Tsubono and Masaki Ando were the supervisors and the leaders of our group. This work has been done at the University of Tokyo.

The results of this research are also published in the following papers by the author of this thesis.

- Yuta Michimura, Nobuyuki Matsumoto, Noriaki Ohmae, Wataru Kokuyama, Yoichi Aso, Masaki Ando, and Kimio Tsubono, Phys. Rev. Lett. **110**, 200401 (2013).
  New Limit on Lorentz Violation Using a Double-Pass Optical Ring Cavity
- Yuta Michimura, Nobuyuki Matsumoto, Noriaki Ohmae, Wataru Kokuyama, Yoichi Aso, Masaki Ando, and Kimio Tsubono, Proceedings of the Sixth Meeting on CPT and Lorentz Symmetry, edited by V. A. Kostelecký, pp.216-219 (World Scientific, Singapore, 2014) [arXiv: 1307.5266].
  Testing Lorentz Invariance with a Double-Pass Optical Ring Cavity
- Yuta Michimura, Matthew Mewes, Nobuyuki Matsumoto, Yoichi Aso, and Masaki Ando, Phys. Rev. D **88**, 111101(R) (2013).
  Optical cavity limits on higher order Lorentz violation

Chapter 2
Tests of Lorentz Invariance

Tests of Lorentz invariance have been performed in wide variety of fields since Einstein's special relativity was formulated more than 100 years ago. In this chapter, we will review previous tests of Lorentz invariance, particularly in the field of electrodynamics.

Firstly, Section 2.1 introduces test theories of special relativity and Lorentz invariance, which parameterize possible Lorentz violation. Section 2.2 reviews previous tests of the constancy of the speed of light and shows current upper limits on Lorentz violation. Section 2.3 describes the purpose and the scope of our experiment.

2.1 Test theories

In order to compare the precision of various experimental tests of Lorentz invariance, it is useful to introduce Lorentz violating parameters to physical theories. There are various test theories which have their own sets of parameters depending on their assumptions, but Robertson's framework [9] developed in 1949 was one of the first test theories of special relativity. In 1977, Mansouri and Sexl extended Robertson's framework, and their framework has been widely used in the tests of special relativity [10, 11, 12]. Recently, the theoretical framework of the Standard Model Extension (SME) [13] has been developed and used not only in the field of electrodynamics but also in other interactions.

Here, we will describe assumptions and meanings of the Lorentz violating parameters of those test theories. We will also introduce a spherical harmonic

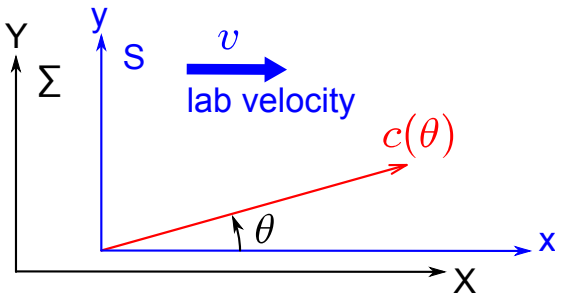

Figure 2.1: Preferred frame Σ and inertial frame S which moves with constant velocity v, with respect to Σ.

decomposition of the light speed anisotropy to compare precision of each test more phenomenologically.

2.1.1 Robertson framework

Robertson started constructing his framework from these two postulates:

- **Postulate 1**: There exists a preferred frame $\Sigma(T, X, Y, Z)$, in which the constancy of the speed of light holds true.
- **Postulate 2**: There is no preferred direction in Σ.

Let's consider an inertial frame $\mathrm{S}(t, x, y, z)$ which moves with constant velocity v, with respect to Σ, as shown in Fig. 2.1. Robertson also assumed the use of Einstein's method to synchronize clocks at different coordinate points in S.

In Newtonian mechanics, time flows constantly at the same speed independent of points, and a comparison of clocks at different points was just a technical problem. However, in special relativity, it is no longer true and we have to take some way to synchronize clocks. Einstein's method was to sent a light signal back and force between two points.

Consider synchronizing the clocks at points A and B in the frame S. A light signal is sent out from A at time $t = 0$, as recorded by the clock at A, reflected at $\mathrm{B}(t_1, x_1, y_1, z_1)$, and received back at A at clock time t_2. By assuming

- **Assumption**: The time it takes for light to go back and forth is the same,

we can synchronize the clocks with

$$t_1 = \frac{t_2}{2}. \tag{2.1}$$

One can write the space-time coordinate transformation from Σ to S in the most general linear form as

$$t = aT + \epsilon x + \epsilon_2 y + \epsilon_3 z, \tag{2.2a}$$
$$x = b_1 T + bX + b_2 Y + b_3 Z, \tag{2.2b}$$
$$y = d_1 T + d_2 X + dY + d_3 Z, \tag{2.2c}$$
$$z = e_1 T + e_2 X + e_3 Y + eZ. \tag{2.2d}$$

Parameters introduced here could be functions of the velocity of S. By using three assumptions mentioned above, this transformation can be simplified into

$$\begin{pmatrix} t \\ x \\ y \\ z \end{pmatrix} = \begin{pmatrix} \gamma/g_0 & -v\gamma/g_0 & 0 & 0 \\ -v\gamma/g_1 & \gamma/g_1 & 0 & 0 \\ 0 & 0 & 1/g_2 & 0 \\ 0 & 0 & 0 & 1/g_2 \end{pmatrix} \begin{pmatrix} T \\ X \\ Y \\ Z \end{pmatrix}, \tag{2.3}$$

where $\gamma = 1/\sqrt{1-v^2}$ [9]. This is the coordinate transformation in Robertson frame work, and the metric in S may be written as

$$\mathrm{d}s^2 = -g_0^2 \mathrm{d}t^2 + g_1^2 \mathrm{d}x^2 + g_2^2(\mathrm{d}y^2 + \mathrm{d}z^2). \tag{2.4}$$

Recall that Lorentz transformation between Σ and S is

$$\begin{pmatrix} t \\ x \\ y \\ z \end{pmatrix} = \begin{pmatrix} \gamma & -v\gamma & 0 & 0 \\ -v\gamma & \gamma & 0 & 0 \\ 0 & 0 & 1 & 0 \\ 0 & 0 & 0 & 1 \end{pmatrix} \begin{pmatrix} T \\ X \\ Y \\ Z \end{pmatrix}. \tag{2.5}$$

By comparing this with Robertson's transformation in Eq. (2.3), it is clear

that g_0, g_1 and g_2 are the parameters for the time dilation, length contraction in the direction of v, and length contraction in the direction orthogonal to v, respectively. In special relativity, $g_0 = g_1 = g_2 = 1$.

We can also derive the speed of light in S. Consider a light propagating in the x-y plane of S in the angular direction θ from x-axis (Fig. 2.1). Relations between coordinates in S are

$$x = c(\theta)t\cos\theta, \tag{2.6a}$$
$$y = c(\theta)t\sin\theta, \tag{2.6b}$$
$$z = 0. \tag{2.6c}$$

The propagation of light can be expressed with a geodesic equation

$$-T^2 + X^2 + Y^2 + Z^2 = 0. \tag{2.7}$$

By substituting (t, x, y, z) for (T, X, Y, Z) in Eq. (2.7) using Eq. (2.3) and Eq. (2.6), we obtain

$$c(\theta) = \frac{g_0}{\sqrt{g_1^2\cos^2\theta + g_2^2\sin^2\theta}}. \tag{2.8}$$

The speed of light is no longer constant in S and is anisotropic. Note that the speed of light in S can also be dependent of v since g_i's can be v-dependent.

Since Robertson used Einstein synchronization of clocks, $c(\theta) = c(\theta + \pi)$. Robertson framework is not a good framework for discussing tests of the isotropy of the *one-way* speed of light.

2.1.2 Mansouri-Sexl framework

Mansouri and Sexl started from the same two postulates (Postulates 1 and 2 in the previous section) Robertson assumed. However, instead of Einstein synchronization, they used slow clock transport scheme for the clock synchronization in order to avoid assuming $c(\theta) = c(\theta+\pi)$. In the slow clock transport scheme, the clock is slowly transported to one point and another to synchronize the clocks at different points. If the speed of the clock being transported is small enough compared with the speed of light, the effect of the time dilation

will be negligible.

If we only assume Postulates 1 and 2 in the previous section, a general linear form of coordinate transformations in Eq. (2.2) will be simplified into [10]

$$\begin{pmatrix} t \\ x \\ y \\ z \end{pmatrix} = \begin{pmatrix} a - \epsilon bv & \epsilon b & 0 & 0 \\ -vb & b & 0 & 0 \\ 0 & 0 & d & 0 \\ 0 & 0 & 0 & d \end{pmatrix} \begin{pmatrix} T \\ X \\ Y \\ Z \end{pmatrix}. \tag{2.9}$$

The speed of light in S can be derived in the same way as in the previous section:

$$c(\theta) = \frac{\epsilon b(1-v^2)\cos\theta + av\cos\theta - a\sqrt{\cos^2\theta + b^2d^{-2}(1-v^2)\sin^2\theta}}{[\epsilon^2 b(1-v^2) - a^2b^{-1} + 2\epsilon av]\cos^2\theta - a^2bd^{-2}\sin^2\theta}. \tag{2.10}$$

Here, let's consider expanding the four parameters introduced in Mansouri-Sexl framework, ϵ, a, b and d, with v. From Postulate 2, a, b and d should be independent of the direction, or sign, of v. The parameter ϵ is related to the clock synchronization and should be an odd function of v. Also, Eq. (2.9) should be $(T, X, Y, Z) = (t, x, y, z)$ when $v = 0$. Thus, we can expand the four parameters as follows [14]:

$$\epsilon(v) = \varepsilon v(1 - \varepsilon_2 v^2 + \cdots), \tag{2.11a}$$
$$a(v) = 1 + \alpha v^2 + \alpha_2 v^4 + \cdots, \tag{2.11b}$$
$$b(v) = 1 + \beta v^2 + \beta_2 v^4 + \cdots, \tag{2.11c}$$
$$d(v) = 1 + \delta v^2 + \delta_2 v^4 + \cdots. \tag{2.11d}$$

Equation (2.10) now can be rewritten as

$$c(\theta) = 1 - (\varepsilon+1)v\cos\theta - \left(\beta - \delta + \frac{1}{2}\right)v^2\sin^2\theta - (\alpha - \beta + 1)v^2 + \mathcal{O}(v^3). \tag{2.12}$$

If we use slow clock transport for the clock synchronization,

$$\varepsilon = 2\alpha \tag{2.13}$$

follows. Thus, the speed of light in S can be written up to the second order of

v as

$$c(\theta) = 1 - 2\left(\alpha + \frac{1}{2}\right) v\cos\theta - \left(\beta - \delta + \frac{1}{2}\right) v^2 \sin^2\theta - (\alpha - \beta + 1)v^2. \quad (2.14)$$

The use of the Einstein synchronization, on the other hand, $\varepsilon = -1$, and the anisotropic term for the *one-way* speed of light will disappear. So, here we adopt the slow clock transport for the clock synchronization. Details of the derivation can be found in Refs. [10, 15].

In Special Relativity, $c(\theta) = 1$ and therefore $\alpha = -1/2$, $\beta = 1/2$, and $\delta = 0$. Also, it is clear that the combined parameters $\alpha + 1/2$, $\beta - \delta + 1/2$, and $\alpha - \beta + 1$ represent the difference between the speed of light propagating in opposite directions, directional dependence of the round-trip speed of light, and dependence of the speed of light on the velocity of the light source, respectively. Each combined parameter is measured with different types of experiments. Classically, types of those experiments are called Ives-Stilwell type, Michelson-Morley type, and Kennedy-Thorndike type experiments, respectively.

Note that we have to set the preferred frame and the velocity of the laboratory frame v in order to derive these Lorentz violation parameters from the experimental data. One of the most natural candidates of the preferred frame is the CMB rest frame, and this frame has been often used. The CMB rest frame is the frame on which the dipole component of the measured CMB anisotropy cancels out. From the COBE observation, the speed of our Sun with respect to the CMB rest frame is obtained to be $v = 369$ km/s $\simeq 10^{-3}c$ [8]. Since this speed is considered to be constant for our timescale, these Lorentz violation parameters in the Sun centered frame are usually shown after the data analysis.

2.1.3 Standard Model Extension

Robertson framework and Mansouri-Sexl framework were the test theories of special relativity, and can only be used for the tests of Lorentz invariance in electrodynamics. Since late 1990's, a test theory called Standard Model Extension (SME) [13, 16] has been developed by Kostelecký and his co-workers to encompass all known physics and all realistic violations of Lorentz invariance.

Since then, the framework of the SME has been widely used to compare the precision of various experimental tests, and experimental results for the SME coefficients are summarized in the Data Tables for Lorentz and CPT Violation [3].

The framework of the SME starts with adding Lorentz violating terms in the Lagrangian density. When the Lorentz violating terms are added in the photon sector of the Lagrangian density, the Maxwell equations are modified, which result in a violation of the constancy of the speed of light. The Lorentz violating terms are partially characterized by the mass dimension d of the operator. The effects from higher d terms result in more complex form of the dependence of the speed of light on the source velocity, the polarization, the wavelength, and the propagation direction. In particular, higher d terms result in more complex multipole structures of the anisotropy.

For example, $d = 4$ terms give dipole and quadrupole structures, which resemble the anisotropy in the *one-way* speed of light and round-trip speed of light, respectively. $d = 8$ terms give dipole, quadrupole, and hexapole structures. $d = 3$ and $d = 4$ terms do not have photon momentum dependence, and they are renormalizable. However, $d > 4$ terms have photon momentum dependence of p^{d-4}, and they are nonrenormalizable.

The restriction to renormalizable dimensions yields the so-called minimal SME (mSME). The mSME has been studied extensively, and coefficients for the mSME have been limited by a number of experiments. On the other hand, nonminimal terms have received comparatively less attention due to the large variety and complexity of the higher order violations. However, a recent theoretical work has established phenomenology that opens up the nonminimal sector to experimentation [63]. The push to consider nonminimal terms in the SME is motivated in part by the apparent nonrenormalizability of gravity and by the possibility that higher-order violations with $d > 4$ might dominate. Theories based on noncommutative spacetime coordinates provide an example where Lorentz violation emerges in the form of operators of nonrenormalizable dimension only [17, 18].

In this thesis, we focus on the higher order violations from $d > 4$ terms. In particular, we focus on parity-odd higher order violations, since they have not been explored yet. Detailed calculations are shown in Appendix A.

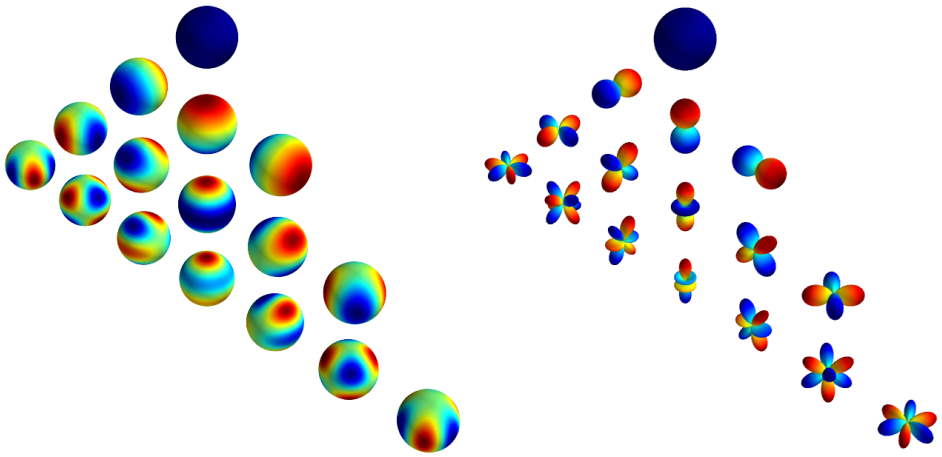

Figure 2.2: Spherical (left) and atomic orbital (right) visualization of spherical harmonics. Red portions represent where the function is positive, and blue portions represent where the function is negative.

2.1.4 Spherical harmonic decomposition of anisotropy

Although the framework of Mansouri-Sexl and the Standard Model Extension have been widely used to compare the upper limits of Lorentz invariance tests, they are not intuitive to be used for comparing experimental precision of each test. This is because the parameters introduced do not directly reflect the relative speed of light difference, $\delta c/c$.

To compare the precision more phenomenologically, it is useful if we simply expand the light speed anisotropy, without any theoretical assumptions or background. Using the spherical harmonics (Fig. 2.2)

$$Y_l^m(\theta,\phi) = (-1)^m \sqrt{\frac{2l+1}{4\pi}\frac{(l-m)!}{(l+m)!}} P_l^m(\cos\theta) e^{im\phi}, \tag{2.15}$$

the speed of light can be expanded as

$$c(\theta,\phi) = 1 + \sum_{l=0}^{\infty}\sum_{m=0}^{l} \mathrm{Re}\left[(\overline{y}_l^m)^* Y_l^m(\theta,\phi)\right]. \tag{2.16}$$

Here, $\theta \in [0,\pi]$ and $\phi \in [0,2\pi)$ is the polar angle and the azimuthal angle of

the spherical coordinates, respectively. P_l^m is associated Legendre polynomials, and l and m are integers. $\overline{y}_l^m$ are the complex anisotropy spherical coefficients which are zero when Lorentz invariance holds, and * represents the complex conjugate.

$l = 0$ term in Eq. (2.16) represents the isotropic shift of the speed of light and can be assigned to multiple Lorentz violations, such as dependence of the speed of light on the source velocity, polarization, or wavelength. In this thesis, we will neglect these terms because of the two reasons. One reason is because the leading order source velocity modulation only occurs at the period of a year from the revolution of the Earth around the sun. The other reason is because there are strict bounds on the Lorentz violation which cause the birefringence and dispersion. The detailed discussions will be addressed in Section A.1.

$l = 1,\ 2,\ 3, \cdots$ terms represent the dipole, quadrupole, hexapole, ... components of the anisotropy of the speed of light and can be measured separately by paying attention to the different types of rotational symmetries. $l = 2k + 1$ terms can be measured with Ives-Stilwell type, or odd-parity, experiments, and $l = 2k$ terms can be measured with Michelson-Morley type, or even-parity, experiments.

This framework of the spherical harmonic decomposition is also useful to do an analysis of anisotropy data independent of the choice of test theory. In this thesis, we will use this framework first to do an analysis and to show the experimental precision, and then do an analysis in the framework of the SME. It is natural to consider the spherical harmonic decomposition considering the fact that the SME also predicts multipole structure of the anisotropy.

2.2 Previous tests of Lorentz invariance

There has been a tremendous number of experimental tests of Lorentz invariance performed in a wide variety of fields. One of the most traditional and direct ways to test Special Relativity is to test the constancy of the speed of light. These tests are considered as tests of Lorentz invariance in electrodynamics, or in photons.

Here, we will review previous tests of the constancy of the speed of light and show current upper limits on Lorentz violation. We will classify those

tests into Ives-Stilwell type [19], Michelson-Morley type [20], and Kennedy-Thorndike type [21] experiments. Ives-Stilwell type experiments search for the odd-parity components of the light speed anisotropy, and Michelson-Morley type experiments search for the even-parity components. Kennedy-Thorndike type experiments search for the source velocity dependence of the speed of light.

There are also other types of tests of Lorentz invariance in electrodynamics, such as the independence of the speed of light on the polarization or the wavelength. These are tested to very high precision by astrophysical observations, since the effects of Lorentz violation are enhanced by the cosmological distances. Bounds on those Lorentz violations are given in the framework of the SME, so we will review these tests in Section A.1.

2.2.1 Michelson-Morley type experiments

Michelson-Morley type experiments look for the directional dependence of the round-trip speed of light. In the Mansouri-Sexl frame work, these experiments can be considered as measurements of $\beta - \delta + 1/2$. In the framework of the Standard Model Extension, these experiments are measurements of the parity-even Lorentz violating parameters of the photonic sector.

Michelson-Morley experiment

The first search for the anisotropy in the speed of light was originally done by Michelson and Morley in 1887 [20], as a measurement of the velocity of the ether wind. An apparatus they used is known as a Michelson interferometer shown in Fig. 2.3. The light from the source was split into two orthogonal paths by a beam splitter, and each beam was reflected back with a mirror. They tried to measure the difference between the speed of light propagating in the two directions as an interference fringe, since two beams interfere when coming back to the beam splitter again.

In Mansouri-Sexl framework, the round-trip phase difference between the

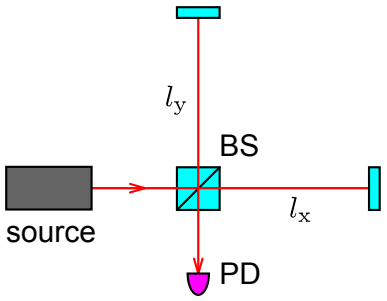

Figure 2.3: Michelson interferometer.

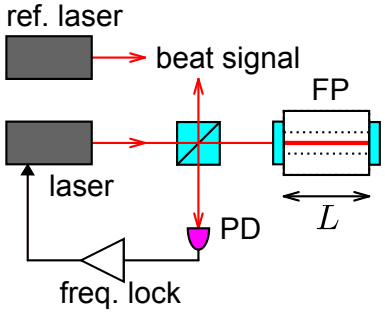

Figure 2.4: Brillet-Hall experiment.

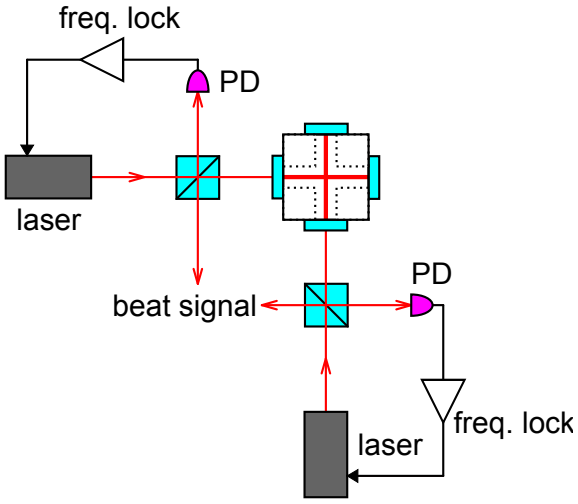

Figure 2.5: Michelson-Morley type experiment with two orthogonal Fabry-Perot cavities.

two beams can be written as

$$\begin{aligned}\phi_- &= \left(\frac{l\omega}{c(\theta)} + \frac{l\omega}{c(\theta+\pi)}\right) - \left(\frac{l\omega}{c(\theta+\pi/2)} + \frac{l\omega}{c(\theta+3\pi/2)}\right) \\ &= -2l\omega\left(\beta - \delta + \frac{1}{2}\right) v^2 \cos 2\theta, \end{aligned} \tag{2.17}$$

where $l \equiv l_x = l_y$ is the arm length of the Michelson interferometer, and ω is the angular frequency of the light. If there exists an ether wind, an interference pattern changes as the interferometer rotates and θ changes. Michelson and Morley looked for the fringe change as they rotate the interferometer which

was floated in a mercury pool, but they could not find any significant change.

Their experimental precision can be evaluated with the upper limit on the Mansouri-Sexl parameter as [12]

$$|\beta - \delta + 1/2| \lesssim 10^{-3}. \tag{2.18}$$

This is equivalent to

$$\left|\frac{\delta c}{c}\right| \lesssim 10^{-9} \tag{2.19}$$

of the fractional change in the speed of light.

Brillet-Hall experiment

Since the first experiment by Michelson and Morley, the anisotropy searches had been repeatedly performed as measurements of the velocity of the ether wind. The major breakthrough for the improvement of the sensitivity was brought by an invention of lasers in 1960. Among experiments done after the invention of lasers, an experiment by Brillet and Hall in 1979 [22] was especially a milestone experiment. To test the isotropy of the speed of light, they measured the change in the resonant frequency of a Fabry-Perot cavity (see Section C.1) as they rotate the cavity. As shown in Fig. 2.4, they locked the laser frequency to the resonant frequency of the rotating Fabry-Perot cavity, and took the beat signal from the laser and another stationary laser to measure the resonant frequency shift from rotation.

In Mansouri-Sexl framework, the resonant frequency of a Fabry-Perot cavity with the cavity length of L can be written as

$$\begin{aligned} \nu &= m\left(\frac{c(\theta)}{L} + \frac{c(\theta+\pi)}{L}\right) \\ &= \frac{m}{2L}\left[1 - \left(\beta - \delta + \frac{1}{2}\right)v^2\cos 2\theta - 2(\alpha - \beta + 1)v^2\right], \end{aligned} \tag{2.20}$$

where m is a natural number. Thus, if v is constant during the measurement, we can measure the directional dependence of the round-trip speed of light by extracting twice the cavity rotation frequency component of the beat frequency

change. The fractional speed of light change they measured was

$$\frac{\delta c}{c} = (1.5 \pm 2.5) \times 10^{-15}. \tag{2.21}$$

Their experimental precision was limited by the cavity deformation caused by the change of the cavity tilt in the rotational period. Amazingly, their precision was so high that it was the most precise measurement in the world until 2000's.

Recent cavity experiments

In 2000's, European groups started competing with each other by introducing modern techniques, such as cryogenic operation, ultra-high vacuum, and high level vibration isolation. The most stringent upper limit at this point is given by an experiment done by Eisele *et al.* [23], and their upper limit was

$$\beta - \delta + 1/2 = (-1.6 \pm 6 \pm 1.2) \times 10^{-12}, \tag{2.22}$$

in Mansouri-Sexl framework. Since the anisotropy in the round-trip speed of light can be written as $(\beta - \delta + 1/2)v^2 \cos 2\theta$, this is equivalent to putting an upper limit of

$$\left|\frac{\delta c}{c}\right| \lesssim 9 \times 10^{-18} \tag{2.23}$$

to the fractional change in the speed of light. Herrmann *et al.* [24] also reported a comparable upper limit at almost the same time.

As shown in Fig. 2.5, they locked two laser frequencies to two orthogonal Fabry-Perot cavities, and measured the beat frequency of the two lasers to look for the anisotropy. Since they used two Fabry-Perot cavities, their sensitivity to the anisotropy is simply twice the Brillet-Hall experiment. Moreover, they fabricated two Fabry-Perot cavities with a single spacer to make use of a high common mode rejection of environmental disturbances. For example, the cavity length fluctuation caused by the temperature fluctuation is mostly common to both cavities, and won't effect the beat signal.

The cavity deformation due to the tilt change, however, is also unavoidable in this setup. The first uncertainty in Eq. (2.22) is the statistical uncertainty,

and the second uncertainty is the systematic uncertainty in the tilt measurement. In their experiment, they monitored the tilt of the cavity and subtracted the effect from the beat signal, and this was the main cause of the systematic uncertainty.

Also, there is a similar experiment done by using two orthogonally aligned cryogenic sapphire oscillators [66]. They analyzed their year-long data within the framework of the Standard Model Extension and placed bounds on parity-even higher order Lorentz violating coefficients. Their bounds in terms of $\delta c/c$ was at 10^{-16} level, and the analysis was done up to $d = 8$ camouflage coefficients (see Section A.1.2). This means that they put upper limits on quadrupole and octupole components of anisotropy.

2.2.2 Kennedy-Thorndike type experiments

Kennedy-Thorndike type experiments search for the dependence of the speed of light on the source velocity. In the Mansouri-Sexl frame work, these experiments can be considered as measurements of $\alpha - \beta + 1$. In the framework of the Standard Model Extension, these experiments are measurements of the isotropic shift of the speed of light $\tilde{\kappa}_{\rm tr}$.

Kennedy-Thondike experiment

If the lengths of two orthogonal arms of a Michelson interferometer are different, it will be sensitive to the source velocity dependence of the speed of light. In the Mansouri-Sexl framework, the round-trip phase difference between the two beams of an asymmetric Michelson interferometer can be written as

$$\begin{aligned}\phi_- &= \left(\frac{l_{\rm x}\omega}{c(\theta)} + \frac{l_{\rm x}\omega}{c(\theta+\pi)}\right) - \left(\frac{l_{\rm y}\omega}{c(\theta+\pi/2)} + \frac{l_{\rm y}\omega}{c(\theta+3\pi/2)}\right) \\ &= 2l_{\rm x}\omega\left(\beta - \delta + \frac{1}{2}\right)v^2\sin^2\theta - 2l_{\rm y}\omega\left(\beta - \delta + \frac{1}{2}\right)v^2\cos^2\theta \\ &\quad +2(l_{\rm x} - l_{\rm y})\omega\,(\alpha - \beta + 1)\,v^2. \end{aligned} \tag{2.24}$$

Tighter constraints are set on $\beta - \delta + 1/2$ by Michelson-Morley type experiments, so first two terms can be neglected for the measurement of $\alpha - \beta + 1$. Since the Earth goes around the sun with the velocity of about 30 km/s $\sim$

$10^{-4}c$, v changes over a year. Thus, by measuring the interference fringe change in a period of a year, $\alpha - \beta + 1$ can be measured.

In 1932, Kennedy and Thorndike firstly demonstrated the measurement based on this principle [21]. Their upper limit in Mansouri-Sexl parameter was [12]

$$\alpha - \beta + 1 \lesssim (2 \pm 2) \times 10^{-2}. \tag{2.25}$$

Since the velocity modulation is on the order of $\delta v \simeq 10^{-4}$, this is equivalent to putting an upper limit of

$$\left|\frac{\delta c}{c}\right| \lesssim 2 \times 10^{-2} \times [(v + \delta v)^2 - v^2] \sim 5 \times 10^{-9} \tag{2.26}$$

to the fractional change in the speed of light.

Recent cavity experiments

Recently, the dependence of the speed of light on the source velocity is measured using cavities. As apparent from Eq. (2.20), the resonant frequency of a cavity will have v dependence if there is Lorentz violation. The current best upper limit is given by Tobar *et al.* [25]. By measuring the frequency difference between a cryogenic sapphire oscillator and a hydrogen maser for 6 years, they gave

$$\alpha - \beta + 1 = (-4.8 \pm 3.7) \times 10^{-8}. \tag{2.27}$$

This is equivalent to putting an upper limit of

$$\left|\frac{\delta c}{c}\right| \lesssim 3.7 \times 10^{-8} \times [(v + \delta v)^2 - v^2] \sim 9 \times 10^{-15} \tag{2.28}$$

to the fractional change in the speed of light.

2.2.3 Ives-Stilwell type experiments

Ives-Stilwell type experiments look for the difference between the speed of light propagating in opposite directions. In the Mansouri-Sexl frame work, these experiments can be considered as measurements of $\alpha + 1/2$. In the framework of the Standard Model Extension, these experiments are measurements of the

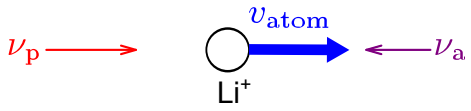

Figure 2.6: Ives-Stilwell experiment with lithium ions.

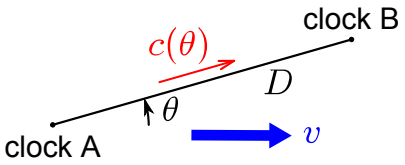

Figure 2.7: Clock comparison experiment.

parity-odd Lorentz violating parameters of the photonic sector.

Ives-Stilwell experiment

The frequency of the laser which is absorbed by fast moving atoms or ions will be shifted by Doppler effect when applying the light in parallel and antiparallel to the particles' motion, as shown in Fig. 2.6. This Doppler shift was firstly measured with hydrogen atoms by Ives and Stilwell in 1938 [19].

If the resonance frequency at the atoms' rest frame is ν_0, and the Doppler-shifted frequencies in parallel and antiparallel are $\nu_{\rm p}$ and $\nu_{\rm a}$, respectively, an equation

$$\nu_0^2 = \nu_{\rm p}\nu_{\rm a} \tag{2.29}$$

holds for the Special Relativity. However, this is not true if Lorentz invariance is violated. Instead, in Mansouri-Sexl framework,

$$\frac{\nu_{\rm p}\nu_{\rm a}}{\nu_0^2} = 1 + 2\left(\alpha + \frac{1}{2}\right)(v_{\rm atom}^2 + 2\boldsymbol{v}\cdot\boldsymbol{v}_{\rm atom}), \tag{2.30}$$

where $v_{\rm atom}$ is the speed of atoms [26].

Thus, by measuring $\nu_{\rm p}$ and $\nu_{\rm a}$, $\alpha + 1/2$ can be measured. The current most stringent upper limit is set by the experiment done by Reinhardt *et al.* [26], and they used lithium ions at two different velocities. They used an optical frequency comb for the measurement of the resonance frequency, and the current precision in Mansouri-Sexl framework is

$$\alpha + 1/2 = (-4.8 \pm 8.4) \times 10^{-8}. \tag{2.31}$$

Since the anisotropy in the *one-way* speed of light is expressed by $2(\alpha +$

$1/2)v\cos\theta$, this upper limit is equivalent to

$$\left|\frac{\delta c}{c}\right| \lesssim 2 \times 8.4 \times 10^{-8} v \sim 2 \times 10^{-10} \tag{2.32}$$

of the fractional hange in the speed of light.

Clock comparison experiments

The difference between the speed of light propagating in opposite directions can also be measured by comparing the phases of two clocks at distant places.

Suppose there are two clocks at the positions A and B as shown in Fig. 2.7. The distance between A and B is D, and the angle between the vector AB and the laboratory velocity vector $\boldsymbol{v}$ is θ. If we send a clock signal from the position A to B, and compare its phase with a clock signal at the position B, the phase difference can be written as

$$\phi = \phi_0 + \frac{D\omega}{c(\theta)} = \phi_0 + D\omega + 2D\omega\left(\alpha + \frac{1}{2}\right) v\cos\theta + \mathcal{O}(v^2), \tag{2.33}$$

in the Mansouri-Sexl framework. Here, ϕ_0 is the phase offset between the origins of the clocks at the positions A and B, and is constant if the two clocks are moving slowly enough compared with the speed of light. Thus, by measuring dependence of ϕ on θ, $\alpha + 1/2$ can be measured.

Krisher *et al.* [27] reported the upper limit on $\alpha + 1/2$ by measuring the sidereal change in the phase difference of two hydrogen-maser frequency standards on the Earth placed 21 km away from each other. Wolf *et al.* [28] did the similar experiment with a hydrogen maser on the Earth, and Caesium and Rubidium atomic clocks on GPS satellites. The upper limit from the latter measurement was more stringent, and it was

$$|\alpha + 1/2| < 1 \times 10^{-6}. \tag{2.34}$$

This upper limit is equivalent to

$$\left|\frac{\delta c}{c}\right| \lesssim 2 \times 1 \times 10^{-6} v \sim 2 \times 10^{-9} \tag{2.35}$$

of the fractional change in the speed of light.

Trimmer experiment

As shown in Eq. (2.17), the difference between the speed of light propagating in opposite directions cannot be measured using Michelson interferometers. This is because Michelson interferometers change their fringes when the round-trip phase of the light change. Other usual interferometers, including cavities, also have closed loops, and so they cannot be used for searches for anisotropy in the *one-way* speed of light. For example, in the Mansouri-Sexl framework, the phase shift of light created in a closed loop propagation can be written as

$$\begin{aligned} \phi_{\text{loop}} &= \oint \frac{\mathrm{d}l\omega}{c(\theta)} \\ &\simeq \oint \mathrm{d}l\omega \left[1 + 2\left(\alpha + \frac{1}{2}\right) v\cos\theta\right] \\ &= \oint \mathrm{d}l\omega, \end{aligned} \tag{2.36}$$

and the *one-way* anisotropy term is canceled out.

However, if the refractive index changes in a closed loop, the *one-way* anisotropy term remains. The experiment done by Trimmer *et al.* [29] in 1973 was the first experiment to utilize this idea. They searched for the anisotropy by placing a piece of glass in a Sagnac interferometer as shown in Fig. 2.8.

The phase difference between the light propagating in the clockwise direction and that in the counterclockwise direction in this Sagnac interferometer can be written as

$$\phi_{-} = 4(n-1)d\omega\left(\alpha + \frac{1}{2}\right) v\cos\theta, \tag{2.37}$$

where θ is the angle between the laboratory frame velocity $\boldsymbol{v}$ and the vector along the glass piece, n and d are the refractive index and the length of the glass piece, respectively. Thus, $\alpha + 1/2$ can be measured when $n \neq 1$. This is because the directions of light propagation in the glass piece are opposite between the clockwise and the counterclockwise propagation.

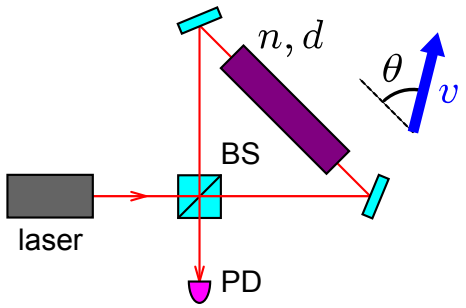

Figure 2.8: Trimmer experiment with the Sagnac interferometer with a glass piece.

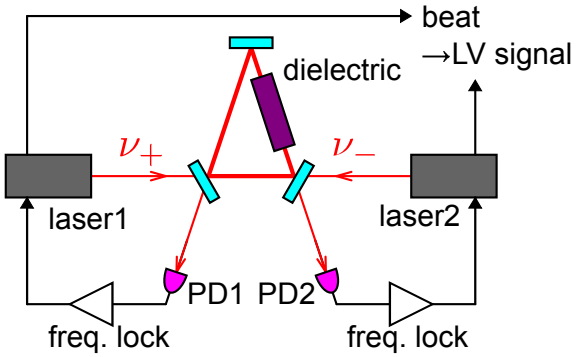

Figure 2.9: Experimental setup of Baynes *et al.* using asymmetric optical ring cavity. Note that their setup is slightly different from this figure since they split the beam from one source into two, and used an acousto-optic modulators to shift the frequency of the two, instead of using the second laser.

In the paper by Trimmer *et al.*, they expressed the anisotropy as

$$\frac{1}{c(\theta)} = 1 + b_1 P_1(\cos\theta) + b_3 P_3(\cos\theta), \tag{2.38}$$

where P_l are the Legendre polynomials. The measurement for the anisotropy that behaves as the first Legendre polynomial was

$$b_1 = (0.1 \pm 8.4) \times 10^{-11}, \tag{2.39}$$

and that for the third Legendre polynomial was

$$b_3 = (2.3 \pm 1.5) \times 10^{-11}. \tag{2.40}$$

Recent cavity experiments

Recently, improving the sensitivity by changing the Trimmer-type triangular Sagnac interferometer to a ring cavity was proposed [30, 31] and demonstrated [32, 33]. Baynes *et al.* [32, 33] looked for a nonzero resonant frequency difference between two counterpropagating directions of an asymmetric optical ring cavity. Their experimental setup is shown in Fig. 2.9. The asymmetric optical ring cavity was made with three mirrors and a piece of glass was placed along one side of the triangle. They locked the frequency of the two laser sources to the resonant frequencies of two counterpropagating directions and compared the frequency of the two.

Their upper limit on the fractional change in the speed of light was

$$\left|\frac{\delta c}{c}\right| \lesssim 2 \times 10^{-13}. \tag{2.41}$$

This limit was achieved by using data taken for 2 months.

Compton scattering experiment

The current best limit on anisotropy in the *one-way* speed of light is obtained by a Compton scattering experiment. When low energy photons are head-on scattered by relativistic electrons, the energy of the scattered photons in the laboratory frame can be written as [34]

$$E'_\gamma(\varphi) = \frac{4\gamma^2 E_\gamma}{1 + 4\gamma E_\gamma / m_e + \varphi^2\gamma^2}, \tag{2.42}$$

where φ is the angle between the scattered photon and the incident direction of the electron (see Fig. 2.10), γ and m_e is the Lorentz factor and the mass of the electron, respectively. The maximum energy of the scattered photons is obtained when $\varphi = 0$, and is called the Compton edge energy $E_0^{\mathrm{CE}} \equiv E'(0)$.

This Compton edge energy will be modified when there is light speed

anisotropy, since the dispersion relation of photons will be modified as

$$\omega = (1 - \boldsymbol{\kappa} \cdot \hat{\boldsymbol{k}})k, \tag{2.43}$$

where ω and k are the angular frequency and the wave number of photons, respectively. $\hat{\boldsymbol{k}}$ is a unit three-dimentional vector and $\boldsymbol{\kappa}$ is a three-dimentional vector of Lorentz violation parameters. In this case, the Compton edge energy will be modified as

$$E^{\mathrm{CE}} = E_0^{\mathrm{CE}} \left[1 + \frac{2\gamma^2}{(1 + 4\gamma E_\gamma / m_e)^2} \boldsymbol{\kappa} \cdot \hat{\boldsymbol{k}} \right]. \tag{2.44}$$

Thus, when the propagation direction of photons $\hat{\boldsymbol{k}}$ changes, the Compton edge energy should change.

Bocquet *et al.* [35] used ultraviolet laser and 6.03 GeV electrons to measure the Compton edge energy at the European Synchrotron Radiation Facility's GRAAL facility. They took data for a week and searched for the sidereal variations in the Compton edge energy. No significant variation was found and they yielded the constraint on the Lorentz violation parameters as

$$\sqrt{\kappa_{\mathrm{X}}^2 + \kappa_{\mathrm{Y}}^2} < 1.6 \times 10^{-14}. \tag{2.45}$$

This means that their upper limit on the fractional change in the speed of light was

$$\left| \frac{\delta c}{c} \right| < 1.6 \times 10^{-14}. \tag{2.46}$$

Note that their upper limit is given at 95% confidence level. Limits from the other experiments discussed in this section are usually given at 1σ level.

The indices J for κ_J in Eq. (2.45) runs from X to Z, which represent the spatial coordinate axes of the sun-centered celestial equatorial frame (SCCEF) defined in Section 5.1.1. They did not put separate upper limits on κ_{X} and κ_{Y} since they only measured the sidereal modulation amplitude, and did not account for the phase of the variation. Also, since the Z-axis is aligned with the Earth's rotational axis and they only use the Earth's rotation to modulate the propagation direction of the speed of light, it is not possible to measure κ_{Z} with their setup.

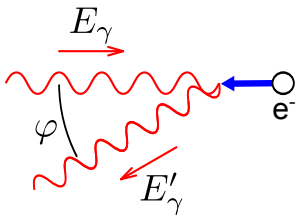

Figure 2.10: Compton scattering experiment.

Table 2.1: Summary of previous experiments with the current best sensitivities in terms of $\delta c/c$. Note that the limit from Bocquet *et al.* is at 95 % confidence level, while others are at 1σ. Also, the experiment done by Bocquet *et al.*cannot put limits on all the individual components for dipole anisotropy.

l	1	2	3	4
	dipole	quadrupole	hexapole	octupole
Eisele+ [23]	no access	9×10^{-18}	no access	no analysis
Parker+ [66]	no access	$\sim 10^{-16}$	no access	$\sim 10^{-16}$
Baynes+ [33]	2×10^{-13}	no access	no analysis	no access
Bocquet+ [35]	1.6×10^{-14} (*)	no access	no analysis	no access
This work	improve limits	no access	first analysis	no access

Cavity experiments, on the other hand, can measure each component of the anisotropy separately by doing the phase sensitive analysis and by rotating the apparatus.

2.3 Purpose of our experiment

We have reviewed the previous Michelson-Morley type, Kennedy-Thorndike type, and Ives-Stilwell type experiments. Table 2.1 summarizes the current best sensitivities on each anisotropy component. The current upper limits on even-parity and odd-parity components of the light speed anisotropy were at 10^{-17} level and 10^{-14} level at the fractional change in the speed of light, respectively. The source velocity independence of the speed of light was tested at 10^{-15} level.

Although upper limits on the odd-parity components were improved by

about 3 orders of magnitude by using asymmetric optical ring cavity, instead of fast ions, they were less stringent by 3 orders of magnitude as compared with even-parity components. The purpose of our experiment is to improve the sensitivity in searching for the odd-parity anisotropy components by refining the setup using asymmetric optical ring cavity.

Also, we will do the data analysis in the framework of the spherical harmonic decomposition and the SME to do the search for the higher order Lorentz violations. Our ring cavity is sensitive to the parity-odd violations, which had not been searched for.

2.4 Summary of this chapter

- Robertson framework, Mansouri-Sexl framework, and the Standard Model Extension (SME) are the test theories of special relativity and Lorentz invariance. The latter ones include more different types of the violations of the constancy of the speed of light.
- The SME introduces birefringence, dispersion, and multipole structures of the anisotropy.
- The spherical harmonic decomposition of the anisotropy, and its spherical coefficients $\overline{y}_l^m$ were introduced. $\overline{y}_l^m$ represent the size of the anisotropy for each component.
- The current upper limits on anisotropy in the round-trip and *one-way* speed of light are $\delta c/c \lesssim 10^{-17}$ and $\delta c/c \lesssim 10^{-14}$ level, respectively. The former was given by the cavity experiments. The latter cannot be measured by simple interferometers or cavities, and the current best limit was given by the Compton scattering experiment.
- Anisotropy in the *one-way* speed of light can be measured by the asymmetric ring cavity, which has a dielectric piece inside the ring.
- The purpose of our experiment is to measure anisotropy in the *one-way* speed of light with improved sensitivity. Also, we search for the parity-odd higher order Lorentz violation for the first time.

Chapter 3
Optical Ring Cavity

In this chapter, we will show the experimental principle of testing Lorentz invariance with an optical ring cavity. In Section 3.1, the experimental principle is explained, and a double-pass configuration which we will employ is introduced. Section 3.2 shows the sensitivity goal to improve the current upper limits, and various noise sources and their requirements are described in Section 3.3.

3.1 Experimental principle

A ring cavity will have direct sensitivity to the odd-parity Lorentz violation if the refractive index changes asymmetrically through its path. The resonant frequency will be shifted if there is Lorentz violation. As the signs of the frequency shift are opposite between the clockwise and counterclockwise directions, measuring the resonant frequency difference between two counterpropagating directions gives us the Lorentz violation signal. We use a double-pass configuration to do this differential measurement.

3.1.1 Principle

To show the experimental principle briefly, we simplify the spherical harmonic decomposition of the light speed anisotropy in Eq. (2.16) as

$$c(\theta) = 1 + \frac{1}{2\sqrt{\pi}}\,\overline{g}_1^0 \cos\theta, \tag{3.1}$$

and ignore any other terms.

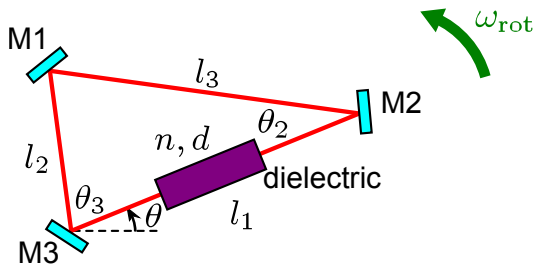

Figure 3.1: An optical ring cavity containing a dielectric.

Consider a triangular ring cavity which consists of 3 mirrors, M1, M2, and M3, and a dielectric material as shown in Fig. 3.1. The length and the refractive index of the material are d and n, respectively.

If we write the counterclockwise resonant frequency of the ring cavity as ν_+, the resonant condition (see Eq. (C.9)) can be written as

$$\frac{m}{\nu_+} = \frac{(l_1 - d)}{c(\theta)} + \frac{nd}{c(\theta)} + \frac{l_3}{c(\theta - \theta_2 + \pi)} + \frac{l_2}{c(\theta + \theta_3 + \pi)}, \tag{3.2}$$

using a natural number m. By inserting Eq. (3.1) to the equation above,

$$\begin{aligned} \frac{m}{\nu_+} &\simeq l_1 - d + nd + l_2 + l_3 \\ &\quad - \frac{1}{2\sqrt{\pi}}\, \overline{y}_1^0 \left[(l_1 - d)\cos\theta + nd\cos\theta - l_3\cos(\theta - \theta_2) - l_2\cos(\theta + \theta_3)\right] \\ &= L + (n-1)d - \frac{1}{2\sqrt{\pi}}\, \overline{y}_1^0\, (n-1)d\cos\theta. \end{aligned} \tag{3.3}$$

Here, $L \equiv l_1 + l_2 + l_3$.

Similarly, the clockwise resonant frequency ν_- follows the equation

$$\frac{m}{\nu_-} = L + (n-1)d + \frac{1}{2\sqrt{\pi}}\, \overline{y}_1^0\, (n-1)d\cos\theta. \tag{3.4}$$

If there is no Lorentz violation and $\overline{y}_1^0 = 0$, the resonant frequencies are $\nu = m/[L + (n-1)d]$ for both directions, but the resonant frequencies are shifted in opposite signs when Lorentz invariance is violated. Also, this shift cannot be measured when $n = 1$, and changing the refractive index of a portion

of the optical path is the key for this measurement.

The resonant frequency difference between both directions is

$$\frac{\delta\nu}{\nu} \equiv \frac{\nu_+ - \nu_-}{\nu} = \frac{(n-1)d}{L+(n-1)d}\frac{1}{\sqrt{\pi}}\,\overline{y}_1^0\cos\theta. \tag{3.5}$$

This difference signal is zero when there is no Lorentz violation. In our experiment, we record this Lorentz violation signal as we rotate the ring cavity and modulate θ. By demodulating the data with the rotational frequency, $\overline{y}_1^0$ can be extracted. Other $\overline{y}_l^m$ with odd l can also be measured similarly.

The optical path of a ring cavity is determined uniquely when arrangements of consisting mirrors are fixed. The optical paths are exactly the same for the counterclockwise and the clockwise directions. Thus, even if the cavity length fluctuated because of temperature fluctuations or tilt fluctuations, ν_+ and ν_- fluctuates in-phase, and $\delta\nu \equiv \nu_+ - \nu_-$ does not change. This common mode rejection is a big merit of this differential measurement.

It is possible that the refractive index also has the directional dependence. Modification of the Maxwell's equations could result in both of the directional dependence of the speed of light and the refractive index, and their effects could cancel each other. However, an example modification of the Maxwell's equations that does not cancel the effect is already proposed (e.g. Ref. [36]). The directional dependence of the refractive index is also the Lorentz violation, but it is considered to be the Lorentz violation in electrons, not in photons. In our experiment, we assume that the Lorentz invariance holds in the electron sector, and search for the Lorentz violation in photons.

3.1.2 Double-pass configuration

One of the most straightforward methods to compare the counterclockwise and the clockwise resonant frequencies is to prepare two laser sources and lock the laser frequencies of the two to each resonance, as shown in Fig. 2.9. Baynes *et al.* used this method and compared the laser frequencies of the two.

However, the frequencies of the two laser beams have to be different by more than a few hundred Hz to use this method in real life. The counterclockwise and the clockwise beams couple to each other via backscattering inside the

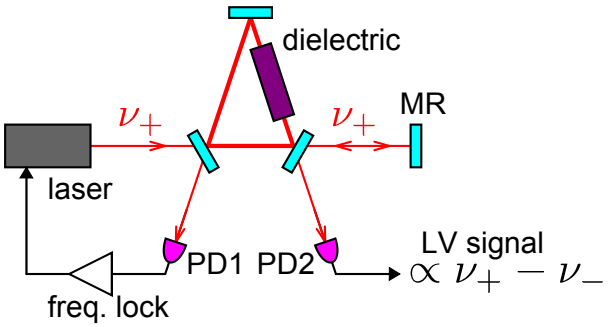

Figure 3.2: Our optical setup using a double-pass configuration.

cavity, and the coupling effect is fed back to the laser frequency by the servo. This feedback makes the frequencies of the two laser sources to be the same even if there is the resonant frequency difference between counterpropagating directions because of Lorentz violation.

This lock-in behavior is also a problem in ring laser gyroscopes [37]. In order to avoid this lock-in behavior, the frequencies of the two laser sources must have the frequency offset which is multiples of a free spectral range to each other. This offset prevents the measurement to be null.

Instead, we employed the configuration called double-pass. A double-pass configuration was originally proposed for use in mode cleaners for interferometric gravitational wave detectors [38, 39]. Our optical setup using a double-pass configuration is shown in Fig. 3.2.

First, we get the error signal which is proportional to the difference between the laser frequency and the counterclockwise resonant frequency ν_+ using the photodetector PD1, and lock the laser frequency to ν_+. The cavity transmitted beam which has the frequency of ν_+ is reflected back into the cavity by a mirror MR, and injected in the clockwise direction this time. If the clockwise resonant frequency ν_- is equal to ν_+, the reflected beam also resonates in the cavity. However, if there is a difference, we can get the signal which is proportional to the difference $\delta\nu \equiv \nu_+ - \nu_-$ from the second reflection on the photodetector PD2.

The error signal from the PD2 is the Lorentz violation signal on its own, and there exist only beams with the same frequency. Thus, there is no mechanism

for lock-in behavior. This double-pass configuration is the method which make the best out of the ring cavity, and allows high-precision null measurement of the Lorentz violation.

3.1.3 Advantages compared with previous experiments

As we saw in Section 2.2.3, Ives-Stilwell type interferometric tests of isotropy of the speed of light was firstly done by Trimmer *et al.* in 1973. They used a Sagnac interferometer, but in Sagnac interferometers, positions or alignments of mirrors change the optical paths of counterpropagating directions, and thus temperature fluctuation and similar environmental disturbances will be noise sources. In ring cavities, however, effects from environmental disturbances are suppressed because of the high common mode rejection. Until recently, an improvement of Trimmer experiment by using a ring cavity has not been carried out.

The first ring cavity test of isotropy of the speed of light was done by Baynes *et al.* [32], and they reported the results in October 2011. They first used the Earth's rotation alone to modulate the signal, but they also reported the rotating experiment in June 2012 [33]. The setup they used was to use two laser sources as shown in Fig. 2.9. They did not do the constant speed rotation. The cavity was rotated for 180° each time, and the data were taken for ~ 10 minutes at each orientation when the cavity was stationary.

On the other hand, we rotate the cavity at the constant speed, and data are taken continuously during the rotation. The rotational period of our experiment is 12 seconds. Generally, noise level at higher frequency is smaller, so higher rotational frequency is better. Also, we use a double-pass configuration as shown in Fig. 3.2. This double-pass configuration enables a null measurement of the resonant frequency difference with a simpler configuration than that of Refs. [32, 33]. Also, stabilizing the frequencies of two counterpropagating beams of a ring cavity has the possibility of lock-in behavior [37], which is a common effect in ring laser gyroscopes.

Also, we use silicon as a dielectric material since its refractive index and transmittance is high at the wavelength of 1550 nm. Compared with using optical glass, which has $n = 1.44$ at the wavelength of 1064 nm, silicon with

$n = 3.69$ gives approximately 4 times better sensitivity to the Lorentz violation (see Eq. (3.5)).

Moreover, the number of the Lorentz violation coefficients that can be accessed by our experiment is larger than the previous experiments. Because data were not taken continuously during the cavity rotation, Baynes *et al.*could only access to the Lorentz violation coefficients which are related to the dipole structure of the anisotropy. The Compton scattering experiment done at the GRAAL facility [35] cannot access to the coefficients which are related to the Z-axis symmetric anisotropies, as discussed in Section 2.2.3. On the contrary, our setup can access all the coefficients related to parity-odd violations.

3.2 Sensitivity goal

The goal of our experiment is to measure the anisotropy in the *one-way* speed of light to the level better than the current best limit obtained by a cavity experiment. The limit is shown in Eq. (2.41), and this means that we have to measure $\overline{y}_1^m$ at better than 10^{-13} level. Here, we estimate the sensitivity goal to fulfill this requirement.

As we have shown in the previous section, the anisotropy signal $s(t)$ is given by Eq. (3.5), and

$$s(t) = \frac{\delta\nu}{\nu} = \frac{(n-1)d}{L+(n-1)d}\frac{1}{\sqrt{\pi}}\ \overline{y}_1^0 \cos\theta. \tag{3.6}$$

If we ignore the Earth's rotation, $\theta \simeq \omega_{\rm rot} t$, and thus $\omega_{\rm rot}$ component of $s(t)$ gives $\overline{y}_1^0$. The Fourier amplitude ξ at $\omega_{\rm rot}$ can be written as

$$\xi \sim \sqrt{\left|\frac{2}{N} S(\omega_{\rm rot})\right|^2}, \tag{3.7}$$

where $S(\omega)$ is the discrete Fourier transform of $s(t)$, and N is the number of data points.

On the other hand, using the sampling frequency $f_{\rm s}$, the power spectral

density of $s(t)$ at $\omega_{\rm rot}$ can be written as

$$P_s(\omega_{\rm rot}) = \sqrt{\frac{1}{N f_{\rm s}} |S(\omega_{\rm rot})|^2}. \tag{3.8}$$

Power spectral density is often used for evaluating a noise level or a sensitivity level of a system in the frequency domain, and also called noise spectrum.

From Eq. (3.7) and Eq. (3.8), using $P_s(\omega_{\rm rot})$, ξ can be written as

$$\xi \sim \frac{2}{\sqrt{T}} P_s(\omega_{\rm rot}). \tag{3.9}$$

Here, $T = N/f_{\rm s}$ is the measurement time, and from this equation, it is clear that the measurement precision is inversely proportional to the square root of the measurement time.

Our requirement is to determine $\overline{y}_1^m$ at level better than 10^{-13}, so requirement for ξ determination is 10^{-13}. If we set the measurement time to be 1 year, $T = 3 \times 10^7$ sec, requirement for the noise at $\omega_{\rm rot}$ is roughly

$$P_s(\omega_{\rm rot}) \lesssim 10^{-10} \ /\sqrt{\rm Hz}. \tag{3.10}$$

In the remaining part of this thesis, we use the same symbols for time series data like $s(t)$ and spectrum data like $P_s(\omega)$. This is possible since we deal with linear response system.

3.3 Noise sources and requirements

Since we search for Lorentz violation by comparing the resonant frequencies of the counterpropagating directions of the ring cavity, most of the noises from environmental disturbances are canceled out by the common mode rejection. However, the common mode rejection is not effective to some noises. Also, even if the common mode rejection cancels out some effects, the common mode rejection ratio is finite.

Here, we will enumerate the noises which could limit the sensitivity of our apparatus, and show the requirements for each noise calculated from Eq. (3.10). All the requirements are set at the rotational frequency $f_{\rm rot} = \omega_{\rm rot}/(2\pi) =$

Table 3.1: Parameters of our apparatus used for the noise calculation.

laser wavelength	$\lambda = 1550$ nm
laser frequency	$\nu = 1.93 \times 10^{14}$ Hz
incident beam power	$P_0 = 1$ mW
finesse	$\mathcal{F} = 120$
cavity round-trip length	$L = 140$ mm
area enclosed by the cavity optical path	$S = 530$ mm^2
silicon block length	$d = 20$ mm
silicon block refractive index	$n = 3.69$
rotational angular frequency	$\omega_{\rm rot} = 30$ °/sec $= 0.524$ rad/sec

0.083 Hz, because the Lorentz violation signal appears at the rotational frequency of the ring cavity.

The parameters used for the noise calculation are summarized in Table 3.1. Strictly speaking, the incident beam powers in the counterclockwise direction and the clockwise direction are different, but we use the approximation that they are both P_0 in the calculation below. Powers of both incident beams are within the same order in our setup.

3.3.1 Shot noise

Shot noise arises from a quantum fluctuation of a number of photons on a photodetector, and is one of the quantum noise which originates from Heisenberg's uncertainty principle. Shot noise is a white noise, and its power spectral density can be written as

$$\delta I_{\rm shot} = \sqrt{2eI_{\rm PD}} \ \ [\mathrm{A}/\sqrt{\mathrm{Hz}}], \tag{3.11}$$

where $I_{\rm PD}$ is a photocurrent of a detector [40].

Consider rewriting this equation with quantum efficiency η. Quantum efficiency is defined as a number of output electrons per one incident photon. Thus, it can be written as

$$\eta \equiv \frac{I_{\rm PD}/e}{P_{\rm PD}/(h\nu)}, \tag{3.12}$$

where P_{PD} is the incident beam power on the photodetector, and

$$I_{\mathrm{PD}} = \frac{e}{h\nu}\eta P_{\mathrm{PD}} \tag{3.13}$$

follows. Here, e is the elementary charge, and h is the Planck's constant. By inserting this equation to Eq. (3.11), the minimum detectable power change from the shot noise can be calculated as

$$\delta P_{\mathrm{shot}} = \sqrt{\frac{2h\nu P_{\mathrm{PD}}}{\eta}}. \tag{3.14}$$

In our experiment, we use the Hänsch-Couillaud method (or polarization spectroscopy) [70, 71] to obtain the error signals. Detailed calculations in Section C.3.1 show that in the Hänsch-Couillaud method, incident beam power on one photodetector at the cavity resonance is

$$P_{\mathrm{PD}} = \frac{1}{4}P_0. \tag{3.15}$$

Also, the ratio between the change in the error signal P_{diff}, and the change in the round-trip phase of the ring cavity ϕ at near resonance is

$$\frac{\partial P_{\mathrm{diff}}}{\partial \phi} = \frac{1}{\pi}P_0\mathcal{F}. \tag{3.16}$$

Therefore, the minimum detectable phase change from the shot noise is

$$\begin{aligned} \delta\phi_{\mathrm{shot}} &= \sqrt{2}\delta P_{\mathrm{shot}}\left(\frac{\partial P_{\mathrm{diff}}}{\partial \phi}\right)^{-1} \\ &= \frac{\pi}{\mathcal{F}}\sqrt{\frac{h\nu}{\eta P_0}}. \end{aligned} \tag{3.17}$$

$\sqrt{2}$ in the first line comes from the fact that we use the difference signal from the two photodetectors to obtain the error signal, and the shot noises from the two detectors are added incoherently.

Since ϕ can be written as

$$\phi = \frac{2\pi}{\lambda}[L + (n-1)d], \tag{3.18}$$

the minimum detectable resonant frequency change from the shot noise is

$$\frac{\delta\nu_{\text{shot}}}{\nu} = \frac{\delta\phi_{\text{shot}}}{\phi} = \frac{1}{2[L + (n-1)d]\mathcal{F}}\sqrt{\frac{ch\lambda}{\eta P_0}}. \tag{3.19}$$

The quantum efficiency is typically $\eta \simeq 1$. So, if we insert the parameters for our ring cavity, we get

$$\frac{\delta\nu_{\text{shot}}}{\nu} \simeq 4 \times 10^{-16}\ /\sqrt{\text{Hz}} < 10^{-10}\ /\sqrt{\text{Hz}}. \tag{3.20}$$

So, the design of our ring cavity is enough to meet the requirement. As it is clear from Eq. (3.19), the shot noise can be further lowered by an order of magnitude by increasing the cavity finesse by an order of magnitude or by increasing the incident beam power by two orders of magnitude.

3.3.2 Laser intensity noise

In interferometric phase detections including our experiment, the phase change is converted into the power change and detected by a photodetector. So, if the apparatus cannot distinguish the intensity fluctuation from the phase fluctuation, the intensity fluctuation of the incident beam will be a noise source.

We use the Hänsch-Couillaud method, and take difference of two photodetectors to obtain the error signal. Since the intensity noise is common to both detectors, the effect can be eliminated by this method. However, the common mode rejection ratio is finite and some effects are remained. From Eq. (3.15), the intensity noise in the error signal can be written as

$$\delta P_{\text{int}} = \frac{1}{4}\gamma^{\text{int}}_{\text{CMRR}} P_0 \frac{\delta P_0}{P_0}, \tag{3.21}$$

where $\gamma^{\text{int}}_{\text{CMRR}}$ is the common mode rejection ratio. Thus, the minimum de-

tectable phase change from the intensity noise is

$$\begin{aligned} \delta\phi_{\rm int} &= \delta P_{\rm int}\left(\frac{\partial P_{\rm diff}}{\partial\phi}\right)^{-1} \\ &= \frac{\pi\gamma^{\rm int}_{\rm CMRR}}{4\mathcal{F}}\frac{\delta P_0}{P_0}, \end{aligned} \tag{3.22}$$

and from Eq. (3.18), the minimum detectable resonant frequency change is

$$\frac{\delta\nu_{\rm int}}{\nu} = \frac{\delta\phi_{\rm int}}{\phi} = \frac{\gamma^{\rm int}_{\rm CMRR}\lambda}{8[L+(n-1)d]\mathcal{F}}\frac{\delta P_0}{P_0}. \tag{3.23}$$

Empirically, the common mode rejection ratio for the intensity noise is roughly 1/100 at best. Here, we assume $\gamma^{\rm int}_{\rm CMRR} = 1/10$, and the parameters for our ring cavity give

$$\frac{\delta\nu_{\rm int}}{\nu} = 8\times10^{-10}\frac{\delta P_0}{P_0}. \tag{3.24}$$

Hense, the requirement for the relative intensity noise of the incident beam is

$$\begin{aligned} \frac{\delta P_0}{P_0} &< \frac{10^{-10}\ /\sqrt{\rm Hz}}{8\times10^{-10}} \\ &\simeq 1\times10^{-1}\ /\sqrt{\rm Hz} \qquad (@\ f_{\rm rot} = 0.083\ {\rm Hz}). \end{aligned} \tag{3.25}$$

This level is easily obtained without any intensity stabilization. The measured relative intensity noise at free run was $2\times10^{-3}\ /\sqrt{\rm Hz}$ for our laser.

3.3.3 Laser frequency noise

We compare the resonant frequencies of counterpropagating directions by locking the laser frequency to the counterclockwise resonance, and injecting the beam into the clockwise direction. Ideally, the laser frequency is perfectly locked to the counterclockwise resonance, but in reality, there are some residual frequency fluctuations between the counterclockwise resonance and the laser frequency.

Requirement for the residual laser frequency noise is the same as the one

in Eq. (3.10), and is

$$\frac{\delta\nu_{\text{freq}}}{\nu} < 10^{-10}\ /\sqrt{\text{Hz}} \qquad (@\ f_{\text{rot}} = 0.083\ \text{Hz}). \tag{3.26}$$

Details of the frequency stabilization are discussed in Section 4.2.3.

The full width at half maximum of the resonance of our cavity is (see Section C.1.2)

$$\nu_{\text{FWHM}} = \frac{c}{[L + (n-1)d]\mathcal{F}} \simeq 12\ \text{MHz}. \tag{3.27}$$

This means that the frequency noise of the cavity transmitted beam is the same as the one for the laser frequency noise below Fourier frequency of ~ 12 MHz. Since we only care about the noise at the rotational frequency f_{rot}, we can assume that the laser frequency stability directly affects the Lorentz violation signal.

3.3.4 Noise from Sagnac effect

The clockwise and the counterclockwise resonant frequencies are different for rotating ring cavities because of the Sagnac effect [41]. If the rotational speed is constant, this resonant frequency difference is constant, so it does not affect our measurement, but if the rotational speed fluctuates, it will be a noise source.

The round-trip phase difference between the beams propagating in the clockwise and the counterclockwise directions is [42]

$$\phi_{\text{Sagnac}} = \frac{4\pi}{c\lambda} \oint_l \boldsymbol{v}_l \cdot \mathrm{d}\boldsymbol{l}, \tag{3.28}$$

and is independent of the refractive index of the optical path. Here, $\mathrm{d}\boldsymbol{l}$ is the line element vector of the optical path, and $\boldsymbol{v}_l$ is the speed of motion of that line element from the rotation. Note that the equation above is true when Fresnel-Fizeau effect is negligible, i.e. when $\omega_{\text{rot}} R \ll c/n$, where R is the average radius of the ring (see, also, Eq. (56) of Ref. [43]).

Therefore, by using Eq. (3.18) also, the resonant frequency difference be-

tween counterpropagating directions caused by the Sagnac effect is

$$\begin{aligned}\frac{\delta\nu_{\rm Sagnac}}{\nu} = \frac{\delta\phi_{\rm Sagnac}}{\phi} &= \frac{8\pi S\delta\omega_{\rm rot}/(c\lambda)}{2\pi[L+(n-1)d]/\lambda} \\ &= \frac{4S}{c[L+(n-1)d]}\delta\omega_{\rm rot}. \end{aligned} \tag{3.29}$$

Here, S is the area enclosed by the triangular cavity optical path.

By inserting the parameters for our ring cavity, we get

$$\frac{\delta\nu_{\rm Sagnac}}{\nu} = 4\times10^{-11}\ ({\rm rad/sec})^{-1}\ \delta\omega_{\rm rot}. \tag{3.30}$$

Thus, the requirement for the fluctuation of $\omega_{\rm rot}$ is

$$\begin{aligned}\delta\omega_{\rm rot} &< \frac{10^{-10}\ /\sqrt{\rm Hz}}{4\times10^{-11}\ ({\rm rad/sec})^{-1}} \\ &\simeq 3\ {\rm rad/sec}/\sqrt{\rm Hz} \qquad (@\ f_{\rm rot}=0.083\ {\rm Hz}). \end{aligned} \tag{3.31}$$

For the rotational speed servo, we used a commercial motor control system. Details of the turntable are discussed in Section 4.3.

It is worth mentioning that the Sagnac effect can be fundamentally avoided by taking the Lorentz violation data only when the cavity is stationary. Modulation of the cavity orientation can be done by rotating the cavity by a few degrees and stopping it repeatedly. However, since the requirement for the fluctuation of $\omega_{\rm rot}$ was not severe for our experiment, we chose to continuously take data when the ring cavity is rotating. This is also beneficial for longer measurement time.

3.3.5 Other noises

Seismic noise

Even if the cavity length fluctuates because of the seismic vibration or the turntable vibration, the resonant frequencies of both directions change coherently, and will not be a noise source for our measurement, in principle. Also, by fixing the optics rigidly, the whole optical system moves in the same way, and the effect of vibrations can be further reduced. To reduce the effect from

the vibrations, we fix three mirrors of the ring cavity to a single spacer, and also fix whole the optics to a single aluminum plate.

The level of the seismic vibration depends on places, local time, weather, etc. but it roughly follows the following spectrum [44]:

$$x_{\mathrm{seis}} = 10^{-7} \left(\frac{1\ \mathrm{Hz}}{f} \right)^2 \ \mathrm{m}/\sqrt{\mathrm{Hz}} \tag{3.32}$$

The actual seismic vibration measured at our laboratory also follows this model at frequencies higher than ~ 10 Hz. Below 10 Hz, the measured spectrum is typically smaller than the model. However, we use this model for overestimating the vibration level.

So, using γ_{CMRR} as the common mode rejection ratio of the resonant frequencies of counterpropagating directions, and $\gamma_{\mathrm{CMRR}}^{\mathrm{rigid}}$ as the common mode rejection ratio from fixing the mirrors rigidly on a spacer, the fluctuation in the resonant frequency difference between counterpropagating directions can be written as

$$\frac{\delta\nu_{\mathrm{seis}}}{\nu} \sim \gamma_{\mathrm{CMRR}}\gamma_{\mathrm{CMRR}}^{\mathrm{rigid}} \frac{\delta x_{\mathrm{seis}}}{L} \sim \gamma_{\mathrm{CMRR}}\gamma_{\mathrm{CMRR}}^{\mathrm{rigid}} \times 10^{-6}\ /\sqrt{\mathrm{Hz}}. \tag{3.33}$$

To meet the requirement in Eq. (3.10),

$$\gamma_{\mathrm{CMRR}}\gamma_{\mathrm{CMRR}}^{\mathrm{rigid}} \lesssim 10^{-4} \tag{3.34}$$

is required. Empirically, $\gamma_{\mathrm{CMRR}}^{\mathrm{rigid}} < 10^{-6}$ can be expected. So, this requirement is not severe, and we can say that no special vibration isolation system is needed.

We will also place all the optics on a single aluminum plate to reduce effects from vibrations outside the ring cavity. However, since the vibration of the turntable is expected to be much larger than the seismic vibration, we should keep our eyes on the vibration. This turntable vibration issue will be discussed in Section 4.3.3.

Thermal noise

The surfaces of the mirrors and the spacer length fluctuate thermally because the cavity is placed in a heat bath with a finite temperature. Those thermal fluctuations induce unwanted cavity length changes, which result in thermal noises. The amplitude of the fluctuating force is proportional to the mechanical losses in the body itself, according to the fluctuation-dissipation theorem [45]. The surface thermal motion of the mirror caused by its substrate and coating are called the mirror substrate thermal noise and the coating thermal noise, respectively. The thermal fluctuation of the spacer length is called the spacer thermal noise. Here, we only consider the Brownian noise.

The spectrum of the spacer thermal noise [46], the mirror substrate thermal noise, and the coating thermal noise [47, 48] are represented by

$$\frac{\delta\nu_{\rm spc}}{\nu} = \frac{1}{L}\sqrt{\frac{4k_{\rm B}T_{\rm cav}}{Q_{\rm spc}\omega}\frac{2\rho l^2}{\pi^2 E_{\rm spc}M}}, \tag{3.35}$$

$$\frac{\delta\nu_{\rm sub}}{\nu} = \frac{1}{L}\sqrt{\frac{4k_{\rm B}T_{\rm cav}}{Q_{\rm sub}\omega}\frac{1-\sigma_{\rm sub}^2}{\sqrt{\pi}E_{\rm sub}w}}, \tag{3.36}$$

$$\frac{\delta\nu_{\rm co}}{\nu} = \frac{1}{L}\sqrt{\frac{4k_{\rm B}T_{\rm cav}}{Q_{\rm co}\omega}\frac{2d_{\rm co}(1+\sigma_{\rm co})(1-2\sigma_{\rm co})}{\pi E_{\rm sub}w^2}}, \tag{3.37}$$

respectively. These equations are valid in the frequency range below their respective resonant frequencies. The expression for the spacer thermal noise is obtained by assuming the spacer to be a cylinder. As we can see, lowering the temperature $T_{\rm cav}$ and using higher Q-value materials give smaller thermal noise. Q-values are related with the mechanical loss for each material, and lower loss gives higher Q-values.

The definitions of each parameter and the values used for thermal noise calculation are listed in Table 3.2. The resulting thermal noise levels are

$$\frac{\delta\nu_{\rm spc}}{\nu} = 2\times10^{-16}\ /\sqrt{\rm Hz}, \tag{3.38}$$

$$\frac{\delta\nu_{\rm sub}}{\nu} = 2\times10^{-16}\ /\sqrt{\rm Hz}, \text{ and} \tag{3.39}$$

$$\frac{\delta\nu_{\rm co}}{\nu} = 4\times10^{-16}\ /\sqrt{\rm Hz} \qquad (@\ f_{\rm rot} = 0.083\ {\rm Hz}). \tag{3.40}$$

Table 3.2: Parameters used for the thermal noise calculations. The spacer material is Super Invar, and the mirror substrate is fused silica. The mirrors are coated with delectric multi-layer coating. Material properties listed here are conservative and empirical values taken from Refs. [46, 50, 49].

temperature	$T_{\rm cav} = 300$ K
spacer density	$\rho = 8 \times 10^3$ kg/m^3
spacer length	$l \sim L/2$
spacer weight	$M = 0.34$ kg
spacer Q-factor	$Q_{\rm spc} = 10^4$
spacer Young's modulus	$E_{\rm spc} = 140$ GPa
substrate Q-factor	$Q_{\rm sub} = 10^6$
substrate Young's modulus	$E_{\rm sub} = 70$ GPa
substrate Poisson's ratio	$\sigma_{\rm sub} = 0.17$
coating Q-factor	$Q_{\rm co} = 10^3$
coating Poisson's ratio	$\sigma_{\rm co} = 0.17$
coating thickness	$d_{\rm co} = 8$ μm
beam radius	$w = 210$ μm

Values in Table 3.2 come from the properties of the spacer material, Super Invar, and the mirror substrate material, fused silica, in Ref. [50]. Q-values and $d_{\rm co}$ are empirically assumed conservative values [49]. Also, the mirror substrate thermal noise and the coating thermal noise have to be multiplied by $\sqrt{3}$ to incorporate the effect from 3 mirrors. Even so, the thermal noise levels are more than 5 orders of magnitude below our requirement.

Thus, we need no cryogenic operation from the thermal noise point of view. The thermal noise level might be even smaller if we consider that the thermal noise is common to both clockwise and counterclockwise resonances.

Temperature fluctuation

The fluctuation in the cavity temperature changes the cavity optical length because of the thermal expansion of the spacer and the silicon piece, and the change in the refractive index of silicon. Since this effect is common to both clockwise and counterclockwise resonances, this effect does not create noise in principle.

The fluctuation in the resonant frequency difference between counterpropagating directions from the cavity temperature fluctuation $\delta T_{\rm cav}$ can be written as

$$\frac{\delta\nu_{\rm temp}}{\nu} = \gamma_{\rm CMRR}\frac{\alpha_{\rm spc}L + \alpha_{\rm Si}(n-1)d + \frac{{\rm d}n}{{\rm d}T}d}{L+(n-1)d}\delta T_{\rm cav}, \tag{3.41}$$

where $\alpha_{\rm spc}$ and $\alpha_{\rm Si}$ are the thermal expansion coefficients of the spacer and silicon, respectively. $\frac{{\rm d}n}{{\rm d}T}$ is the thermo-optic coefficient of silicon, and $\gamma_{\rm CMRR}$ is the common mode rejection ratio of the resonant frequencies of counterpropagating directions.

As a material of the spacer, we use Super Invar which has low thermal expansion coefficient ($\alpha_{\rm L} \sim 10^{-7}$ /K [50]). The thermal expansion coefficient of silicon is 3×10^{-6} /K at room temperature [50]. The thermo-optic coefficient of silicon at 1550 nm and at room temperature is 2×10^{-4} /K [51]. Thus, if we assume $\gamma_{\rm CMRR} = 1/100$, requirement for the temperature stability is

$$\begin{aligned}\delta T_{\rm cav} &\lesssim \frac{10^{-10}\ /\sqrt{\rm Hz}}{1/100\cdot(10^{-7}+8\times10^{-6}+2\times10^{-5})\ /{\rm K}} \\ &= 4\times10^{-4}\ {\rm K}/\sqrt{\rm Hz} \qquad (@\ f_{\rm rot} = 0.083\ {\rm Hz}).\end{aligned} \tag{3.42}$$

This value is typically realized in usual laboratories, and we can say that no special temperature stabilization is needed for our experiment. The measured temperature fluctuation was less than 10^{-4} K/$\sqrt{\rm Hz}$ at 0.1 Hz.

However, in order to go further in the sensitivity, temperature stabilization might be needed. Since the requirement on the temperature fluctuation mainly comes from the thermo-optic effect in silicon, making thermo-optic coefficient smaller also helps. This can be realized by operating the cavity at cryogenic temperature. For example, the thermo-optic coefficient at 20 K is 2 orders of magnitude smaller than that at the room temperature [51].

Cavity tilt fluctuation

If the rotational axis of the turntable and the direction of gravity is not parallel, the tilt of the cavity changes in the rotational period, and the cavity changes its length because of the gravitational deformation. This tilt fluctuation has been a long standing issue for limiting the sensitivity of Michelson-Morley

type experiments. However, this effect is also common to both clockwise and counterclockwise resonances, and this effect won't be a noise source for our experiment in principle.

If we approximate that the shape of the spacer is a cuboid with length of l, and its length is expanded by a gravitational acceleration of $g \sin \delta\varphi$ when the cavity tilt from horizontal plane is $\delta\varphi$, the length change can be written as [52]

$$\frac{\delta l}{l} = \frac{\rho l^2}{2E_{\mathrm{spc}}} g \sin \delta\varphi \tag{3.43}$$

$$\simeq \frac{\rho l^2 g}{2E_{\mathrm{spc}}} \delta\varphi. \tag{3.44}$$

Here, ρ and E_{sub} is the density and the Young's modulus of the spacer.

Therefore, the fluctuation in the resonant frequency difference between counterpropagating directions from the tilt fluctuation is

$$\frac{\delta\nu_{\mathrm{tilt}}}{\nu} \sim \gamma_{\mathrm{CMRR}} \frac{\delta l}{l} = \gamma_{\mathrm{CMRR}} \frac{\rho l^2 g}{2E_{\mathrm{spc}}} \delta\varphi. \tag{3.45}$$

Assuming $\gamma_{\mathrm{CMRR}} = 1/100$, $l \sim L/2$, and $g = 9.8$ m/s^2, and inserting the physical properties of Super Invar in Table 3.2, we get

$$\frac{\delta\nu_{\mathrm{tilt}}}{\nu} \sim 1 \times 10^{-11} \ /\mathrm{rad} \ \delta\varphi. \tag{3.46}$$

Thus, the requirement for the tilt fluctuation is

$$\delta\varphi \lesssim \frac{10^{-10} \ /\sqrt{\mathrm{Hz}}}{1 \times 10^{-11} \ /\mathrm{rad}}$$

$$= 1 \times 10^{1} \ \mathrm{rad}/\sqrt{\mathrm{Hz}} \qquad (@ \ f_{\mathrm{rot}} = 0.083 \ \mathrm{Hz}). \tag{3.47}$$

This requirement is 7 orders of magnitude larger than the requirement for other Michelson-Morley type experiments [24], and we can say that no special tilt control is needed for our experiment. However, tilt also couples into the signal in multiple ways. For example, tilt of the turntable could introduce rotational speed fluctuation in a rotational period. The actual measurement on the tilt

coupling will be discussed in Section 5.4.

Noise from centrifugal force

If the rotational speed fluctuates, the centrifugal force acting on a cavity fluctuates and the resonant frequency fluctuates by the cavity deformation. In principle, this effect is also eliminated by the common mode rejection in our experiment.

The length change of the spacer from centrifugal force can be written in the similar way as Eq. (3.43), by replacing $g \sin \delta\varphi$ with fluctuation in the centrifugal acceraration $\delta(r\omega_{\rm rot}^2)$,

$$\begin{aligned} \frac{\delta l}{l} &= \frac{\rho l^2}{2E_{\rm sub}} \delta(r\omega_{\rm rot}^2) \\ &= \frac{\rho l^2 r \omega_{\rm rot}}{E_{\rm sub}} \delta\omega_{\rm rot}. \end{aligned} \tag{3.48}$$

Therefore, the fluctuation in the resonant frequency difference between counterpropagating directions from the centrifugal force fluctuation is

$$\frac{\delta\nu_{\rm cent}}{\nu} \sim \gamma_{\rm CMRR} \frac{\delta l}{l} = \gamma_{\rm CMRR} \frac{\rho l^2 r \omega_{\rm rot}}{2E_{\rm sub}} \delta\omega_{\rm rot}. \tag{3.49}$$

By assuming $\gamma_{\rm CMRR} = 1/100$ and $r \sim L/2$, and inserting the cavity parameters, we get

$$\frac{\delta\nu_{\rm cent}}{\nu} \sim 8 \times 10^{-14}\ ({\rm rad/sec})^{-1}\ \delta\omega_{\rm rot}. \tag{3.50}$$

Thus, requirement for the rotational speed fluctuation is

$$\begin{aligned} \delta\omega_{\rm rot} &\lesssim \frac{10^{-10}\ /\sqrt{\rm Hz}}{8 \times 10^{-14}\ ({\rm rad/sec})^{-1}} \\ &= 1 \times 10^3\ {\rm rad/sec}/\sqrt{\rm Hz} \qquad (@\ f_{\rm rot} = 0.083\ {\rm Hz}). \end{aligned} \tag{3.51}$$

This requirement is 3 orders of magnitude larger than Eq. (3.31), and the effect from the centrifugal force is sufficiently small.

Electrical noises

Since we use photodetectors, electrical circuits, and electrical devices for acquiring data and feedback control, injection of electrical noises to the Lorentz violation signal is unavoidable. ADC (analog-to-digital converter) noise and aliasing noise could also contribute to the sensitivity of the apparatus. So, we have to carefully design electrical components by estimating the coupling. The noise coupling of each component can be estimated using the method described in Section B.2.

Noises from sound, wind, etc.

Generally, when interferometers are built in air, the vibration from sound and wind will be noise sources. Some amount of these effects will be canceled out by the common mode rejection, but it is better to reduce these effects from the stability point of view for the laser frequency servo.

In our experiment, the optical system including the cavity is placed in a vacuum enclosure at roughly 1 kPa($= 10^{-2}$ atm). This gives not only the soundproofing, but also the temperature stability of the system.

3.4 Summary of this chapter

- We use an optical ring cavity with a silicon piece inside to change the refractive index of the path asymmetrically to search for the parity-odd Lorentz violation.
- The Lorentz violation signal is the resonant frequency difference between the counterclockwise and clockwise directions. We obtain this signal with a double-pass configuration.
- The Lorentz violation signal obtained with a double-pass configuration will be zero when there is no violation. Thus, our experiment is a null experiment.
- Since we do the differential measurement of the resonant frequencies, the noise from the cavity length fluctuations will be canceled out by a

Table 3.3: Summary of requirements and estimations of various noise sources. Requirements and estimations are the values at the cavity rotational frequency 0.083 Hz.

Noise	Req. or est.	Design
Shot noise	4×10^{-16} $/\sqrt{\text{Hz}}$	6 orders of magnitude below requirement
Laser intensity	$\frac{\delta P_0}{P_0} < 1 \times 10^{-1}$ $/\sqrt{\text{Hz}}$	free-run is 2 orders of magnitude below requirement
Laser frequency	$\frac{\delta \nu_{\text{freq}}}{\nu} < 10^{-10}$ $/\sqrt{\text{Hz}}$	need to lock laser frequency on cavity resonance
Sagnac effect	$\delta\omega_{\text{rot}} < 3$ rad/sec$/\sqrt{\text{Hz}}$	stabilize rotational speed with motor control system
Seismic noise	$\gamma_{\text{CMRR}}\gamma_{\text{CMRR}}^{\text{rigid}} \lesssim 10^{-4}$	make a rigid cavity, place optics on a single plate
Thermal noise	1×10^{-15} $/\sqrt{\text{Hz}}$	operation at room temperature
Temperature fluctuation	$\delta T_{\text{cav}} < 4 \times 10^{-4}$ K$/\sqrt{\text{Hz}}$	laboratory environment meets requirement
Tilt fluctuation	$\delta\varphi < 1 \times 10^{1}$ rad$/\sqrt{\text{Hz}}$	no tilt stabilization needed
Centrifugal force	$\delta\omega_{\text{rot}} < 10^{3}$ rad/sec$/\sqrt{\text{Hz}}$	stabilize rotational speed with motor control system
Sound, wind, etc.	-	place optics in a vacuum enclosure

high common mode rejection. Therefore, no special high vacuum environment, high performance vibration isolation system, nor cryogenic operation is needed.

- By rotating the ring cavity, we upconvert the Lorentz violation signal to higher frequency (0.083 Hz) to lower the noise effectively.
- We have estimated the noises from various sources to design the apparatus and set the requirement for the stabilization. The requirements and estimations are summarized in Table 3.3.

Chapter 4
Experimental Setup

Our experimental apparatus consists of the optical system including the ring cavity, turntable, and data acquisition system. In this chapter, we will overview the whole apparatus and describe details of each component. We will also describe the details of the observational data taken for a year.

4.1 Overview

Schematic of the whole experimental setup is shown in Fig. 4.1. We use a single-frequency DFB fiber laser (Koheras AdjustiK C15) with a wavelength of 1550 nm as a laser source. The laser beam is fed into the vacuum enclosure via a polarization maintaining fiber. The beam passes through an isolator to avoid the beam returning into the source, and split into three using two beam splitters, or fiber couplers. Two of three beams are used for monitoring the laser intensity, and the last one is get out of the fiber by a collimator (Thorlabs PAF-X-5-C) and fed into the ring cavity.

The beams for monitoring the laser intensity and the reflected beams from the ring cavity are transduced to the electrical signals by photodetectors (Hamamatsu Photonics G8194) and used as the intensity monitor signals, the frequency servo error signal, and the Lorentz violation signal. The laser source and the vacuum enclosure are fixed on a turntable. The rotation of the turntable is controlled with a personal computer. The Lorentz violation signal and other monitor signals are recorded with a data logger (Yokogawa DL750), and used for data analysis.

The actual photographs of the experimental setup are shown in Appendix E.

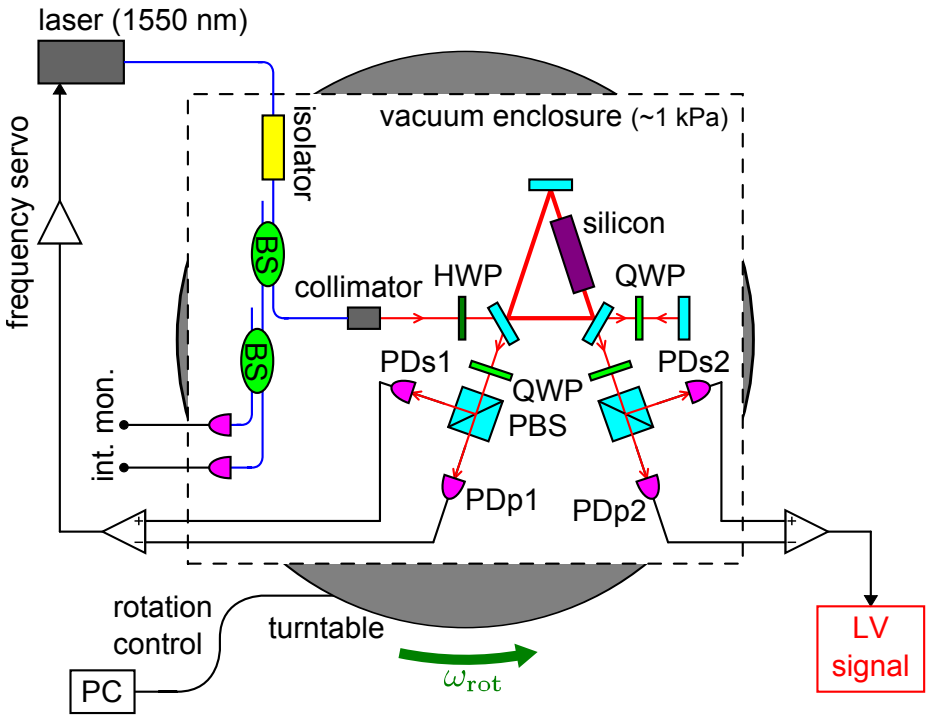

Figure 4.1: Schematic of the whole experimental setup. BS: beam splitter, HWP: half-wave plate, QWP: quarter-wave plate, PBS: polarizing beam splitter. The rotational axis of the turntable is vertical to the optical plane.

4.2 Optical ring cavity

Here, we will discuss the ring cavity design, the optical configuration for obtaining the Lorentz violation signal, and the laser frequency servo. We will also discuss the calibration of the Lorentz violation signal, and show sensitivity level achieved.

4.2.1 Design of the optical ring cavity

Our ring cavity shown in Fig. 4.2 is a triangular cavity constructed from three half-inch mirrors. These mirrors are mechanically fixed on a spacer made of Super Invar. Super Invar is an alloy which has a low thermal expansion constant ($\alpha_{\mathrm{L}} \sim 10^{-7}$ /K). As we have discussed in Section 3.3.5, common mode rejection of effects from vibrations or temperature fluctuation etc. is

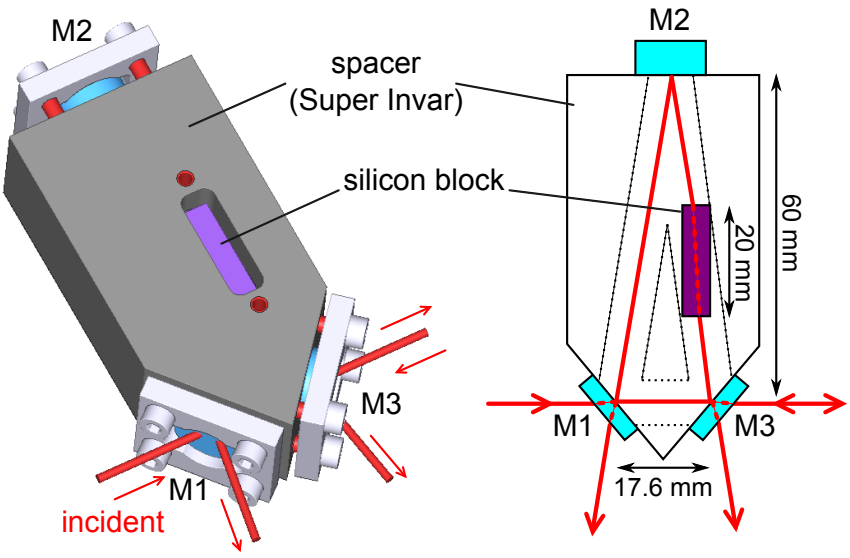

Figure 4.2: Shape and dimensions of the ring cavity.

enhanced, and the frequency lock is expected to be more stable by fixing the mirrors to a spacer.

The spacer has through holes for the optical path. The radii of the holes are 4 mm and the beam radius inside the cavity is 260 μm at maximum (see Fig. 4.4). The spacer also has a hole for placing a silicon piece along one side of the triangle. This silicon piece is rectangular, and its size is 5 mm $\times$ 10 mm $\times$ 20 mm. The edge surfaces of this silicon piece are polished up to the surface figure of $\lambda/10$, and antireflection coated for both polarizations ($r^2 < 0.5\%$/surface). Also, the incident beam to this piece is slightly angled ($\theta_{\rm in} = 9.5°$) in order to avoid the cross-coupling between the counterpropagating beams. The incident angle to the silicon piece is chosen so that the silicon piece is placed parallel to the spacer. The incident angle to the mirror M2 is also 9.5°, and the incident angles to M1 and M3 is 40.25°.

Silicon has high transmittance and a large refractive index (measured value $n = 3.69$) at wavelength $\lambda = 1550$ nm. The round-trip length of our cavity is 14 cm and the designed finesse is about 120 for p-polarized light, with the silicon piece inside the cavity. This finesse is large enough considering the shot noise calculation in Section 3.3.1.

Table 4.1: Parameters of the ring cavity. All values are designed values except for n. r_i values shown are for p-polarized light, and they are lower than those for s-polarized light. $\mathcal{F}$ value shown is the designed value assuming 1% loss at the silicon block. n value shown is for the light at $\lambda = 1550$ nm, and it is the measured by Okamoto Optics.

M1 and M3 amplitude reflectivity	$r_1^2 = r_3^2 = 98\%$
M2 amplitude reflectivity	$r_2^2 > 99\%$
M1 and M3 radius of curvature	$R_1 = R_3 = \infty$ (flat)
M2 radius of curvature	$R_2 = 200$ mm
finesse	$\mathcal{F} = 120$
round-trip length	$L = 140$ mm
silicon length	$d = 20$ mm
silicon refractive index (measured)	$n = 3.69$
free spectral range	$\nu_{\mathrm{FSR}} = 1.5$ GHz
full width at half maximum	$\nu_{\mathrm{FWHM}} = 12$ MHz

The optical parameters of the ring cavity are summarized in Table 4.1. Terminology and treatment of optical cavities are summarized in Section C.1. Also, for example, Refs. [53, 54] give basics of optical cavities.

4.2.2 Optical configuration

The optical setup for obtaining the Lorentz violation signal using the ring cavity is shown in Fig. 4.3.

The laser beam is fed into the ring cavity in the counterclockwise direction via a polarization maintaining fiber. A fiber collimator (Thorlabs PAF-X-5-C) was used to align and mode-match the incident beam to the ring cavity. A polarizing beam splitter (PBS) was placed right after the collimator output in order to suppress the effect from the polarization drift. The incident beam power to the ring cavity is about 1 mW. No external intensity stabilization was employed.

From the cavity reflection of the counterclockwise beam, we get the error signal which is proportional to the difference between the incident laser beam frequency and the counterclockwise resonant frequency. We used the Hänsch-Couillaud method [70, 71], or polarization spectroscopy, to obtain the error

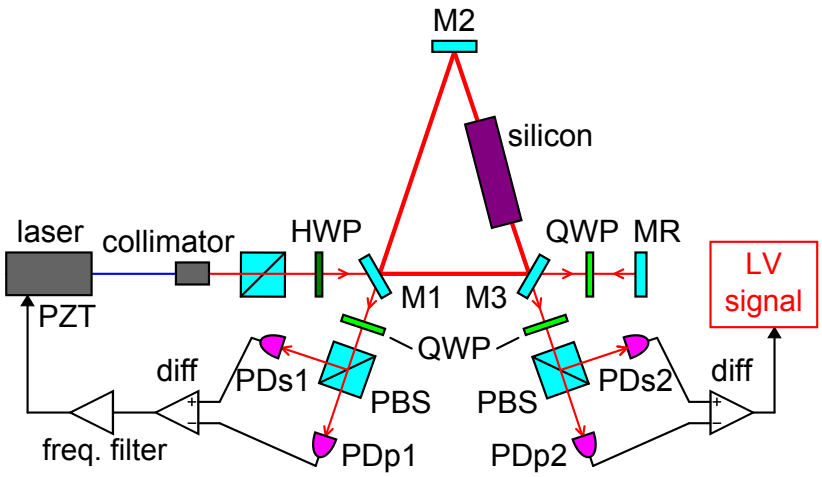

Figure 4.3: The optical setup for obtaining the Lorentz violation signal. HWP: half-wave plate, QWP: quarter-wave plate, PBS: polarizing beam splitter.

signal. The Hänsch-Couillaud method utilizes the polarization selectability of triangular ring cavities. Since there is an odd number of mirror reflections in triangular ring cavities, the resonant frequencies for p-polarization and s-polarization are different. The polarization component which is anti-resonant in the incident beam is created by a half-wave plate (HWP). In our case, the p-polarization beam resonates in the cavity, and s-polarization is anti-resonant. In the cavity reflection, there are a p-polarization beam which went through the cavity, and an s-polarization beam which is directly reflected by an input mirror. So, by taking the interference between those two beams with a quarter-wave plate (QWP) and PBS, we can obtain the error signal about the cavity length with respect to the incident beam frequency. Also, by taking the difference of two PD outputs (PDs1 and PDp1) to obtain an error signal, we reduce the effect of laser intensity fluctuation.

The frequency of the laser beam is stabilized to the counterclockwise resonance using this error signal. The frequency actuator of the laser source used was a piezoelectric actuator attached on the fiber-made laser cavity. A high voltage amplifier (Thorlabs MDT694A) was used to increase the frequency actuation range. The frequency actuation range was 1.3 GHz, which is roughly 1 FSR of the ring cavity. During the observation run, we also manually tuned

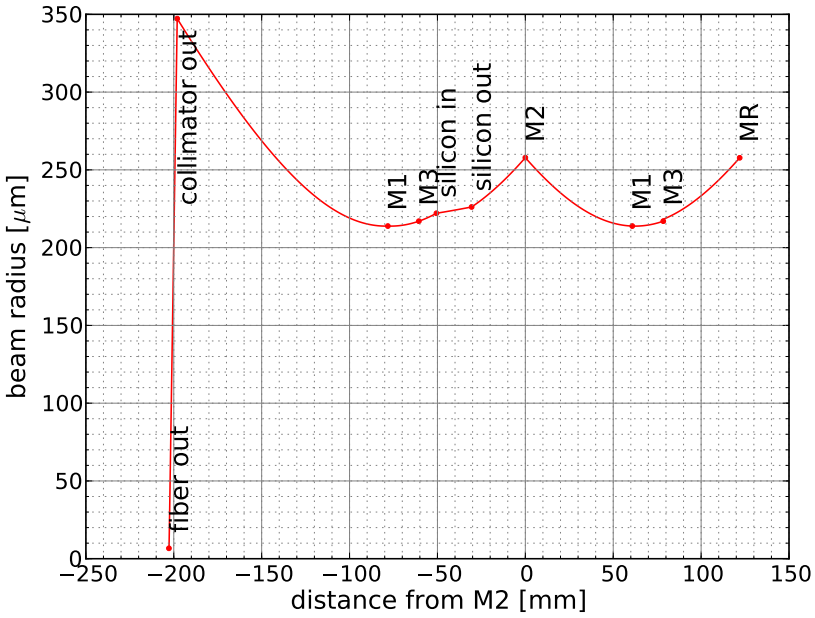

Figure 4.4: Distances between optical components and the beam radius changes. Red dots show the positions of the surfaces of the optics, and the beam radii at those optics. Red dots for mirrors such as M1, M2, M3, and MR, are for HR surfaces of those optics.

the laser frequency once in a while to compensate the frequency drift.

The transmitted light of the counterclockwise beam from the mirror M3 is then reflected back into the cavity in the clockwise direction by a reflection mirror (MR). We obtain the second error signal from the reflection of this clockwise beam. This second error signal is proportional to the resonant frequency difference between both directions, and in this signal we search for the Lorentz violation. To obtain this error signal, we again used the Hänsch-Couillaud method. Our experiment is a null experiment since this error signal will be zero when there is no Lorentz violation.

The principle of the Hänsch-Couillaud method and its advantage in our experiment are summarized in Appendix C. The photodetectors used for the error signals (PDs1, PDp1, PDs2, and PDp2) are all G10899-02K from Hamamatsu Photonics.

The distances between the fiber collimator and the ring cavity, and the ring cavity and the mirror MR is set so that the mode-matching of the beam is maximized. The distances between optical components and the beam radius change along the beam propagation are shown in Fig. 4.4. The radius of curvature of the mirror MR is 200 mm, which is the same as the designed wave front curvature at MR. Generally, the spatial mode of the incident beam and the proper mode of the cavity should be matched to get enough intra-cavity power. See, for example, Refs. [53, 54] for more details.

All the optics are placed in a 30 cm $\times$ 30 cm $\times$ 17 cm vacuum enclosure to realize a stable operation. The vacuum level was $\sim$ 1 kPa at lowest, but since we used sealed-off enclosure and did not evacuated the enclosure continuously, the vacuum level decayed at the time scale of about a few weeks. We did not monitor the vacuum level continuously, and only re-evacuated the enclosure twice during the one-year observation run. This vacuum enclosure is fixed on a turntable together with the laser source, and rotated. The details of the turntable system are discussed in the next section (Section 4.3).

4.2.3 Frequency servo and calibration of the signal

The openloop transfer function of the laser frequency servo is shown in Fig. 4.5. The unity gain frequency (UGF) is 1 kHz, and the phase margin is 80°, which indicate that the servo is stable. The servo bandwidth was limited by the resonance of the piezoelectric actuator at around 23 kHz. This resonance can be considered as a cause of the phase delay at high frequency.

In the Hänsch-Couillaud method, we can obtain the error signal which is proportional to the difference between incident laser beam frequency and the cavity reonant frequency. Using the constant of proportionality for this error signal H [V/Hz], the transfer function of the servo filter F [V/V], and the frequency actuation efficiency of the piezoelectric actuator A [Hz/V], the openloop transfer function can be written as (see Appendix B)

$$G = HFA. \tag{4.1}$$

Since F is the transfer function of the servo filter circuit we made, it is known and independently measurable. Also, A can be measured using an asymmetric

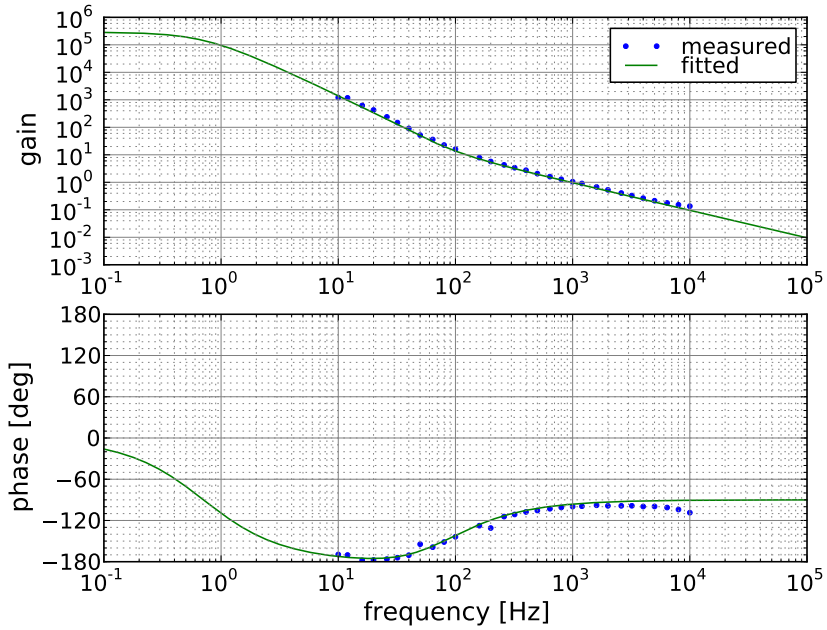

Figure 4.5: Openloop transfer function of the laser frequency servo.

Michelson interferometer (see Appendix D). Thus, by measuring the openloop transfer function G, H can be measured. We used this H to calibrate the error signal in volts to Hz.

This calibration method can also be used to calibrate the Lorentz violation signal. This can be done by measuring the openloop transfer function of the laser frequency lock using the error signal from the difference output of PDs2 and PDp2, not PDs1 and PDp1 (see Fig. 4.3).

4.2.4 Sensitivity of the stationary ring cavity

Figure 4.6 shows the result of the laser frequency servo. The green curve shows the spectrum of the laser frequency noise without any frequency servo, and this spectrum is estimated from the feedback signal of the servo (see Section B.2 for details of the calculation). The blue curve is the spectrum of the error signal used for the laser frequency servo, and the red curve is the spectrum of the Lorentz violation signal. Thus, the red curve shows the sensitivity of

our apparatus for Lorentz violation, and we can see that the noise level is well below the required value, 1×10^{-10} $/\sqrt{\text{Hz}}$ at 0.083 Hz.

If the error signal perfectly reflects the fluctuation of the laser frequency with respect to the ring cavity, the spectrum of the error signal and the Lorentz violation signal should be equal. It is true for the frequency band higher than $\sim$ 70 Hz, and we can say that the residual laser frequency noise is the major noise source for the Lorentz violation signal at the high frequency region. However, at the low frequency region, the noise level for the Lorentz violation signal is higher than the error signal. There are two ways to explain the reason for this:

- Since the error signal is in-loop, the actual residual laser frequency noise could be larger
- Other noises could be introduced when obtaining the Lorentz violation signal

The major noise source to the Lorentz violation signal at the turntable rotation frequency 0.083 Hz is not identified yet at this point. The contributions from the noise from the electrical circuits and the shot noise are sufficiently small and are not limiting the noise level of the Lorentz violation signal. However, note that these spectra are taken when the cavity is not rotated, and the actual sensitivity for the Lorentz violation is determined by the spectra during the cavity rotation. Identifying the noise source for the stationary cavity is not important for improving the sensitivity, since the noise level for the rotating cavity is much worse (see Section 4.3.3).

4.3 Turntable

In our experiment, we illuminate the ring cavity with a laser beam fed from the source via optical fiber. The laser source and the ring cavity are rotated to modulate the Lorentz violation signal. Power to the laser source is supplied and the signals from the cavity are extracted with electrical cables, and we rotated the turntable in positive and reverse directions alternately to avoid the twist of the cables. Also, the rotational speed of the turntable should be

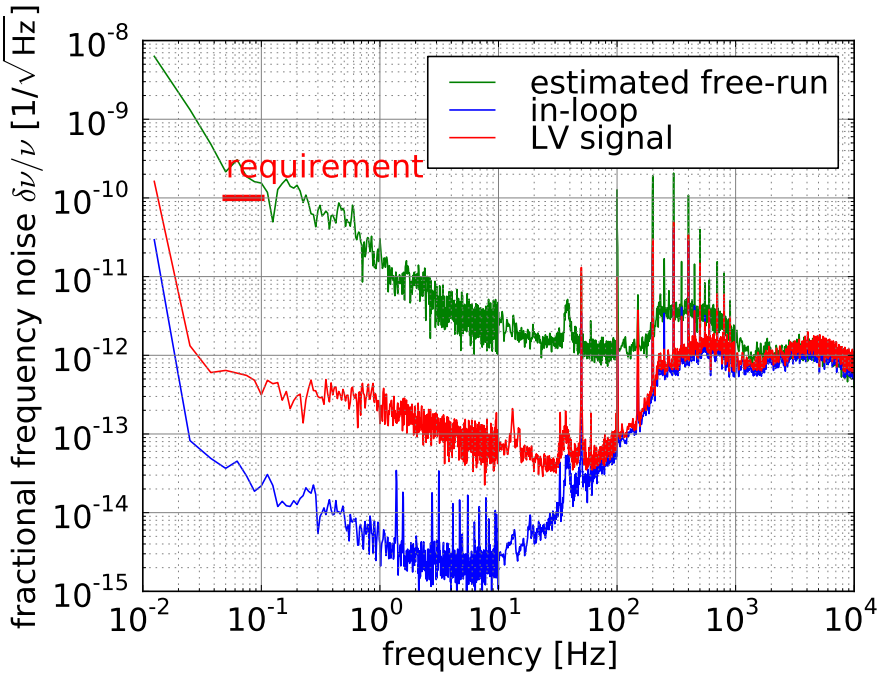

Figure 4.6: Fractional frequency noise spectrum before and after the laser frequency servo, and the noise spectrum of the Lorentz violation signal. The green curve shows the spectrum of the free-running laser frequency noise estimated from the feedback signal, the blue curve shows the spectrum of the in-loop error signal, and the red curve shows the spectrum of the Lorentz violation signal. Note that these spectra are taken when the cavity is stationary.

well controlled to avoid noise from the Sagnac effect (see Section 3.3.4). Such a control of the turntable was done by a commercial motor and its servo system.

In this section, we show the details of the turntable setup and show measured rotational speed fluctuation. We also show the sensitivity to the Lorentz violation signal when the cavity is rotating.

Note that the electric power supply and the data acquisition can also be done even if the cavity is continuously rotated in one direction. Other anisotropy experiments such as Refs. [23, 24] continuously rotated the cavity together with the laser source and data taking instruments. In these cases, they used slip rings to avoid the twist of cables. However, slip rings create electrical noise at the turntable rotational frequency, and we need a larger scale

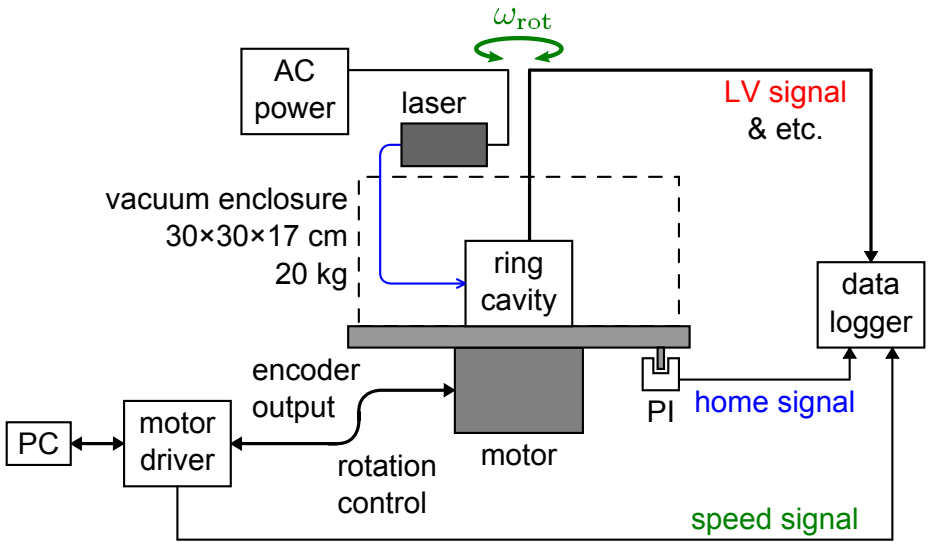

Figure 4.7: Schematic of the turntable and data acquisition system. PI: photointerrupter.

rotational system to avoid this noise. Michelson-Morley type experiments are less sensitive to the noise from slip rings since the Lorentz violation signal appears at twice the turntable rotational frequency.

4.3.1 Setup of the turntable

A schematic of the turntable system is shown in Fig. 4.7. All the optics including the ring cavity is placed inside the vacuum enclosure for sound-proofing etc., and this enclosure is fixed on the turntable. The laser source is also put on top of the enclosure and rotated together with the ring cavity. The vacuum enclosure has the base size of 30 cm × 30 cm, the height of 17 cm, and the mass of the rotating body is approximately 20 kg.

The turntable is rotated with a direct drive servo motor (Nikki Denso NMR-CAUIA2A-151A), and its rotation is controlled by a motor driver (Nikki Denso NCR-CDA1A1A-201D). Positive and reverse rotations of 420° are repeated alternately in order to avoid the twist of the electrical cables hang down from the top of the rotating body. We used thin cables (0.1 mm dia.) for reducing vibrations introduced through the cables. The rotational speed is $\omega_{\rm rot} = 30°/\text{sec}$

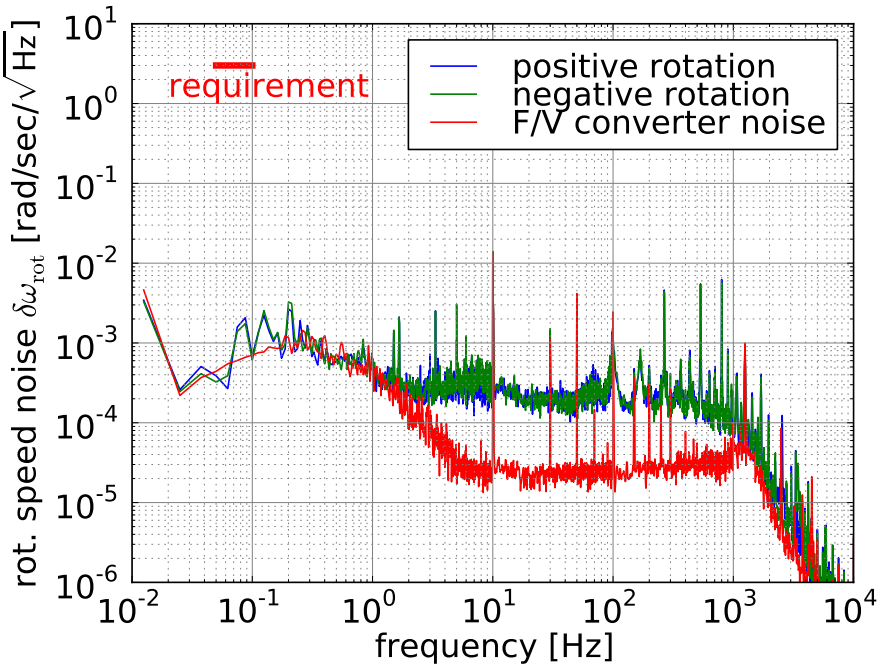

Figure 4.8: Spectra of the rotational speed fluctuation. The blue curve is for positive rotation, the green curve is for reverse rotation, and the red curve is for stationary turntable.

($f_{\rm rot} = 0.083$ Hz), and S-curve acceleration and deceleration were used when flipping the sign of the rotations in order to avoid sudden rotational speed change. We rotated more than 360° in order to keep the rotational speed constant for 360° part in the middle of each rotation.

The motor driver gives torque commands to the motor for controlling the rotational speed by computing the rotation angle and the rotational speed from the output signal from the built-in encoder. The encoder gives 6.4×10^5 pulses (4 multiplication value) per one rotation. The rotation angle and the rotational speed settings are done by writing a code with a personal computer connected to the motor driver.

4.3.2 Rotational speed fluctuation

Figure 4.8 shows the spectra of the rotational speed fluctuation of the turntable controlled by the motor driver. The blue and green curves show the fluctuation when the turntable is continuously rotated at the speed of $\omega_{\rm rot} = 30°/\text{sec}$ ($f_{\rm rot} = 0.083$ Hz), which is used for the Lorentz violation search, in positive and reverse directions, respectively. Here, we define positive rotation as the rotation which the ring cavity rotates in counterclockwise directions when viewed from the zenith. The rotational speed fluctuations in the both directions are well below the required value.

Although there are peaks at the rotational frequency 0.083 Hz and its harmonics in the measured spectrum, we consider that they originated from the encoder itself and not the actual rotational speed fluctuations. The motor has a disc which has slits equiangularly, and by counting the number of slits which pass the sensor per unit time, it measures the rotational speed. This is how the encoder works, but since the distances of the slits are not perfectly even, the noise peaks at the rotational frequency and its harmonics are unavoidable.

We confirmed that the actual rotational speed fluctuation at the rotational frequency is smaller by rotating the turntable without any load. If there are actual rotational speed fluctuations at the rotational frequency, the probable reason for this is because the gravitational force vector acting on the rotating body and the rotation axis is not aligned. So, if we rotate the turntable without any load, the measured rotational speed spectrum should give smaller peaks at the rotational frequency. However, it gave the peaks with the same height.

The red curve in Fig. 4.8 is the spectrum of the rotational speed signal when the turntable was not rotating. This gives the noise level of the frequency to voltage (F/V) converter, which converts the raw encoder output to the rotational speed signal. This F/V converter noise gets larger at the frequency band from 0.1 Hz to 10 Hz, and this limits the measurement at the rotational frequency. So, the actual rotational speed fluctuation could be smaller.

We have also done the rotational speed fluctuation measurement by placing a fiber optic gyroscope (Japan Aviation Electronics JG-201FA) on the turntable. The measured fluctuation was approximately 4×10^{-5} rad/sec at the rotational period, but this measurement was done when the turntable was

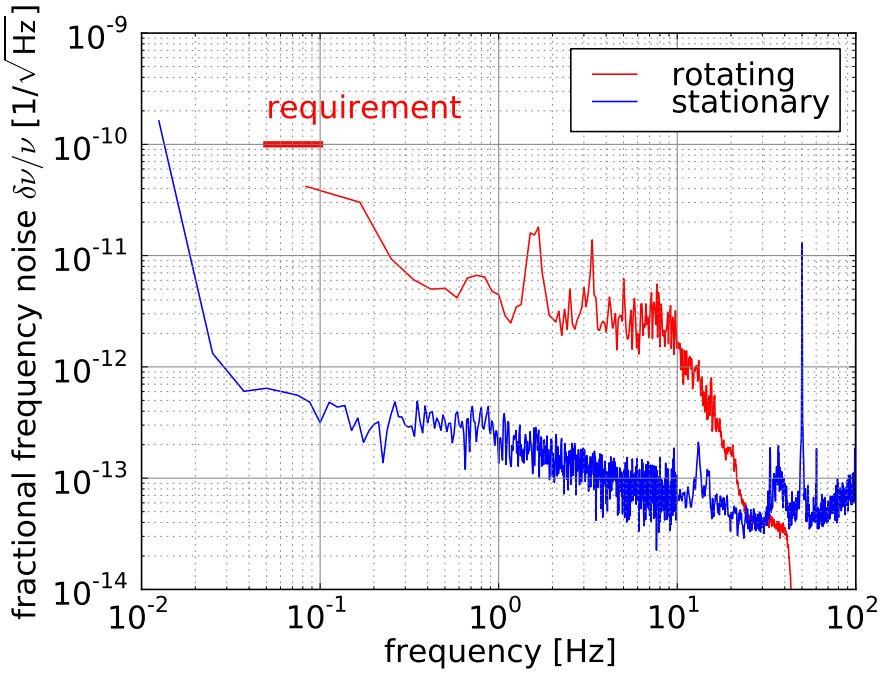

Figure 4.9: Fractional frequency noise spectra of the Lorentz violation signal during the cavity rotation and without cavity rotation. The blue curve is the spectrum when the cavity is not rotated, and the red curve is the spectrum when the cavity is rotated.

rotated at $\omega_{\text{rot}} = 15°/\text{sec}$ to avoid saturation of the gyroscope output. So, the actual rotational speed fluctuation at $\omega_{\text{rot}} = 30°/\text{sec}$ could be larger.

From the above, we have concluded that the rotational speed fluctuation of the turntable used for our experiment is

$$\delta\omega_{\text{rot}} \lesssim 1 \times 10^{-3}\ \text{rad/sec}/\sqrt{\text{Hz}}. \tag{4.2}$$

This is smaller than the required value by more than three orders of magnitude.

4.3.3 Sensitivity during rotations

The typical spectrum of the Lorentz violation signal during the cavity rotation is shown in Fig. 4.9. Compared with the spectrum taken when the turntable is

stationary, the noise level is higher by two orders of magnitude, but typically below the required value. The reason for the higher noise is unidentified at this point, but we think that this is because of the turntable vibration from the rotation. Although the cavity length fluctuations caused by vibrations are canceled out in the double-pass configuration, vibrations of the optics and photodetectors outside the ring cavity are not canceled out, and they create beam jitter into the photodetectors or jitter of the incident beam into the cavity.

To calculate the spectrum during the rotations, we only used an interval of 360° in the middle of each rotation where the rotational speed is constant, since the ring cavity is rotated alternately in two directions. For each rotation, we did Fourier transform of the Lorentz violation signal data and took average over 78 rotations to plot the spectrum in Fig. 4.9. The spectrum plotted is a typical spectrum and the noise level fluctuated over one year of the observation run (see Section 4.5).

Also, even if the spectrum during the rotations meets the requirement, it is important to mitigate the noise which is coherent to the rotational angle. If there is a coherent noise, it will fake the Lorentz violation signal. For example, we used transparent a vacuum enclosure made of acryl resin, and the rotation of the turntable created luminosity change from the room light into the photodetectors. So, we put a shield to the enclosure. Also, we originally did not rotate the laser source and we hang down the optical fiber to put the laser beam into the vacuum enclosure. However, this setup twists the optical fiber and created the coherent noise in the rotational period mainly because of the polarization change. The electrical cables also created the coherent noise, so we changed the cables to thinner cables to reduce vibrations from the cables.

The static tilt of the table also created the coherent noise. The coupling mechanism was not clear, but we think it is because the tilt of the turntable gives the tilt of the rotational axis with respect to the gravity direction. The tilt of the rotational axis creates the tilt fluctuation of the optics in the rotational period. It could also create the rotational speed fluctuation in the rotational period. We used an accelerometer (KISTLER 8302A2) to measure the static tilt and aligned the rotational axis and the gravity direction within approximately 0.01 mrad.

It is important to note that the frequency resolution of the sensitivity spectrum during rotations in Fig. 4.9 is the same as the rotational frequency since the length of the data we used for each Fourier transform is the same as the rotational period. This also worked against our noise hunting. Continuous rotation could be done by using a slip ring to extract the signals from and provide power to the apparatus. However, we did not use a slip ring since slip rings create the noise which is coherent to the rotation.

4.4 Data acquisition system

Since we repeat positive and reverse rotations alternately during the Lorentz violation search, taking the Lorentz violation data only is not sufficient for data analysis. Here, we explain two other main signals we took, and the data taking flow. We will also mention the remote controlling system we used for the year long observation run.

4.4.1 Data taking

To perform a Lorentz violation search, we repeated positive and reverse rotations alternately. When flipping the sign of the rotation, the rotational speed changes and the turntable shakes. So, in order to take clean 360° data for each rotation, we rotated 420° or −420° for each rotation. For data analysis, we only used an interval of 360° in the middle of each rotation where the rotational speed is constant.

In order to split the Lorentz violation signal data into every rotation, we need a signal which tells us that the turntable rotated 360°. As shown in Fig. 4.7, we put a small plate which sticks out of the back surface of the turntable, and made it pass through a transmission type photointerrupter (OMRON EE-SX330) when the turntable rotated 360°. The place of the photointerrupter acts as the origin of the rotation angle, and we called this signal as *home signal*. Note that there exists a similar mechanism in the motor and the rotation control by the driver is done by this built-in home signal. Our home signal with the photointerrupter is an independent signal used only for the data analysis.

We also need the signal which tells us the signs of the rotations. We recorded this rotational speed signal from the motor driver, as well as the home signal and the Lorentz violation signal with a sampling frequency of 500 Hz, by a data logger (Yokogawa DL750). These three continuous signal data were used for the data analysis.

The sampling frequency of 500 Hz was chosen in order to reduce the ADC (analog-to-digital converter) noise, and to avoid the contamination of the aliasing of the 50 Hz line noise. The power spectrum of the ADC noise in voltage can be written as [55]

$$P_{\mathrm{ADC}}(f) = 2\sigma_{\mathrm{rms}}^{\mathrm{ADC}\,2} T_{\mathrm{s}} \left(\frac{\sin(\pi f T_{\mathrm{s}})}{\pi f T_{\mathrm{s}}} \right)^2 , \tag{4.3}$$

where $\sigma_{\mathrm{rms}}^{\mathrm{ADC}}$ is the root mean square of the quantization error, and T_{s} is the sampling time. So, higher sampling frequency gives lower ADC noise. For the Lorentz violation signal channel, we also introduced 3rd-order Butterworth lowpass filter for antialiasing.

Since the sampling frequency of 500 Hz is too high from the point of view of the number of data points, we decimated the raw data into the sampling frequency of 100 Hz. For decimation, we used a MATLAB function, `decimate`, which uses 8th-order Chebyshev type I IIR lowpass filter.

Figure 4.10 is the actual raw data of the three signals acquired during the observation run. 12-sec data taken from one pulse of the home signal to the next pulse are the data for one rotation. The rotational speed signal was used only for checking the signs of the rotations. One cycle of the positive and reverse rotation was about 30 sec including the acceleration and deceleration time.

4.4.2 Remote controlling system

For a long-term operation, we introduced devices and software for remote controlling.

Data taking and the data logger control were done remotely by a PC based software called Wirepuller. Because the data logger we used had small internal storage, we had to stop and extract data every 20 hours. The size of the 20

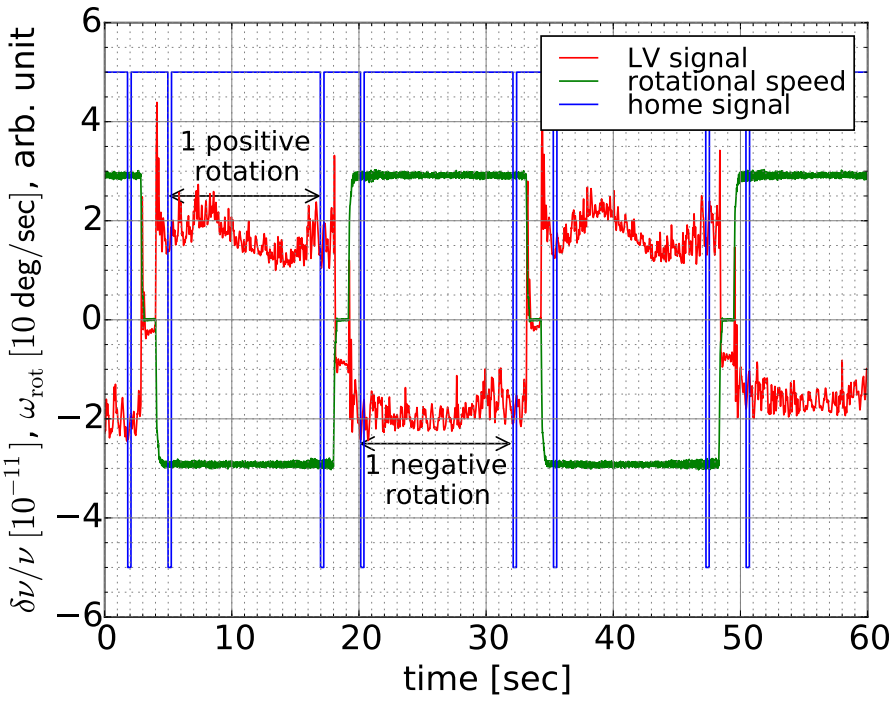

Figure 4.10: Example plot of the raw data of the Lorentz violation signal, the rotational speed signal, and the home signal. The vertical axis is in 10^{-11} for the Lorentz violation signal, in the unit of 10 deg for the rotational speed signal, and in arbitrary unit for the home signal.

hour data was about 720 MB, and downloading took about 15 minutes.

The Lorentz violation data were taken only during the laser frequency was locked to the counterclockwise resonance of the ring cavity. However, the lock was sometimes lost mainly because of the temperature drift. When the feedback signal gets too large and exceed the frequency actuation range, the lock losses. In order to re-lock the frequency again, we had to first turn off the feedback and turn it on with gain boost filters at low frequency again. This was done remotely by using a network based switching device (AVIOSYS IP Power 9258) and relay circuits.

The turntable was monitored by a network camera (TENVIS JPT3185W), and the motor was controlled by a PC based software VCII from Nikki Denso.

4.5 Observational data

The data we used for the analysis were taken at the University of Tokyo for 393 days between July 25, 2012 to October 2, 2013. During the data acquisition, the ring cavity was rotated approximately 1.7×10^6 times.

The number of cavity rotations for each day and the accumulated total are plotted in Fig. 4.11 (above). The intermittent data acquisition was started on July 25, 2012, but the continuous long-term operation was started on October 21, 2012. The number of rotations per day when the laser frequency stayed locked to the cavity resonance for a day was 5.7×10^3. Days with smaller number of rotations were when the frequency lock was lost, the data acquisition error occurred, or other technical issues happened.

Achieved duty cycle for the whole period was 53% and for the period starting from October 21, 2012 was 64%. As we have seen in Section 4.4.1, maximum duty cycle we can archive with our setup is 80%, since there is 3 sec of time loss per rotation for reversing the direction of the cavity rotation. This means that approximately 20% of the time was lost because of the lock-loss or the data acquisition error.

The main cause of lock-losses was the temperature drift, which causes a cavity length drift and a frequency drift. The laser frequency servo keeps the laser frequency to be locked to the cavity resonant frequency by changing the laser cavity length with a piezoelectric actuator. However, if the difference between the original laser frequency and the cavity resonant frequency drifts, the feedback signal to the piezoelectric actuator drifts, and the lock will be lost when the feedback signal exceeds the actuation range.

This issue can be solved by feeding back the signal also to the laser temperature or the cavity temperature. The temperature control loop generally has slower response compared with a piezoelectric actuator loop, but has a larger tunable range. During the operation, we occasionally adjusted the laser temperature manually to relieve the piezoelectric actuator loop, since we did not have a temperature loop. The air-conditioning system in the laboratory also helped to control the temperature of the cavity.

For the data analysis, the Lorentz violation signal is split into intervals of the rotational period, and demodulated at the rotational frequency and

the third harmonics of the rotational frequency. Modulation amplitude uncertainty per rotation for each day is also plotted in Fig. 4.11 (below). Here, the amplitude uncertainty was defined as

$$\Sigma_{m_\mathrm{r}} = \sqrt{N_\mathrm{rot}\left((\sigma[C^C_{m_\mathrm{r}0}])^2 + (\sigma[S^C_{m_\mathrm{r}0}])^2\right)}, \tag{4.4}$$

where N_rot is the number of rotation in the day, and $\sigma[C^C_{m_\mathrm{r}0}]$ and $\sigma[S^C_{m_\mathrm{r}0}]$ are the standard uncertainties of $C^C_{m_\mathrm{r}0}$ and $S^C_{m_\mathrm{r}0}$ for the day, respectively. $C^C_{m_\mathrm{r}0}$ and $S^C_{m_\mathrm{r}0}$ are the modulation amplitudes defined in Eq. (5.23) and Eq. (5.24), and $\sqrt{(C^C_{m_\mathrm{r}0})^2 + (S^C_{m_\mathrm{r}0})^2}$ gives the modulation amplitude at m_r-th harmonics of the rotational frequency.

Σ_1 was typically 2.7×10^{-12} and Σ_3 was typically 1.5×10^{-12}. The noise difference is supposed to be from the difference in the vibration level. The vibration of the turntable is likely to be high at the rotational frequency.

The amplitude uncertainty differs randomly by days, but there are certain periods of days when the amplitude uncertainty is relatively small. We are not sure about the reason, but it might be related to the vacuum level of the enclosure. During the observation run, we have evacuated the enclosure on October 21, 2012, November 1, 2012, and May 24, 2013. As you can see from Fig. 4.11, the amplitude uncertainty somewhat gets smaller after evacuation. We have not done the detailed study about this effect at this point.

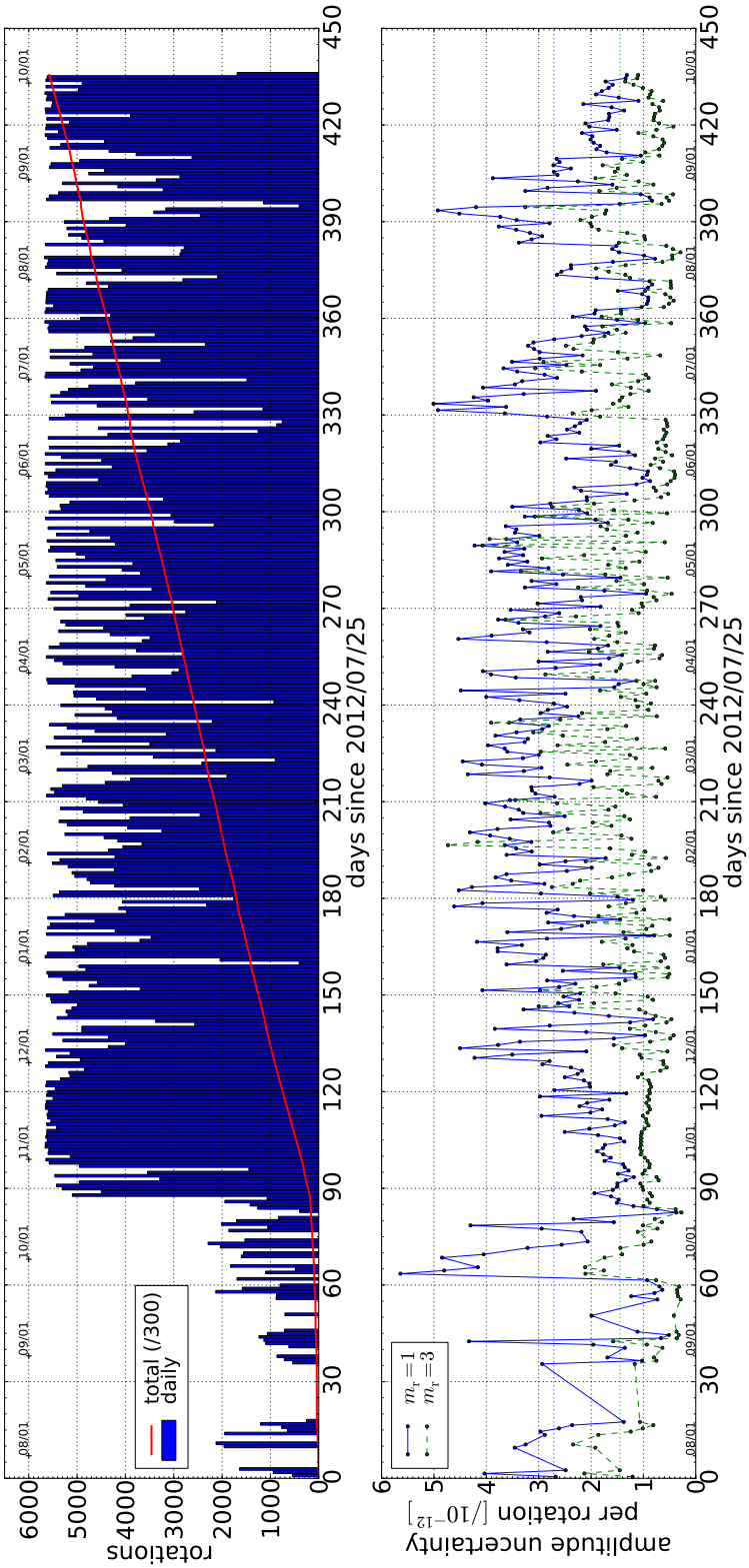

Figure 4.11: Daily number of rotations (above) and amplitude uncertainty per rotation (below). The red curve in the above plot shows the accumulated total number of rotations divided by 300.

4.6 Summary of this chapter

- Our experimental apparatus consists of the optical system including the ring cavity, turntable, and data acquisition system.
- All the components were developed and assembled successfully. The noise requirements to improve the current limits on the parity-odd Lorentz violation were achieved.
- The current frequency noise was limited by the vibration of the turntable during the rotations. The noise level is 2 orders of magnitude larger than that taken when the ring cavity is not rotated.
- Search for the Lorentz violation is performed by rotating the ring cavity in positive and reverse directions alternately.
- The Lorentz violation signal is split into intervals of a rotational period using the home signal. Data analysis will be performed for each rotations.
- The Lorentz violation signal was taken for 393 days between July 2012 and October 2013. During the data acquisition, the ring cavity was rotated approximately 1.7 million times.

Chapter 5
Data Analysis

We have done the analysis of the year-long observational data taken from July 2012 to October 2103. In this chapter, we explain how to extract Lorentz violation parameters from the year-long data. Then, we show the results of our data analysis, and study the systematic uncertainties.

Here, we do the data analysis in the framework of the spherical harmonic decomposition of the light speed anisotropy. However, we have also done the analysis in the framework of the Standard Model Extension. We only show the results here, and the details of the data analysis in the Standard Model Extension will be described in Appendix A.

5.1 Method

The Lorentz violation signal in our experiment is the resonant frequency difference between the clockwise and the counterclockwise directions of the optical ring cavity. If we only consider one dipole component of the anisotropy, the expression of the Lorentz violation signal is given by Eq. (3.5), and it was

$$s(t) = \frac{\delta\nu}{\nu} = \frac{(n-1)d}{L+(n-1)d}\frac{1}{\sqrt{\pi}}\,\overline{y}_1^0\cos\theta. \tag{5.1}$$

Here, θ represents the rotational angle of the cavity. Since the Earth moves around the sun as it rotates on its own axis, we cannot simply replace θ to be $\omega_{\rm rot}t$. In order to compare the limits on $\overline{y}_l^m$ with various experiments, we have to set a frame in which we can reasonably assume that $\overline{y}_l^m$ are constant. The frame most commonly used is SCCEF (sun-centered celestial equatorial frame) [56]. This is because the velocity of SCCEF with respect to the CMB

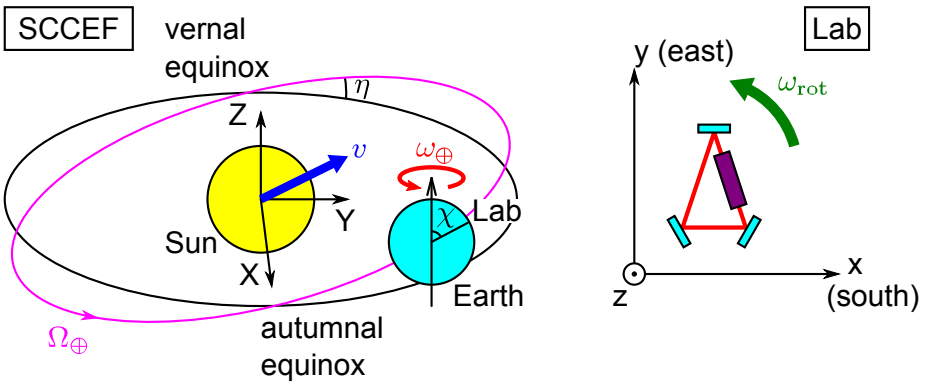

Figure 5.1: SCCEF and the laboratory frame.

rest frame is approximately constant ($v = 369$ km/s [8]). The CMB rest frame is the leading preferred frame candidate, and we can reasonably assume that the Lorentz violation parameters are constant in its inertial frames.

In this section, we first introduce SCCEF, and derive the full formula of the Lorentz violation singal in SCCEF. We then describe how to extract the Lorentz violation parameters $\overline{y}_l^m$ from the measurement data.

5.1.1 Sun centered celestial equatorial frame

As illustrated in Fig. 5.1, the origin of the SCCEF is the sun. The X-axis points toward the Earth at the autumnal equinox, and the Z-axis points toward the north of the axis of rotation of the Earth. The X-Y plane is the same as the equatorial plane of the Earth, and is tilted by $\eta = 23.4°$ with respect to the plane of the revolution of the Earth. From the CMB observation, it is known that the velocity of SCCEF with respect to the CMB rest frame is approximately constant and the velocity is

$$\boldsymbol{v} = v \begin{pmatrix} \cos\psi\cos\varphi \\ \sin\psi\cos\varphi \\ -\sin\psi \end{pmatrix}, \tag{5.2}$$

where $v = 369$ km/s, $\psi = 168°$, and $\varphi = -7.2°$ [8]. Here, ψ and φ is the right ascension and the declination, respectively.

If we set the x-axis of the laboratory frame to point south, and the z-axis to point zenith, the spatial coordinate transformation matrix can be written as [56]

$$R = \begin{pmatrix} \cos\chi\cos\omega_\oplus T_\oplus & \cos\chi\sin\omega_\oplus T_\oplus & -\sin\chi \\ -\sin\omega_\oplus T_\oplus & \cos\omega_\oplus T_\oplus & 0 \\ \sin\chi\cos\omega_\oplus T_\oplus & \sin\chi\sin\omega_\oplus T_\oplus & \cos\chi \end{pmatrix}. \tag{5.3}$$

Here, χ is the colatitude of the laboratory frame, and since we did the experiment in Tokyo (northern latitude of 35.7°), $\chi = 54.3°$. $\omega_\oplus$ is the angular frequency of the Earth rotation, and $T_\oplus$ is the time from the vernal equinox in 2000. $T_\oplus = 0$ is set when the y-axis of the laboratory frame points the same direction as the Y-axis of SCCEF in 2000, and it was 16:30 on March 20, 2000 [57].

5.1.2 Expression of the Lorentz violation signal

To derive the full formula of the Lorentz violation signal, we first consider the expression of the speed of light propagating in the x-y plane of the laboratory frame. If we set the angle between the x-axis and the unit vector along the direction of the propagation of light to be α, the unit vector can be written as

$$\hat{\boldsymbol{e}}_{\rm lab} = \begin{pmatrix} \cos\alpha \\ \sin\alpha \\ 0 \end{pmatrix}. \tag{5.4}$$

Using the transformation matrix R in Eq. (5.3), this vector can be written as

$$\hat{\boldsymbol{e}}_{\rm SCCEF} \equiv \begin{pmatrix} \sin\theta\cos\phi \\ \sin\theta\sin\phi \\ \cos\theta \end{pmatrix} = R^{-1}\hat{\boldsymbol{e}}_{\rm lab}. \tag{5.5}$$

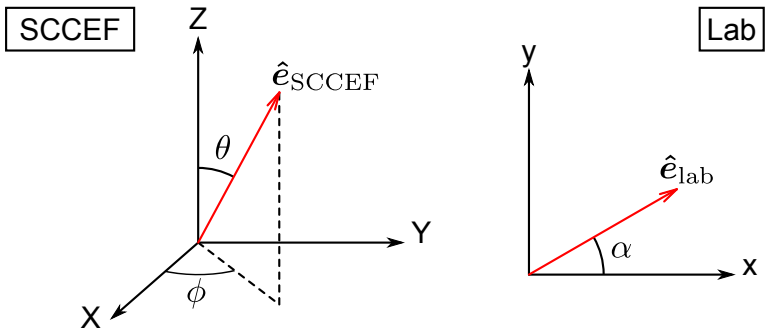

Figure 5.2: Angles indicating the propagation direction of light in the SCCEF and the laboratory frame.

in SCCEF (Fig. 5.2). Thus, the polar angle θ and the azimuthal angle ϕ indicating the direction of the propagation of light are

$$\cos\theta = -\sin\chi\cos\alpha, \tag{5.6}$$

$$\cos\phi = \frac{\cos\chi\cos\omega_{\oplus}T_{\oplus}\cos\alpha - \sin\omega_{\oplus}T_{\oplus}\sin\alpha}{\sqrt{\cos^2\chi\cos^2\alpha + \sin^2\alpha}}, \tag{5.7}$$

$$\sin\phi = \frac{\cos\chi\sin\omega_{\oplus}T_{\oplus}\cos\alpha + \cos\omega_{\oplus}T_{\oplus}\sin\alpha}{\sqrt{\cos^2\chi\cos^2\alpha + \sin^2\alpha}}. \tag{5.8}$$

By treating θ and ϕ as functions of α, the speed of light in the laboratory frame can be expressed as

$$c_{\mathrm{lab}}(\alpha) = c(\theta(\alpha), \phi(\alpha)). \tag{5.9}$$

In particular, the shift in the speed of light from the anisotropy component indicated by l and m in the spherical harmonic decomposition is

$$\delta c_{l\,\mathrm{lab}}^{m}(\alpha) = c_l^m(\theta(\alpha), \phi(\alpha)) - 1 \tag{5.10}$$

$$= \mathrm{Re}\left[(\overline{y}_l^m)^* Y_l^m(\theta(\alpha), \phi(\alpha))\right]. \tag{5.11}$$

Remind that

$$\delta c_{l\,\mathrm{lab}}^{m}(\alpha + \pi) = (-1)^l \delta c_{l\,\mathrm{lab}}^{m}(\alpha) \tag{5.12}$$

follows from the characteristic of the spherical harmonics.

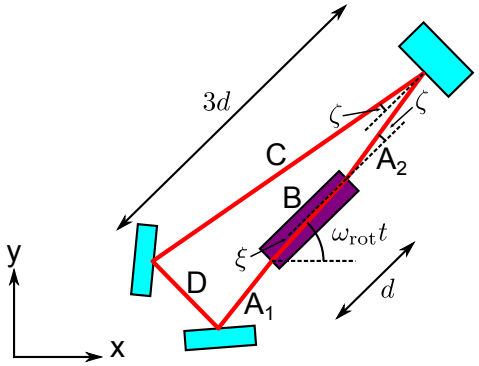

Figure 5.3: Optical ring cavity on the laboratory frame x-y plane.

Now, let's consider a ring cavity placed on the x-y plane as shown in Fig. 5.3. The lengths of the each arm can be written as

$$L_{\mathrm{A}} = L_{\mathrm{A}_1} + L_{\mathrm{A}_2} = \frac{2d}{\cos\zeta} \tag{5.13}$$

$$L_{\mathrm{B}} = \frac{d}{\cos\xi} \tag{5.14}$$

$$L_{\mathrm{C}} = \frac{3d}{\cos\zeta} \tag{5.15}$$

$$L_{\mathrm{D}} = 5d\tan\zeta + d\tan\xi \tag{5.16}$$

Here, $d = 20$ mm and $\zeta = 9.5°$ in our ring cavity, and from Snell's law,

$$\xi = \arcsin\frac{\sin\zeta}{n} \tag{5.17}$$

We can derive the shift in the resonant frequencies similarly to what we have done in Section 3.1.1. The resonant condition for the counterclockwise direction is

$$\begin{aligned}\frac{m}{\nu} = {} & \frac{L_{\mathrm{A}}}{c_{\mathrm{lab}}(\omega_{\mathrm{rot}}t - \xi + \zeta)} + \frac{nL_{\mathrm{B}}}{c_{\mathrm{lab}}(\omega_{\mathrm{rot}}t)} \\ & + \frac{L_{\mathrm{C}}}{c_{\mathrm{lab}}(\omega_{\mathrm{rot}}t - \xi - \zeta - \pi)} + \frac{L_{\mathrm{D}}}{c_{\mathrm{lab}}(\omega_{\mathrm{rot}}t - \xi - \pi/2)}.\end{aligned} \tag{5.18}$$

Here, $t = 0$ is set when the optical path inside the silicon piece is aligned to

the x-axis. The resonant condition when there is no Lorentz violation is

$$\frac{m}{\nu_+} = L_{\rm opt}, \tag{5.19}$$

where $L_{\rm opt} \equiv L_{\rm A} + nL_{\rm B} + L_{\rm C} + L_{\rm D}$ is the round-trip optical path length. By comparing these two equations, the shift in the resonance frequency for the counterclockwise direction is

$$\begin{aligned}\frac{\nu_+ - \nu}{\nu} &= \frac{L_{\rm A}}{L_{\rm opt}}\delta c_{\rm lab}(\omega_{\rm rot}t - \xi + \zeta) + \frac{nL_{\rm B}}{L_{\rm opt}}c_{\rm lab}(\omega_{\rm rot}t) \\ &\quad + \frac{L_{\rm C}}{L_{\rm opt}}\delta c_{\rm lab}(\omega_{\rm rot}t - \xi - \zeta - \pi) + \frac{L_{\rm D}}{L_{\rm opt}}\delta c_{\rm lab}(\omega_{\rm rot}t - \xi - \pi/2).\end{aligned} \tag{5.20}$$

The resonant frequency shift for the clockwise direction can be obtained by reversing the direction of the beam in each arm. This is the same as adding 180° to each α angle. So, by using the symmetry of the spherical harmonics shown in Eq. (5.12), the resonant frequency difference between both directions can be written as

$$\frac{\delta\nu}{\nu} = \frac{\nu_+ - \nu_-}{\nu} = \sum_{l=0}^{\infty}\sum_{m=0}^{l}\left(1 - (-1)^l\right)\left.\frac{\nu_+ - \nu}{\nu}\right|_l^m, \tag{5.21}$$

where $\left.\dfrac{\nu_+ - \nu}{\nu}\right|_l^m$ is the shift from $\overline{y}_l^m$ component of the anisotropy.

The equation above is the expression of our Lorentz violation signal. As it is clear from the expression, the anisotropy components with even l's do not contribute to the signal. This is because of the odd-parity nature of the apparatus and we can only measure $\overline{y}_l^m$ with odd l's.

5.1.3 Extraction of the spherical coefficients from the signal

As we have seen in the previous section, the resonant frequency difference between two counterpropagating directions varies at the frequencies $\omega_{m_{\rm r}m_\oplus} = m_{\rm r}\omega_{\rm rot} + m_\oplus\omega_\oplus$ due to the turntable rotation and the rotation of the Earth. So,

we could perform a direct search for the Lorentz violation by searching for variations at those frequencies. However, a demodulation method is appropriate since $\omega_{\rm rot} \gg \omega_\oplus$.

We first consider a decomposition of the resonant frequency difference into harmonics of $\omega_{\rm rot}$,

$$\frac{\delta\nu}{\nu} = \sum_{m_{\rm r}>0} \left[C_{m_{\rm r}} \cos\left(m_{\rm r}\omega_{\rm rot}t\right) + S_{m_{\rm r}} \sin\left(m_{\rm r}\omega_{\rm rot}t\right)\right]. \tag{5.22}$$

A turntable rotation of 180° effectively interchanges the two counterpropagating solutions, reversing the sign of $\delta\nu/\nu$. This implies that we can concentrate our attention on odd values of $m_{\rm r}$.

The amplitudes $C_{m_{\rm r}}$ and $S_{m_{\rm r}}$ slowly vary at harmonics of the sidereal frequency $\omega_\oplus$ and can be expanded as

$$C_{m_{\rm r}} = \sum_{m_\oplus \geq 0} \left[C^C_{m_{\rm r}m_\oplus} \cos\left(m_\oplus\omega_\oplus T_\oplus\right) + C^S_{m_{\rm r}m_\oplus} \sin\left(m_\oplus\omega_\oplus T_\oplus\right)\right], \tag{5.23}$$

$$S_{m_{\rm r}} = \sum_{m_\oplus \geq 0} \left[S^C_{m_{\rm r}m_\oplus} \cos\left(m_\oplus\omega_\oplus T_\oplus\right) + S^S_{m_{\rm r}m_\oplus} \sin\left(m_\oplus\omega_\oplus T_\oplus\right)\right]. \tag{5.24}$$

Any non-negative $m_\oplus$ can contribute, but the multipole structure of the spherical harmonics predicts that as far as considering the anisotropy up to $l = l_{\rm max}$, we can limit our focus to $0 \leq m_\oplus \leq l_{\rm max}$. In this thesis, we restrict ourselves to $l_{\rm max} = 3$ and consider combinations of $m_{\rm r} = 1, 3$ and $m_\oplus = 0, 1, 2, 3$ only.

The relationship between the spherical coefficients $\overline{y}^m_l$ and these modulation amplitudes can be obtained by demodulating Eq. (5.21). The relation is given in Table 5.1. By demodulating the Lorentz violation signal, we can extract the Lorentz violation parameters.

Note that the silicon piece provides additional asymmetry that increases the number of spherical coefficients that can be accessed by our experiment. The calculation shows that without the silicon, we lose sensitivity to all $l = 1$ coefficients. It also reduces the number of $l = 3$ coefficients that can be measured. The loss in the sensitivity comes from the fact that dipole effects cancel around a closed path without matter.

Also, as we can see from Table 5.1, modulation amplitudes with $m_\oplus = 0$

Table 5.1: The relationship between the nonzero modulation amplitudes and the spherical coefficients $\overline{y}_l^m$. The numbers m_r and $m_\oplus$ represent the harmonics of the turntable rotation frequency and sidereal frequency.

m_r	$m_\oplus$	$C^C_{m_\mathrm{r}m_\oplus}$	$C^S_{m_\mathrm{r}m_\oplus}$	$S^C_{m_\mathrm{r}m_\oplus}$	$S^S_{m_\mathrm{r}m_\oplus}$
1	0	$-0.22\ \overline{y}_1^0$	-	0	-
		$+0.089\ \overline{y}_3^0$			
1	1	$0.11\mathrm{Re}[\overline{y}_1^1]$	$0.11\mathrm{Im}[\overline{y}_1^1]$	$0.19\mathrm{Im}[\overline{y}_1^1]$	$-0.19\mathrm{Re}[\overline{y}_1^1]$
		$+0.16\mathrm{Re}[\overline{y}_3^1]$	$+0.16\mathrm{Im}[\overline{y}_3^1]$	$-0.032\mathrm{Im}[\overline{y}_3^1]$	$+0.032\mathrm{Re}[\overline{y}_3^1]$
1	2	$-0.0025\mathrm{Re}[\overline{y}_3^2]$	$-0.0025\mathrm{Im}[\overline{y}_3^2]$	$-0.14\mathrm{Im}[\overline{y}_3^2]$	$0.14\mathrm{Re}[\overline{y}_3^2]$
1	3	$-0.067\mathrm{Re}[\overline{y}_3^3]$	$-0.067\mathrm{Im}[\overline{y}_3^3]$	$-0.12\mathrm{Im}[\overline{y}_3^3]$	$0.12\mathrm{Re}[\overline{y}_3^3]$
3	0	$-0.17\ \overline{y}_3^0$	-	$0.18\ \overline{y}_3^0$	-
3	1	$0.10\mathrm{Re}[\overline{y}_3^1]$	$-0.19\mathrm{Re}[\overline{y}_3^1]$	$-0.11\mathrm{Re}[\overline{y}_3^1]$	$-0.18\mathrm{Re}[\overline{y}_3^1]$
		$+0.19\mathrm{Im}[\overline{y}_3^1]$	$+0.10\mathrm{Im}[\overline{y}_3^1]$	$0.18\mathrm{Im}[\overline{y}_3^1]$	$-0.11\mathrm{Im}[\overline{y}_3^1]$
3	2	$-0.19\mathrm{Re}[\overline{y}_3^2]$	$0.17\mathrm{Re}[\overline{y}_3^2]$	$0.20\mathrm{Re}[\overline{y}_3^2]$	$0.16\mathrm{Re}[\overline{y}_3^2]$
		$-0.17\mathrm{Im}[\overline{y}_3^2]$	$-0.19\mathrm{Im}[\overline{y}_3^2]$	$-0.16\mathrm{Im}[\overline{y}_3^2]$	$0.20\mathrm{Im}[\overline{y}_3^2]$
3	3	$0.14\mathrm{Re}[\overline{y}_3^3]$	$-0.15\mathrm{Re}[\overline{y}_3^3]$	$-0.14\mathrm{Re}[\overline{y}_3^3]$	$-0.14\mathrm{Re}[\overline{y}_3^3]$
		$+0.15\mathrm{Im}[\overline{y}_3^3]$	$+0.14\mathrm{Im}[\overline{y}_3^3]$	$+0.14\mathrm{Im}[\overline{y}_3^3]$	$-0.14\mathrm{Im}[\overline{y}_3^3]$

give $\overline{y}_l^m$ with $m = 0$. So, without the turntable rotation, we cannot access to there coefficients. This is because of the symmetric structure of $m = 0$ components around the Z-axis of the SCCEF. The effect from $m = 0$ anisotropy will not be modulated by the Earth's rotation, since the Z-axis is parallel to the Earth's rotational axis.

5.2 Results

The analysis starts by demodulating the data at frequencies ω_rot and $3\omega_\mathrm{rot}$ to extract the amplitudes C_{m_r} and S_{m_r} in Eq. (5.22) for each rotation. We only used an interval of 360° in the middle of each 420° rotation where the rotational speed is constant. The demodulation was done by least-squares fit

to Eq. (5.22). For negative rotation, we used $-\omega_{\rm rot}$ and $-3\omega_{\rm rot}$ instead of $\omega_{\rm rot}$ and $3\omega_{\rm rot}$ to extract the amplitudes.

Time series data of $C_{m_{\rm r}}$ and $S_{m_{\rm r}}$ are split into one-day intervals and fit to Eq. (5.23) and Eq. (5.24) by the least squares method to extract the modulation amplitudes $C^C_{m_{\rm r}m_\oplus}, C^S_{m_{\rm r}m_\oplus}, S^C_{m_{\rm r}m_\oplus}$, and $S^S_{m_{\rm r}m_\oplus}$ for each day. The results are shown in Fig. 5.4 and Fig. 5.5 as pairs of quadratic amplitudes.

Taking the weighted average over the 393 days gives our measured values for the modulation amplitudes, which are listed in Table 5.2. The weight were calculated using the standard uncertainties of the modulation amplitudes for each day, which can be derived from the least squares method. We obtained standard uncertainties of $\sim 1 \times 10^{-15}$ for $m_{\rm r} = 1$ amplitudes, and $\sim 6 \times 10^{-16}$ for $m_{\rm r} = 3$ amplitudes. No deviation from zero by more than 2σ was found. Thus, we conclude that no significant evidence for anisotropy in the speed of light in a sidereal frame can be claimed from our data.

Figure 5.6 and 5.7 show histograms for each modulation amplitude. Compared with a normal distribution, each distribution has an excess tail. The origin of this non-Gaussian component is unidentified yet, but we guess this is from nonstationary or transient vibrations from the turntable or the cables. The statistical uncertainties could be reduced by identifying and mitigating this non-Gaussian noise.

The level of non-Gaussianity can be somewhat quantified by a kurtosis parameter. Kurtosis (or excess kurtosis) is defined as

$$\beta_2 = \frac{\mu_4}{\sigma^4} - 3, \tag{5.25}$$

where μ_4 is the fourth moment about the mean and σ is the standard deviation. When there is a large excess tail, β_2 will be positive and large. β_2 is zero for a normal distribution, but the distributions of our modulation amplitudes give a few tens of β_2, as shown in Fig. 5.6 and Fig. 5.7.

To get constraints on the Lorentz violation parameters $\overline{y}^m_l$, we used the relationship between the modulation amplitudes and $\overline{y}^m_l$, which is shown in Table 5.1. The results are summarized in Table 5.3. We obtained standard uncertainties of $\sim 6 \times 10^{-15}$ for $l = 1$ coefficients, and $\sim 2 \times 10^{-15}$ for $l = 3$ coefficients. Note that the coefficients $\overline{y}^m_l$ with $m \neq 0$ are complex, so

we bounnd both the real and imaginary parts. The uncertainties on $l = 1$ coefficients are larger than those of $l = 3$ components. This stems from the noise difference at the rotational frequency ω_{rot} and at $3\omega_{\mathrm{rot}}$.

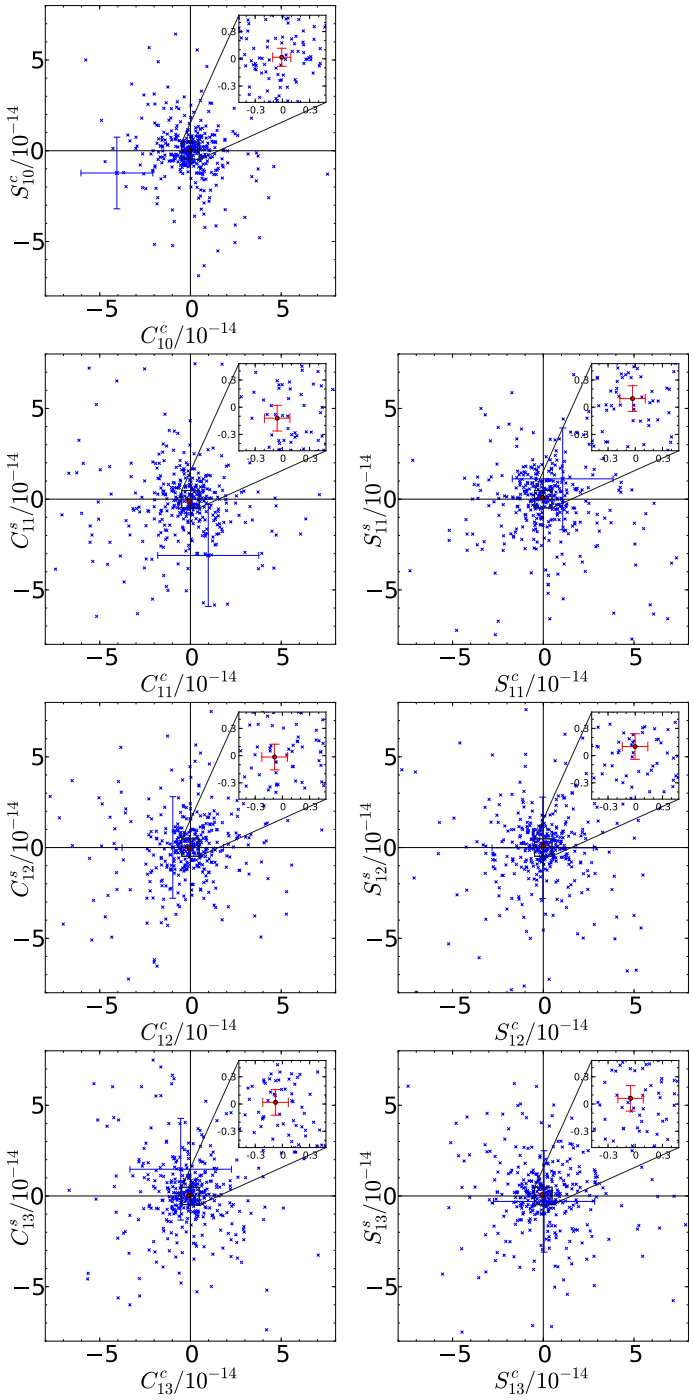

Figure 5.4: Modulation amplitudes for $m_\mathrm{r} = 1$. For clarity, the error bars are omitted except for one data point to indicate the typical standard uncertainties. The mean values of all 393 points are shown as red dots.

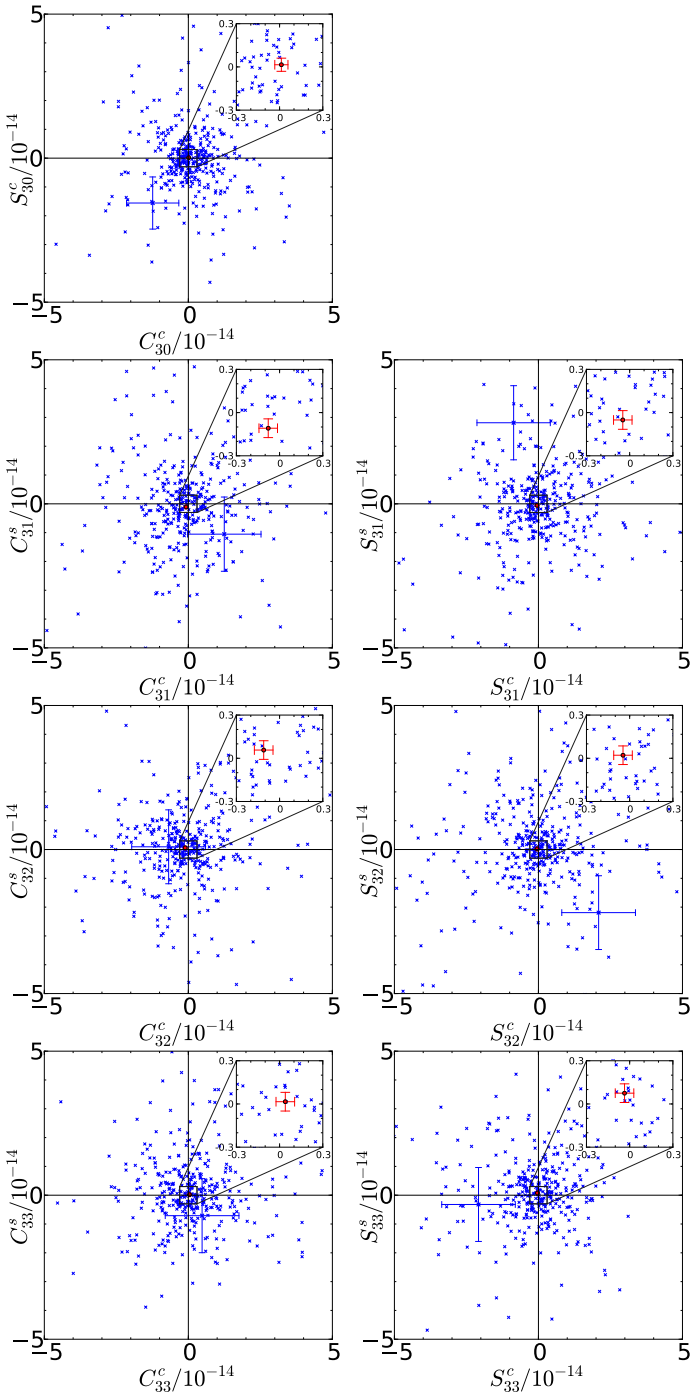

Figure 5.5: Modulation amplitudes for $m_\mathrm{r} = 3$. For clarity, the error bars are omitted except for one data point to indicate the typical standard uncertainties. The mean values of all 393 points are shown as red dots.

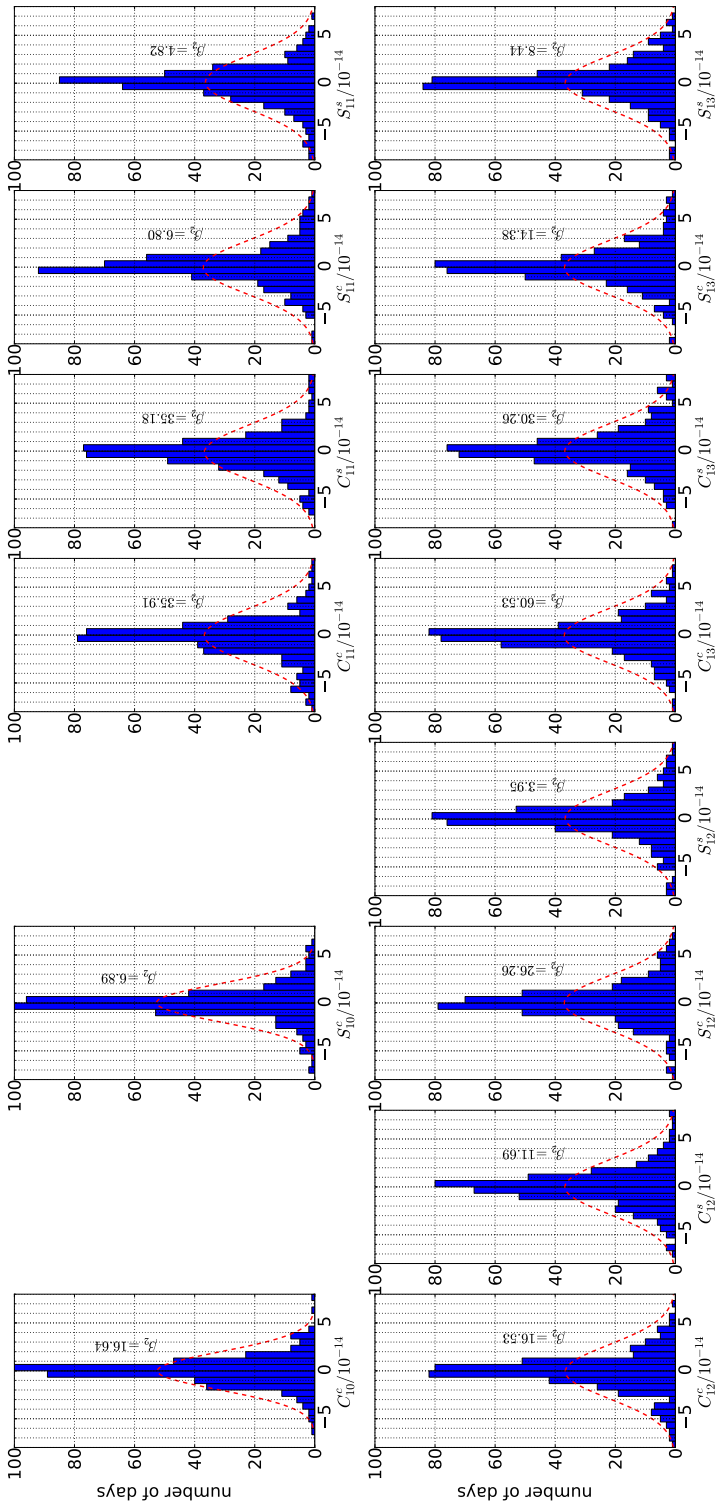

Figure 5.6: Histgrams for modulation amplitudes for $m_{\mathrm{r}} = 1$. Red dashed line shows the normal distribution using the weighted average and the weighted standard deviation for each amplitude. Excess kurtoses β_2 for each amplitude are also shown.

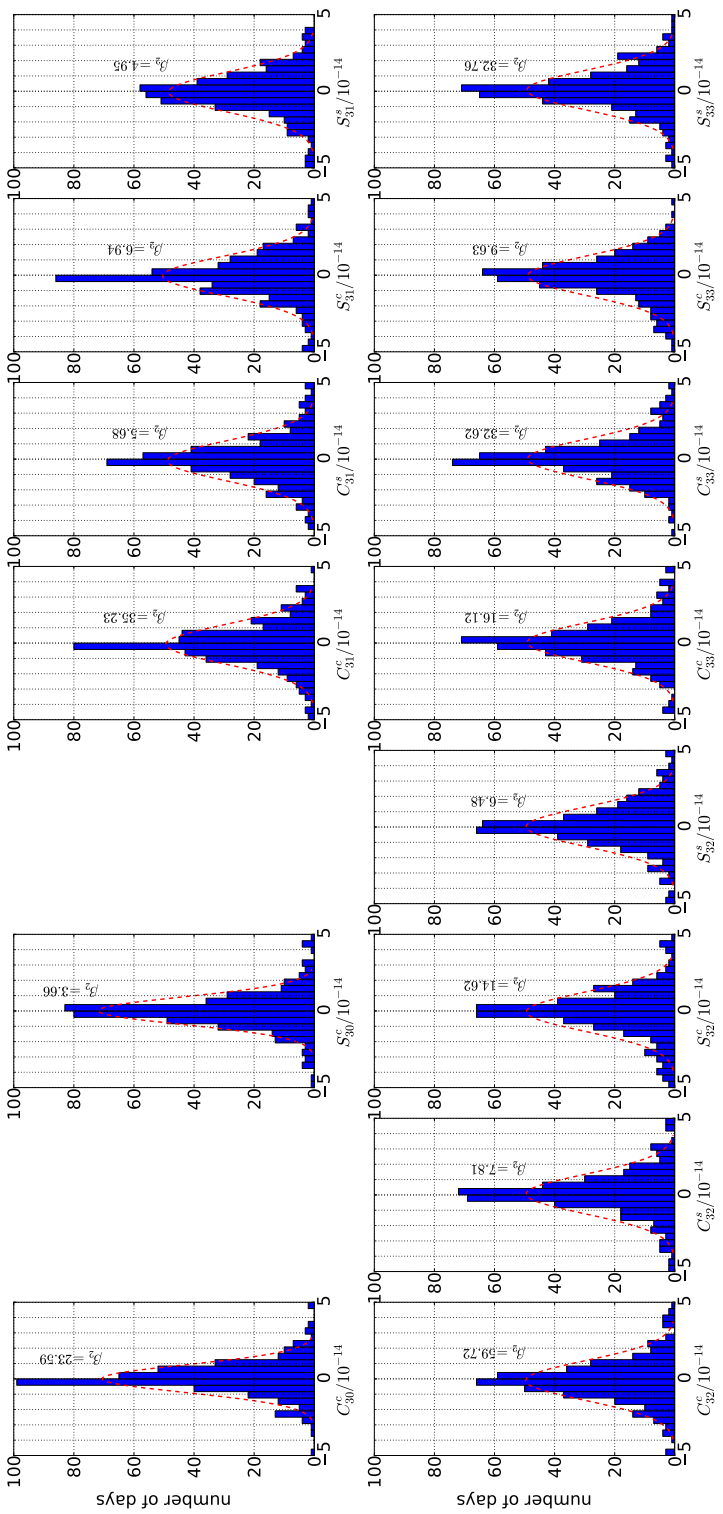

Figure 5.7: Histgrams for modulation amplitudes for $m_\mathrm{r} = 3$. Red dashed line shows the normal distribution using the weighted average and the weighted standard deviation for each amplitude. Excess kurtoses β_2 for each amplitude are also shown.

Table 5.2: Constraints on the $\delta\nu/\nu$ modulation amplitudes for $m_{\rm r} = 1, 3$ and $m_\oplus = 0, 1, 2, 3$. All values are in units of 10^{-15}.

$m_{\rm r}$	$m_\oplus$	$C^C_{m_{\rm r}m_\oplus}$	$C^S_{m_{\rm r}m_\oplus}$	$S^C_{m_{\rm r}m_\oplus}$	$S^S_{m_{\rm r}m_\oplus}$
1	0	-0.1 ± 1.0	-	0.2 ± 1.0	-
1	1	-0.6 ± 1.4	-1.2 ± 1.4	-0.3 ± 1.4	1.0 ± 1.4
1	2	-0.9 ± 1.4	-0.2 ± 1.4	-0.1 ± 1.4	1.0 ± 1.4
1	3	-0.8 ± 1.4	0.2 ± 1.4	-0.5 ± 1.4	0.6 ± 1.4
3	0	0.12 ± 0.46	-	0.15 ± 0.46	-
3	1	-0.79 ± 0.64	-1.1 ± 0.65	-0.48 ± 0.64	-0.51 ± 0.65
3	2	-1.1 ± 0.65	0.57 ± 0.65	-0.46 ± 0.65	0.21 ± 0.65
3	3	0.40 ± 0.65	0.16 ± 0.65	-0.36 ± 0.64	0.75 ± 0.65

Table 5.3: Spherical coefficients with 1σ uncertainties determined from this work. All values are in units of 10^{-15}.

Coefficient	Measurement
$\overline{y}^0_1$	0.4 ± 4.4
$\mathrm{Re}[\overline{y}^1_1]$	-5.7 ± 6.3
$\mathrm{Im}[\overline{y}^1_1]$	-3.2 ± 6.2
$\overline{y}^0_3$	0.1 ± 1.9
$\mathrm{Re}[\overline{y}^1_3]$	2.9 ± 2.2
$\mathrm{Im}[\overline{y}^1_3]$	-3.2 ± 2.1
$\mathrm{Re}[\overline{y}^2_3]$	2.1 ± 1.8
$\mathrm{Im}[\overline{y}^2_3]$	1.5 ± 1.8
$\mathrm{Re}[\overline{y}^3_3]$	-0.2 ± 2.2
$\mathrm{Im}[\overline{y}^3_3]$	-0.7 ± 2.2

In terms of $\delta c/c$, our upper limits are more than an order of magnitude better than the previous best limit from a cavity experiment [33], and are comparable with the previous best limit from a Compton scattering experiment [35]. See Table 2.1 for comparison of limits from previous experiments.

Compared with the Compton scattering experiment, our experiment can measure coefficients with $m = 0$, since we rotate the ring cavity. As discussed in the previous section, the Compton scattering experiment only uses the Earth's rotation alone, and thus cannot access $m = 0$ coefficients. Also, since we did the phase sensitive demodulation for the data analysis. Thus, we could put bounds on all the parity-odd coefficients up to $l = 3$.

5.3 Results in the framework of the SME

We have also done the analysis in the framework of the SME. The method is the same as the one we have used in the previous sections. The relationship between the modulation amplitudes and the SME coefficients are summarized in Table A.2, and the derivation is described in Appendix A. Here we restrict ourselves to consider the camouflage coefficients of dimensions $d = 6$ and $d = 8$.

To get constraints on the SME coefficients, we consider each dimension $d = 6$ and $d = 8$ separately and place constraints under the assumption that only one of the two sets of coefficients is nonzero.

The results are summarized in Table 5.4. For $d = 6$, there is a total of 3 parity-odd camouflage coefficients, and our experiment constrains the entire coefficient space accessible to parity-odd cavity experiments. For $d = 8$, we find that 10 combinations of coefficients contribute to the modulations of the frequency difference $\delta\nu/\nu$, and we got 10 bounds on those combinations. There is a total of 13 parity-odd camouflage coefficients for $d = 8$, so 3 linear combinations of coefficients remain untested. These may be accessed by future ring cavity experiments with different configurations, yielding sensitivities to different combinations of coefficients.

The results in Table 5.4 are the first bounds on parity-odd camouflage coefficients for the Lorentz violation. The current best bounds on the parity-even coefficients come from the microwave cavity experiment in Ref. [66]. While this experiment and our experiment probe two independent sets of Lorentz

Table 5.4: SME camouflage coefficients with 1σ uncertainties determined from this work.

Dimension	Coefficient	Measurement
$d = 6$	$(\overline{c}_F^{(6)})_{110}^{(0E)}$	$(-0.1 \pm 1.5) \times 10^3$ GeV^{-2}
	$\mathrm{Re}[(\overline{c}_F^{(6)})_{111}^{(0E)}]$	$(-0.8 \pm 1.1) \times 10^3$ GeV^{-2}
	$\mathrm{Im}[(\overline{c}_F^{(6)})_{111}^{(0E)}]$	$(-0.6 \pm 1.0) \times 10^3$ GeV^{-2}
$d = 8$	$-0.020(\overline{c}_F^{(8)})_{110}^{(0E)} + (\overline{c}_F^{(8)})_{310}^{(0E)}$	$(-0.2 \pm 1.9) \times 10^{19}$ GeV^{-4}
	$\mathrm{Re}[-0.020(\overline{c}_F^{(8)})_{111}^{(0E)} + (\overline{c}_F^{(8)})_{311}^{(0E)}]$	$(1.4 \pm 1.3) \times 10^{19}$ GeV^{-4}
	$\mathrm{Re}[-0.020(\overline{c}_F^{(8)})_{111}^{(0E)} + (\overline{c}_F^{(8)})_{311}^{(0E)}]$	$(0.1 \pm 1.3) \times 10^{19}$ GeV^{-4}
	$(\overline{c}_F^{(8)})_{330}^{(0E)}$	$(-0.8 \pm 3.3) \times 10^{19}$ GeV^{-4}
	$\mathrm{Re}[(\overline{c}_F^{(8)})_{331}^{(0E)}]$	$(-0.3 \pm 1.9) \times 10^{19}$ GeV^{-4}
	$\mathrm{Im}[(\overline{c}_F^{(8)})_{331}^{(0E)}]$	$(-2.8 \pm 1.9) \times 10^{19}$ GeV^{-4}
	$\mathrm{Re}[(\overline{c}_F^{(8)})_{332}^{(0E)}]$	$(2.2 \pm 1.3) \times 10^{19}$ GeV^{-4}
	$\mathrm{Im}[(\overline{c}_F^{(8)})_{332}^{(0E)}]$	$(0.2 \pm 1.3) \times 10^{19}$ GeV^{-4}
	$\mathrm{Re}[(\overline{c}_F^{(8)})_{333}^{(0E)}]$	$(-0.1 \pm 1.6) \times 10^{19}$ GeV^{-4}
	$\mathrm{Im}[(\overline{c}_F^{(8)})_{333}^{(0E)}]$	$(-0.1 \pm 1.6) \times 10^{19}$ GeV^{-4}

violations, the sensitivity was improved by closer to a factor of a million for $d = 6$, and a factor of 10^{14} for $d = 8$ violations. See Table A.1 for comparison of limits from the previous experiment.

The radical increase in the sensitivity results from higher frequencies. While their experiment used a microwave with the frequency of 10 GHz, we used the optical laser with the frequency of 200 THz. Naive estimates in Section A.1.2 suggest improvements of roughly 8 orders of magnitude for $d = 6$ and 16 orders of magnitude for $d = 8$ may be possible. An achieved improvement factor was a bit less because their sensitivity was at $\delta c/c \lesssim 10^{-16}$ level, whereas ours was at 10^{-15} level.

5.4 Systematic uncertainties

A number of systematic effects was studied. A major cause of the systematic offset was the tilt of the base of the turntable. As we have discussed in Section 3.3.5, the tilt does not couple into the Lorentz violation signal, but it did in real when the tilt is large. The coupling mechanism was not clear, but the tilt of the fiber collimator could create a slight change in the alignment of the incident beam into the cavity. Also, the tilt of the photodetectors could create the fake signal due to ununiformity of the quantum efficiency. If the tilt fluctuates in $1/m_{\oplus}$ of a sidereal period, it will give a systematic offset to the resulting Lorentz violation coefficients. The measured tilt stayed within 0.2 mrad and this effect was less than 10% of our statistical uncertainty. The effect was estimated by intentionally tilting the table and measuring the coupling factor.

The tilt was measured with an accelerometer (KISTLER 8302A2). The temperature was also recorded simultaneously with a temperature sensor (Texas Instruments LM35). The tilt and the temperature both showed similar drift in a sidereal period. Thus, we guess that the tilt change was induced by the temperature change. The relation between the tilt and the temperature was approximately 1 mrad/K.

The Sagnac effect also gives systematic offset to the modulation amplitudes if the rotational speed of the turntable fluctuates in $1/m_{\oplus}$ of a sidereal period. However, the measured fluctuation was less than 1 mrad/sec, and this effect was less than 2% of our statistical uncertainty. The rotational speed was measured with a fiber optic gyro (Japan Aviation Electronics JG-201FA).

Another type of a systematic uncertainty is a calibration uncertainty, which does not fake the Lorentz violation signal, but changes the magnitude of our limits on the Lorentz violation. There was a slight drift in the calibration factor for the Lorentz violation signal, which originated from slight detuning in the laser frequency servo. This detuning was supposed to be introduced by the polarization drift of the incident beam. This is because the change in the polarization state of the incident beam changes the zero crossing point of the error signal (see Appendix C). We have introduced a PBS to reduce this drift, but slight rotations in waveplates could also create the polarization change. The detuning can be monitored from the offset level of the acquired data and

this calibration uncertainty was estimated to be 3%.

As we have seen in Section 4.2.3, the uncertainty in the measurement of the openloop transfer function G and the frequency actuation efficiency of the piezoelectric actuator A also gives calibration uncertainty. The uncertainty was estimated to be 3% and 5% for the measurement of G and A, respectively (see Appendix D).

Systematic uncertainties are summarized in Table 5.5. Other minor calibration uncertainties due to the uncertainties in the silicon refractive index and optical path lengths are also shown. The calibration uncertainty was 7% in total.

There were also uncertainties in the orientation of the cavity with respect to the SCCEF. This is due to timing uncertainty in data acquisition, and uncertainty in the orientation of the cavity with respect to the laboratory frame, in which x-axis points south. The effect from the orientation uncertainty is zero when the noise is purely Gaussian and quadratic modulation amplitudes have equal standard deviation. However, due to slight ellipticity, orientation uncertainty affects the statistical uncertainty on the Lorentz violation coefficients. Our calculation shows that the effect is negligibly small, as summarized in Table 5.5.

5.5 Summary of this chapter

- By demodulating the Lorentz violation signal with the turntable rotation frequency and the sidereal frequency, we obtained the modulation amplitudes.

- We extracted the spherical coefficients $\overline{y}_l^m$ from the modulation amplitudes.

- No significant Lorentz violation was found at the $\delta c/c \lesssim 10^{-15}$ level, and put limits on $\overline{y}_l^m$ at $\sim 6 \times 10^{-15}$ level for $l = 1$, and at $\sim 2 \times 10^{-15}$ level for $l = 3$ coefficients. These limits are more than an order of magnitude better than the previous best limit from a cavity experiment, and are comparable with a Compton scattering experiment.

Table 5.5: Summary of systematic uncertainties. Contribution ratios with respect to the statistical uncertainty are shown.

Cause	Amount	Ratio
Offset		
Sagnac effect	< 1 mrad/sec	$< 2\%$
Turntable tilt	< 0.2 mrad	$< 10\%$
Calibration		
Cavity detuning	-	3%
Openloop measurement	-	3%
Laser frequency actuation efficiency measurement	$A = 1.29 \pm 0.6$ MHz/V	5%
Silicon refractive index	$n = 3.69 \pm 0.01$	0.4%
Length	$L_{\rm opt} = 192 \pm 1$ mm	0.5%
Orientation		
Timing	< 1 min	$2 \times 10^{-5}\%$
Lab frame orientation	$< 10^\circ$	0.03%

- We have also done the analysis in the framework of the SME, and put the first limits on 13 camouflage coefficients $(\overline{c}_F^{(d)})_{jlm}^{(0E)}$ at $\sim 1 \times 10^3$ GeV^{-2} level for dimension $d = 6$, and $\sim 2 \times 10^{19}$ GeV^{-4} level for $d = 8$ coefficients. The sensitivity for $d = 6$ and $d = 8$ was improved by a factor of a million and 14 orders of magnitude, respectively, over existiting parity-even bounds.

- The estimated systematic offset was less than 10% of our statistical uncertainty, and the calibration uncertainty was 7%. The most contributing systematic uncertainty came from the tilt of the base of the turntable.

Chapter 6
Conclusion

In this chapter, we will summarize our work and make a discussion about our results. We will also give prospects for future parity-odd cavity tests of the Lorentz violation, and conclude our research.

6.1 Summary

We have developed an apparatus to test the Lorentz invariance in electrodynamics. The main component of the apparatus was an optical ring cavity, and we searched for the resonant frequency difference between counterpropagating directions. When there is any Lorentz violation, the constancy of the speed of light is violated. In particular, parity-odd components of the light speed anisotropy create the resonant frequency difference.

The propagation direction dependence of the speed of light $c(\theta, \phi)$ can be decomposed with the spherical harmonics $Y_l^m(\theta, \phi)$. The parity-odd anisotropies are l =odd components, which come from parity-odd Lorentz violation. We have introduced the spherical coefficients $\overline{y}_l^m$ to represent the size of the anisotropy for each mode.

The resonant frequency difference was measured with a double-pass configuration. The beam from the laser source was fed into the ring cavity in the counterclockwise direction and the laser frequency was locked to the counterclockwise resonant frequency. The transmitted beam from the ring cavity was reflected back into the cavity again, but in the clockwise direction. From its reflection, the error signal which is proportional to the resonant frequency difference was obtained. This double-pass configuration enabled a null measurement of the resonant frequency difference. Also, the differential measurement

enabled a rejection of the effects from the cavity length fluctuations, since they are common to both directions.

We took the Lorentz violation signal for more than a year starting from July 2012. During the observation run, the ring cavity was rotated in order to modulate the Lorentz violation signal. The data were taken for 393 days, and the ring cavity was rotated for approximately 1.7×10^6 times.

The data analysis was done with a demodulation method. First, the signal was demodulated at the harmonics of the turntable rotation frequency $m_{\rm r}\omega_{\rm rot}$ to get the modulation amplitudes for each rotation. One day data of these modulation amplitudes were then demodulated at the harmonics of the sidereal frequency $m_\oplus\omega_\oplus$ to get the sidereal modulation amplitudes. To do the data analysis up to $l = 3$, we restricted ourselves to $m_{\rm r} = 1, 3$ and $m_\oplus = 0, 1, 2, 3$.

From the modulation amplitudes we have extracted, we concluded that no significant evidence for the Lorentz violation was found at the $\delta c/c \lesssim 10^{-15}$ level. These modulation amplitudes are related to the spherical coefficients $\overline{y}_l^m$, and we put limits on $\overline{y}_l^m$ at $\sim 6 \times 10^{-15}$ level for $l = 1$, and at $\sim 2 \times 10^{-15}$ level for $l = 3$ coefficients. Our limits were more than an order of magnitude better than previous best cavity limits. Also, our experiment was the first experiment which could put limits on all the coefficients for $l = 1$ and $l = 3$.

In the framework of the Standard Model Extension, we have put the limits on 13 camouflage coefficients $(\overline{c}_F^{(d)})_{jlm}^{(0E)}$ at $\sim 1 \times 10^3$ GeV^{-2} level for dimension $d = 6$, and $\sim 2 \times 10^{19}$ GeV^{-4} level for $d = 8$ coefficients, for the first time. Over existing parity-even bounds from the microwave cavity experiment, the sensitivity was improved by a factor of a million for $d = 6$, and by 14 orders of magnitude for $d = 8$ coefficients. The improvement factors were large since the effect of the Lorentz violation scales with ν^{d-4}, and the optical frequency is higher than the microwave frequency.

6.2 Discussions

The previous best parity-odd cavity test was done by Baynes *et al.* [33], and they tested the isotropy of the speed of light at $\delta c/c \lesssim 2 \times 10^{-13}$ level. The sensitivity improvement over their experiment by a factor of ~ 30 is explained in part by a longer observation time and a higher refractive index of the dielec-

tric piece used. The observation time was a year instead of their 2 months. We used silicon with a refractive index of $n = 3.69$, whereas they used optical glass with $n = 1.44$. These two effects simply gave us factor of a ~ 6 improvement.

The unexplained factor of ~ 5 improvement could be from higher rotational speed and/or less noise from the use of the double-pass configuration. It is hard to compare with the Baynes experiment since we do not have their noise spectrum. The common mode rejection ratio (CMRR) from the differential measurement of the resonant frequencies for counterpropagating directions is also not measured yet at this point. The CMRR could be measured by modulating the cavity length with temperature, and measuring the feedback signal for the laser frequency servo and the Lorentz violation signal at the same time.

There are virtually no quantitative predictions for the light speed anisotropy, but we might expect the SME camouflage coefficients to involve some mass scale M. The simplest possibility is that the coefficients scale like M^{4-d} from dimensional analysis. If we assume that new physics beyond the Standard Model comes from the Planck-scale origin, it is natural to use the Planck mass ($M_{\rm pl} = 1.2 \times 10^{19}$ GeV) for M. However, it has been suggested that the coefficients might involve a lower energy scale, possibly in conjunction with the Planck scale. The lower energy scale could be electroweak scale $m_{\rm w} = 2.5 \times 10^2$ GeV, considering scenarios where the Lorentz breaking is connected to the Higgs mechanism.

Our new limits on the camouflage coefficients at 10^3 GeV^{-2} level for dimension $d = 6$ suggest M^2 to be larger than 10^{-3} GeV^2 level. Therefore, we can say that we put limit on the scale where the Lorentz violations arise at $M \gtrsim 0.03$ GeV. Although this energy scale is relatively low, this is the first limit from cavity experiments, to the best of our knowledge.

Also, there are theories where $d = 6$ violations might be quite large. For example, noncommutative geometry gives $d = 6$ violations at approximately 1 GeV^{-2}, considering noncommutative effects have a natural length scale of 10^{-15} m. This level is within the experimental reach, and we can also reach this level by increasing the sensitivity by 5 orders of magnitude in terms of $\delta c/c$. Also, using the laser with higher frequency, such as ultraviolet or X-ray, would simply increase the sensitivity to such higher order Lorentz violations.

6.3 Future prospects

The current noise level of our apparatus was dominated by the vibration of the turntable. This was because we used a simple commercial motor for the rotation, without any vibration isolation system. Most recent parity-even experiments [23, 24] have achieved sensitivities at the 10^{-17} level with a dedicated vibration isolation system. Also, the noise level of our apparatus when the turntable is not rotating was less by 2 orders of magnitude. These naively suggest the potential for a hundredfold improvement in future cavity tests of parity-odd Lorentz violation.

It is important to note that the estimated thermal noise level is more than 5 orders of magnitude below our current sensitivity. This means that we do not need to cool down the cavity to reduce thermal noise, until we reach the sensitivity at the 10^{-20} level. However, cryogenic operation might be needed in order to reduce thermal-optic coefficient of silicon. Effects from temperature dependence of the refractive index can also simply be reduced by introducing a temperature stabilization system.

Tilt fluctuations in a turntable rotational period would be an issue in future parity-odd tests. In our experiment, we did not apply any tilt control, and the tilt fluctuation stayed within 0.2 mrad. The estimated effect to the result was at the 10^{-16} level even in the pessimistic case. Thus, in order to test the Lorentz invariance at the 10^{-17} level, tilt fluctuation should be smaller than 2 μrad. This can be achieved by applying a similar tilt control system that has been used for parity-even experiments.

Vibrations and tilt fluctuations could be reduced by suspending the apparatus from the motor with flexible joint. An example of such a rotation system has been used for a modern Eötös experiment to test the weak equivalence principle with rotating torsion balance [58].

Also, fixing all the optics monolithically on a single optical bench would reduce the effects of vibration and tilt. This technique has been developed for space-based interferometric gravitational wave detector projects, such as LISA [59], DECIGO [60], and their pathfinders. These monolithic optical benches can be constructed using hydroxide-catalysis bonding of optical components to a baseplate made of materials with low thermal expansion [61].

Space-based test of Lorentz invariance could also be taken into reality, when monolithic optical benches are considered. Quiet environment in space and continuous smooth spin of a satellite would allow the sensitivity to reach into the 10^{-20} regime [62].

Continuous rotation can also be done in ground-based laboratories by using a slip ring to extract the signals from and provide power to the apparatus. There are mainly three advantages for continuous rotation. From the stability point of view, it will provide better rotational speed stability and longer duration of the laser frequency lock, since there will be no inversions of rotational directions. Also, duty cycle will be increased. In our setup, about 20% of the time was useless for the data analysis because of the dead time for inversions of rotations.

Finally, continuous rotation has a merit from the data analysis point of view. Since the cavity was rotated alternately, modulation amplitude extraction was done for each rotation. Demodulation will be more sensitive if we can use data containing multiple rotations. This is also a merit for noise hunting.

The reason why we did not use a slip ring to realize continuous rotation was because slip rings create the noise which is coherent to the rotation. This noise could be subtracted by monitoring the noise with a different cable from the cable for the Lorentz violation signal. This noise can also be fundamentally avoided by extracting the data with wireless signal transmission technique.

6.4 Conclusion

We have performed a search for the Lorentz violation in electrodynamics using an asymmetric optical ring cavity on a turntable. From the analysis of a year-long observational data, we put limits on dipole and hexapole components of anisotropy at the level of $\delta c/c \lesssim 10^{-15}$. Within the frame work of the Standard Model Extension, we have put the first limits on parity-odd higher order Lorentz violations. From this research, we have put the limit on the energy scale where new physics arises. Significant sensitivity improvement could be done in the future upgrade of the apparatus.

Appendix A
Standard Model Extension

The Standard Model Extension (SME) [13] is the theoretical framework to compare the precision of various experimental tests of Lorentz invariance and CPT symmetry. Here, we will briefly describe the SME coefficients that can be measured with our experiment. We will also show how to extract those coefficients from the data.

Note that here we only show the minimum set of definitions and equations that are used to analyze our data. For more comprehensive understanding of the SME in arbitrary dimension, see Refs. [16, 63].

A.1 Overview of the SME electrodynamics

In this section, we will introduce the photonic Lagrangian density in the framework of the SME, and describe the coefficients that can be measured with cavity experiments. By adding the Lorentz violating terms in the Lagrangian density, the light speed dependence on polarization, wavelength, and propagation direction are introduced. Each of the effects are connected to different types of the SME coefficients and they are called the birefringence coefficients, the dispersion coefficients, and the camouflage coefficients, respectively.

The cavity experiments are sensitive to the camouflage coefficients, which describe the anisotropy of the speed of light. We will also show the current limits on the camouflage coefficients, as well as the birefringence and dispersion coefficients.

A.1.1 Camouflage coefficients

The general Lagrangian density in the framework of the SME for photons can be written as [16]

$$\mathcal{L}_{\text{photon}} = -\frac{1}{4}F_{\mu\nu}F^{\mu\nu} + \frac{1}{2}\epsilon^{\kappa\lambda\mu\nu}A_\lambda(\hat{k}_{AF})_\kappa F_{\mu\nu} - \frac{1}{4}F_{\kappa\lambda}(\hat{k}_F)^{\kappa\lambda\mu\nu}F_{\mu\nu}, \tag{A.1}$$

where A_κ is the electromagnetic four-potential, and $F_{\mu\nu}$ is the electromagnetic tensor defined by $F_{\mu\nu} \equiv \partial_\mu A_\nu - \partial_\nu A_\mu$. The differential operators $\hat{k}_{AF}$ and $\hat{k}_F$ can be expanded with the mass dimension of the tensor operator d as

$$(\hat{k}_{AF})_\kappa = \sum_{d=\text{odd}} (k_{AF}^{(d)})_\kappa, \tag{A.2}$$

$$(\hat{k}_F)^{\kappa\lambda\mu\nu} = \sum_{d=\text{even}} (k_F^{(d)})^{\kappa\lambda\mu\nu}, \tag{A.3}$$

where the sums range over values $d \geq 3$.

The terms with $d =$ odd violates the CPT symmetry as well as Lorentz invariance. So, here we restrict ourselves only to $\hat{k}_F$ terms, which involve *CPT*-even violations. Also, by neglecting the leading order birefringent terms, the Lagrangian density reduces to

$$\mathcal{L}_{\text{photon}} = -\frac{1}{4}F_{\mu\nu}F^{\mu\nu} - \frac{1}{2}F_{\kappa\rho}(\hat{c}_F)^{\mu\nu}F^\rho_\nu. \tag{A.4}$$

Here, $(\hat{c}_F)^{\mu\nu}$ is the derivative of the scalar potential $\hat{\Phi}_F$

$$(\hat{c}_F)^{\mu\nu} = \partial^\mu\partial^\nu\hat{\Phi}_F, \tag{A.5}$$

and the relationship between $\hat{c}_F$ and $\hat{k}_F$ is shown in Ref. [16].

It is safe to neglect some operators result in vacuum birefringence here, since there are tight constraints on birefringent coefficients. Constraints were obtained from polarization measurements of light from cosmologically distant sources, such as gamma ray bursts [16, 64].

By expanding the scalar potential $\hat{\Phi}_F$ in spherical harmonics,

$$\hat{\Phi}_F = \sum_{djlm} \omega^{d-2-j} p^j{}_0 Y_l^m(\hat{\boldsymbol{p}})(c_F^{(d)})_{jlm}^{(0E)}, \tag{A.6}$$

we get the minimal set $(c_F^{(d)})_{jlm}^{(0E)}$ of nonbirefringent spherical coefficients for Lorentz violation. Here, ω and $\boldsymbol{p} = p\hat{\boldsymbol{p}}$ are the angular frequency and the three-momentum of photons.

The last step is to consider dispersive effects. We can also set the dispersion coefficients to be zero since there are tight constraints from dispersion measurement of light from gamma ray bursts [65]. No vacuum dispersion is ensured if $\hat{\Phi}_F$ can be written in the form $\hat{\Phi}_F = p^2\tilde{\Phi}_F$. We can define the set of coefficients

$$\tilde{\Phi}_F = \sum_{djlm} \omega^{d-4-j} p^j {}_0Y_l^m(\hat{\boldsymbol{p}})(\overline{c}_F^{(d)})_{jlm}^{(0E)}. \tag{A.7}$$

This result leads to the simple relation

$$(c_F^{(d)})_{jlm}^{(0E)} = (\overline{c}_F^{(d)})_{jlm}^{(0E)} - (\overline{c}_F^{(d)})_{(j-2)lm}^{(0E)} \tag{A.8}$$

when there is no leading order birefringence or vacuum dispersion.

Thus, the set of $(\overline{c}_F^{(d)})_{jlm}^{(0E)}$ is the anisotropy coefficients in the SME, and they are called the camouflage coefficients. For each even dimension $d \geq 6$, there are $(d-1)(d-2)(d-3)/6$ independent components, including $(d-2)(d-4)(2d-3)/24$ parity-odd components. Dimensional analysis shows that the dimension of the camouflage coefficients is $4-d$. By convention, measurements of coefficients are reported in units of GeV^{4-d}.

A.1.2 Current limits

Current constraints on the birefringence coefficients for $d = 6$ are at 10^{-32} to 10^{-31} GeV^{-2} level, and for $d = 6$ are at 10^{-25} to 10^{-24} GeV^{-4} level [64]. Constraints on vacuum dispersion coefficients for $d = 6$ are at 10^{-21} to 10^{-19} GeV^{-2} level [65], and for $d = 8$ are at 10^{-25} GeV^{-4} level [65]. These limits are obtained from astrophysical observations of the light from gamma ray bursts.

Constraints on the camouflage coefficients are obtained by cavity experiments. The first constraints are reported by Parker *et al.* [66] using the data described in [67]. They used rotating microwave sapphire resonators that are orthogonally aligned inside the cryostat. By using the data taken for 14 months, they put limits on the even-parity components of the anisotropy to the $|\delta c/c| \lesssim 10^{-16}$ level. Their constraints on the camouflage coefficients for

Table A.1: Summary of current limits on SME camouflage coefficients.

dimension		Parker *et al.* [66]	This work
$d = 6$	dipole	no access	first limit
	quadrupole	10^{8} to 10^{11} GeV^{-2}	no access
$d = 8$	dipole	no access	first limit
	quadrupole	10^{36} to 10^{38} GeV^{-4}	no access
	hexapole	no access	first limit
	octupole	10^{33} to 10^{34} GeV^{-4}	no access

$d = 4$ were at 10^{-14} to 10^{-17} level, for $d = 6$ were at 10^{8} to 10^{11} GeV^{-2} level, and for $d = 8$ were at 10^{33} to 10^{38} GeV^{-4} level.

As implied by Eq. (A.7), the effects of Lorentz violation typically grow with frequency by a factor of ω^{d-4}. This gives optical cavities an inherent advantage over microwave cavities. We naively expect an increase in sensitivity by a factor of $\sim 10^{4(d-4)}$ compared with Ref. [66]. The frequency of the laser we used is 200 THz and their frequency was 10 GHz.

Table A.1 summarizes current limits on SME camouflage coefficients, and which coefficients we can explore with our apparatus. We search for dipole and hexapole anisotropy components to measure parity-odd camouflage coefficients for the first time.

We note here that limit on vacuum dispersion from gamma ray bursts are also put within the framework other than the SME. For example, the Fermi LAT (Large Area Telescope) Collaboration put limit on vacuum dispersion arising from quantum gravity effects [68].

A.2 Data analysis in the SME

In this section, we will show the expression of our Lorentz violation signal in the framework of the SME. Then, we show the relationship between the modulation amplitudes described in Section 5.1.3 and the SME camouflage coefficients $(\overline{c}_F^{(d)})_{jlm}^{(0E)}$. The detailed calculation is described in Ref. [63].

A.2.1 Expression of the Lorentz violation signal

The resonant frequency difference between the counterclockwise and clockwise directions due to the SME camouflage terms takes the form [63]

$$\frac{\delta\nu}{\nu} = \sum_{djlm_{\rm r}m_\oplus} A_{m_{\rm r}m_\oplus} e^{im_{\rm r}\omega_{\rm rot}t + im_\oplus\omega_\oplus T_\oplus} \tag{A.9}$$

where

$$A_{m_{\rm r}m_\oplus} = \Delta\mathcal{M}^{(d)\ \rm lab}_{(\overline{c}_F)_{jlm_{\rm r}}} d^{(l)}_{m_{\rm r}m_\oplus}(-\chi)(\overline{c}^{(d)}_F)^{(0E)}_{jlm_\oplus}. \tag{A.10}$$

Here, $\Delta\mathcal{M}^{(d)\ \rm lab}_{(\overline{c}_F)_{jlm}}$ is the $\mathcal{M}^{(d)\ \rm lab}_{(\overline{c}_F)_{jlm}}$ matrix difference between the counterclockwise and clockwise directions, and the $\mathcal{M}^{(d)\ \rm lab}_{(\overline{c}_F)_{jlm}}$ matrices are experiment dependent factors that determine the sensitivity of the cavity to the camouflage coefficients. χ is the colatitude of the laboratory, and the $d^{(l)}_{m_{\rm r}m_\oplus}$ are little Wigner matrices defined by

$$\begin{aligned} d^{(l)}_{m_{\rm r}m_\oplus}(\beta) \;=\; & \sum_k \frac{(-1)^{m_{\rm r}-m_\oplus+k}\sqrt{(l+m_{\rm r})!(l-m_{\rm r})!(l+m_\oplus)!(l-m_\oplus)!}}{(l-m_{\rm r}-k)!(m_{\rm r}-m_\oplus+k)!(l+m_\oplus-k)!k!} \\ & \cdot\left(\cos\frac{\beta}{2}\right)^{2l-m_{\rm r}+m_\oplus-2k}\left(\sin\frac{\beta}{2}\right)^{m_{\rm r}-m_\oplus+2k}, \end{aligned} \tag{A.11}$$

where sum over k is over such values that the factorials are nonnegative, i.e. $\max(m_\oplus - m_{\rm r}, 0) \le k \le \min(l-m_{\rm r}, l+m_\oplus)$. Also, when $|m_{\rm r}| > l$ or $|m_\oplus| > l$, $d^{(l)}_{m_{\rm r}m_\oplus}(\beta) = 0$.

We first consider $\mathcal{M}^{(d)\ \rm lab}_{(c_F)_{jlm}}$ matrix with dispersion coefficients to get the $\mathcal{M}^{(d)\ \rm lab}_{(\overline{c}_F)_{jlm}}$ matrix. From Eq. (A.8), they are related with

$$\mathcal{M}^{(d)\ \rm lab}_{(\overline{c}_F)_{jlm}} = \mathcal{M}^{(d)\ \rm lab}_{(c_F)_{jlm}} - \mathcal{M}^{(d)\ \rm lab}_{(c_F)_{(l+2)lm}}. \tag{A.12}$$

We need the $\mathcal{M}^{(d)\ \rm lab}_{(c_F)_{jlm}}$ matrix elements for each arm of the cavity to get the

$\mathcal{M}^{(d)\ \mathrm{lab}}_{(c_F)_{jlm}}$ matrix. They depend on the arm frame factors

$$\mathcal{U}^{(d)}_{jl} = -\frac{\omega^{d-4}n^{j-2}}{2\epsilon}\sqrt{\frac{2l+1}{4\pi}}\left[\left(j-\frac{l(l+1)}{2}\right)(n^2-1)\right. \\ \left.+(d-2-j)(d-3-3j)n^2+j(j-1)n^2\right] \tag{A.13}$$

$$\mathcal{V}^{(d)}_{jl} = \frac{\omega^{d-4}n^{j-2}(n^2-1)}{8\epsilon}\sqrt{\frac{2l+1}{4\pi}\frac{(l+2)!}{(l-2)!}} \tag{A.14}$$

Here, ϵ and n are the permittivity and the refractive index of the arm, respectively. Since we are not using magnetic elements, here we can set $\epsilon = n^2$. The $\mathcal{M}^{(d)}_{(c_F)_{jlm}}$ matrix for the arm in the arm frame is given by

$$\mathcal{M}^{(d)\ \mathrm{arm}}_{(c_F)_{jlm}} = \mathcal{U}^{(d)}_{jl}\delta_{m,0} + \mathcal{V}^{(d)}_{jl}\delta_{|m|,2} \tag{A.15}$$

By rotating this to the laboratory frame (see Fig. 5.3) using Wigner matrices, we get

$$\mathcal{M}^{(d)\ \mathrm{lab}}_{(c_F)_{jlm}} = \sum_{m'}\mathcal{M}^{(d)\ \mathrm{lab}}_{(c_F)_{jlm'}}e^{im'\gamma}e^{im\alpha}d^{(l)}_{m'm}\left(-\frac{\pi}{2}\right) \tag{A.16}$$

$$= \left[\mathcal{U}^{(d)}_{jl}d^{(l)}_{0m}\left(-\frac{\pi}{2}\right)+\mathcal{V}^{(d)}_{jl}e^{i2\gamma}d^{(l)}_{2m}\left(-\frac{\pi}{2}\right)\right. \\ \left.+\mathcal{V}^{(d)}_{jl}e^{-i2\gamma}d^{(l)}_{(-2)m}\left(-\frac{\pi}{2}\right)\right]e^{im\alpha}. \tag{A.17}$$

Here, $\pi/2$ rotates the beam into the horizontal plane, α is the angle between the beam and the laboratory x-axis at $t = 0$, and γ is the angle between the polarization and the horizontal plane.

Since p-polarized light resonates in the cavity in our setup, $\gamma = 0$. α for each arm in the counterclockwise mode is

$$\alpha = \begin{cases} -\xi+\zeta & \text{for the arm A} \\ 0 & \text{for the arm B} \\ -\xi-\zeta-\pi & \text{for the arm C} \\ -\xi-\pi/2 & \text{for the arm D} \end{cases}$$

The label of each arm are the same as the one defined in Fig. 5.3. Also, the index of refraction $n = 1$ for all the arms except for B. Note that $\mathcal{V}_{jl}^{(d)} = 0$ when $n = 1$, so it only contributes to the arm B. From these values, we can calculate $\mathcal{M}_{(c_F)_{jlm}}^{(d)\ \mathrm{lab}}$ for each arm.

Next, we combine the results for the individual arms to get the $\mathcal{M}_{(c_F)_{jlm}}^{(d)\ \mathrm{lab}}$ matrix for the counterclockwise mode,

$$\begin{aligned}\mathcal{M}_{(c_F)_{jlm}}^{(d)\ \mathrm{lab}} &= \frac{L_\mathrm{A}}{L_\mathrm{opt}}\mathcal{M}_{(c_F)_{jlm}}^{(d)\ \mathrm{A}} + \frac{nL_\mathrm{B}}{L_\mathrm{opt}}\mathcal{M}_{(c_F)_{jlm}}^{(d)\ \mathrm{B}} \\ &\quad + \frac{L_\mathrm{C}}{L_\mathrm{opt}}\mathcal{M}_{(c_F)_{jlm}}^{(d)\ \mathrm{C}} + \frac{L_\mathrm{D}}{L_\mathrm{opt}}\mathcal{M}_{(c_F)_{jlm}}^{(d)\ \mathrm{D}},\end{aligned} \tag{A.18}$$

which is the optical path length weighted average ($L_\mathrm{opt} \equiv L_\mathrm{A} + nL_\mathrm{B} + L_\mathrm{C} + L_\mathrm{D}$). Comparison of this equation with Eq. (5.20) gives the rough relation between δc and $\mathcal{M}_{(c_F)_{jlm}}^{(d)\ \mathrm{lab}}$.

The $\mathcal{M}_{(c_F)_{jlm}}^{(d)\ \mathrm{lab}}$ matrix for the clockwise mode is found to be reversing the direction of the beam in each arm. This is equivalent to adding π to each α angle, and this gives an extra factor of $e^{im\pi} = (-1)^m$. So, the difference between the counterclockwise mode and clockwise mode is given by

$$\Delta\mathcal{M}_{(c_F)_{jlm}}^{(d)\ \mathrm{lab}} = \left(1 - (-1)^m\right)\mathcal{M}_{(c_F)_{jlm}}^{(d)\ \mathrm{lab}}. \tag{A.19}$$

A.2.2 Extraction of the camouflage coefficients from the signal

The relationship between the camouflage coefficients $(\overline{c}_F^{(d)})_{jlm}^{(0E)}$ and the modulation amplitudes defined in Eq. (5.22), Eq. (5.23) and Eq. (5.24) can be derived by comparing these equations with Eq. (A.9). The modulation amplitudes are given by

$$C_{m_\mathrm{r}m_\oplus}^{C} = 2\eta_{m_\mathrm{r}}\eta_{m_\oplus}\mathrm{Re}[A_{m_\mathrm{r}m_\oplus} + A_{m_\mathrm{r}(-m_\oplus)}], \tag{A.20}$$

$$C_{m_\mathrm{r}m_\oplus}^{S} = -2\eta_{m_\mathrm{r}}\mathrm{Im}[A_{m_\mathrm{r}m_\oplus} - A_{m_\mathrm{r}(-m_\oplus)}], \tag{A.21}$$

$$S_{m_\mathrm{r}m_\oplus}^{C} = -2\eta_{m_\oplus}\mathrm{Im}[A_{m_\mathrm{r}m_\oplus} + A_{m_\mathrm{r}(-m_\oplus)}], \tag{A.22}$$

$$S_{m_\mathrm{r}m_\oplus}^{S} = -2\mathrm{Re}[A_{m_\mathrm{r}m_\oplus} - A_{m_\mathrm{r}(-m_\oplus)}], \tag{A.23}$$

where $\eta_0 = 1/2$, and $\eta_m = 1$ when $m \neq 0$.

In this thesis, we restricted ourselves to extract modulation amplitudes for m_r and $m_\oplus$ up to 3. Since the camouflage coefficients for $d = 6$ introduce monopole, dipole and quadrupole structures of the anisotropy, while $d = 8$ also give hexapole and octupole structures, we can restrict ourselves to consider up to $d = 8$ coefficients. Our experiment is only sensitive to parity-odd dipole and hexapole anisotropies.

The relationship between the camouflage coefficients of $d = 6$ and $d = 8$ and the modulation amplitudes for our optical ring cavity is summarized in Table A.2. Comparison of this table with Table 5.1 gives naive picture of the multipole structure of the SME camouflage coefficients. As predicted by the multipole structure, only $m_\oplus = 0, 1$ contribute for $d = 6$ and $m_\oplus = 0, 1, 2, 3$ contribute for $d = 8$.

Table A.2: Nonzero modulation amplitudes for dimensions 6 and 8 The numbers $m_{\rm r}$ and $m_\oplus$ represent the harmonics of the turntable rotation frequency and sidereal frequency. The dimension-6 amplitudes are in units of 10^{-18} GeV^2. The dimension-8 amplitudes are in units of 10^{-36} GeV^4. $\mathcal{C}_{m_\oplus} = -0.020(\overline{c}_F^{(8)})^{(0E)}_{11m_\oplus} + (\overline{c}_F^{(8)})^{(0E)}_{31m_\oplus}$.

Dimension	$m_{\rm r}$	$m_\oplus$	$C^C_{m_{\rm r}m_\oplus}$	$C^S_{m_{\rm r}m_\oplus}$	$S^C_{m_{\rm r}m_\oplus}$	$S^S_{m_{\rm r}m_\oplus}$
$d=6$	1	0	$-0.66(\overline{c}_F^{(6)})^{(0E)}_{110}$	-	0	-
	1	1	$-0.68\mathrm{Re}[(\overline{c}_F^{(6)})^{(0E)}_{111}]$	$0.68\mathrm{Im}[(\overline{c}_F^{(6)})^{(0E)}_{111}]$	$1.2\mathrm{Im}[(\overline{c}_F^{(6)})^{(0E)}_{111}]$	$1.2\mathrm{Re}[(\overline{c}_F^{(6)})^{(0E)}_{111}]$
$d=8$	1	0	$-44\mathcal{C}_0 + 18(\overline{c}_F^{(8)})^{(0E)}_{330}$	-	0	-
	1	1	$-44\mathrm{Re}(\mathcal{C}_1)$	$44\mathrm{Im}(\mathcal{C}_1)$	$76\mathrm{Im}(\mathcal{C}_1)$	$76\mathrm{Re}(\mathcal{C}_1)$
			$-61\mathrm{Re}[(\overline{c}_F^{(8)})^{(0E)}_{331}]$	$+61\mathrm{Im}[(\overline{c}_F^{(8)})^{(0E)}_{331}]$	$-12\mathrm{Im}[(\overline{c}_F^{(8)})^{(0E)}_{331}]$	$-12\mathrm{Re}[(\overline{c}_F^{(8)})^{(0E)}_{331}]$
	1	2	$-0.98\mathrm{Re}[(\overline{c}_F^{(8)})^{(0E)}_{332}]$	$0.98\mathrm{Im}[(\overline{c}_F^{(8)})^{(0E)}_{332}]$	$53\mathrm{Im}[(\overline{c}_F^{(8)})^{(0E)}_{332}]$	$53\mathrm{Re}[(\overline{c}_F^{(8)})^{(0E)}_{332}]$
	1	3	$26\mathrm{Re}[(\overline{c}_F^{(8)})^{(0E)}_{333}]$	$-26\mathrm{Im}[(\overline{c}_F^{(8)})^{(0E)}_{333}]$	$-45\mathrm{Im}[(\overline{c}_F^{(8)})^{(0E)}_{332}]$	$-45\mathrm{Re}[(\overline{c}_F^{(8)})^{(0E)}_{333}]$
	3	0	$-14(\overline{c}_F^{(8)})^{(0E)}_{330}$	-	$0.58(\overline{c}_F^{(8)})^{(0E)}_{330}$	-
	3	1	$1.2\mathrm{Im}[(\overline{c}_F^{(8)})^{(0E)}_{331}]$	$17\mathrm{Im}[(\overline{c}_F^{(8)})^{(0E)}_{331}]$	$30\mathrm{Im}[(\overline{c}_F^{(8)})^{(0E)}_{331}]$	$-0.72\mathrm{Im}[(\overline{c}_F^{(8)})^{(0E)}_{331}]$
			$-17\mathrm{Re}[(\overline{c}_F^{(8)})^{(0E)}_{331}]$	$+1.2\mathrm{Re}[(\overline{c}_F^{(8)})^{(0E)}_{331}]$	$+0.72\mathrm{Re}[(\overline{c}_F^{(8)})^{(0E)}_{331}]$	$+30\mathrm{Re}[(\overline{c}_F^{(8)})^{(0E)}_{331}]$
	3	2	$1.1\mathrm{Im}[(\overline{c}_F^{(8)})^{(0E)}_{332}]$	$31\mathrm{Im}[(\overline{c}_F^{(8)})^{(0E)}_{332}]$	$27\mathrm{Im}[(\overline{c}_F^{(8)})^{(0E)}_{332}]$	$-1.3\mathrm{Im}[(\overline{c}_F^{(8)})^{(0E)}_{332}]$
			$-31\mathrm{Re}[(\overline{c}_F^{(8)})^{(0E)}_{332}]$	$+1.1\mathrm{Re}[(\overline{c}_F^{(8)})^{(0E)}_{332}]$	$+1.3\mathrm{Re}[(\overline{c}_F^{(8)})^{(0E)}_{332}]$	$+27\mathrm{Re}[(\overline{c}_F^{(8)})^{(0E)}_{332}]$
	3	3	$1.0\mathrm{Im}[(\overline{c}_F^{(8)})^{(0E)}_{333}]$	$23\mathrm{Im}[(\overline{c}_F^{(8)})^{(0E)}_{333}]$	$24\mathrm{Im}[(\overline{c}_F^{(8)})^{(0E)}_{333}]$	$-0.94\mathrm{Im}[(\overline{c}_F^{(8)})^{(0E)}_{333}]$
			$-23\mathrm{Re}[(\overline{c}_F^{(8)})^{(0E)}_{333}]$	$+1.0\mathrm{Re}[(\overline{c}_F^{(8)})^{(0E)}_{333}]$	$+0.94\mathrm{Re}[(\overline{c}_F^{(8)})^{(0E)}_{333}]$	$+24\mathrm{Re}[(\overline{c}_F^{(8)})^{(0E)}_{333}]$

Appendix B
Feedback Control

Here we briefly summarize the basics of the feedback control needed for reading this thesis. For more comprehensive understanding, see, for example, Ref. [69].

B.1 Openloop transfer function

In a feedback control, we measure fluctuation of the output of the system and try to regulate the output by applying a force in an opposite direction to the system input. Typical feedback control loop in a block diagram is shown in Fig. B.1. First, some external disturbance x_0 is converted into an error signal $v_{\rm er}$ with a sensor transfer function H. From this error signal, the amount of feedback $v_{\rm fb}$ is determined with a servo filter F, and an actuator A puts the feedback into the input of the sensor. By this feedback, original fluctuation x_0 is regulated to $x_{\rm st}$.

Here, the residual fluctuation $x_{\rm st}$ can be written with transfer functions of the sensor, the filter, and the actuator as

$$x_{\rm st} = x_0 - AFHx_{\rm st}. \tag{B.1}$$

Thus, by defining $G \equiv AFH$,

$$x_{\rm st} = \frac{1}{1+G}x_0 \tag{B.2}$$

follows. As you can see from this equation, the fluctuation can be reduced by making the gain $|G|$ high. This G is called the openloop transfer function.

However, G is generally a function of Fourier frequency, and it is not possi-

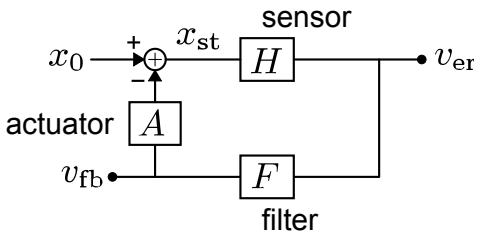

Figure B.1: Block diagram showing principle of a typical feedback control.

ble to make $|G|$ high at all the frequency bands. Generally, $|G|$ is low at higher frequency, and the frequency band which is $|G| > 1$ is called a control band. The frequency where $|G| = 1$ is called a unity gain frequency (UGF).

As you can guess from Eq. (B.2) that $x_{\rm st}$ diverges when $G = -1$, UGF is important for determining the stability of a servo. There is a number of ways for the determination, but the Nyquist stability criterion is often used for the determination of the stability of the system with relatively simple transfer functions. If the phase margin of G, such as $\arg(G) + 180^\circ$ is larger than $\sim 30^\circ$, we can say that feedback control is stable.

A real part and an imaginary part of a transfer function has the Kramers-Kronig relation, and it is not possible to manage both a high gain and a large phase margin. We have to design a transfer function of a servo filer circuit F, so that a high gain is achieved at the frequency band we need, and also realize a stable feedback control loop.

B.2 Feedback control and noise

In ideal cases we considered in the previous section, making loop gain G high sufficiently suppresses the fluctuation. However, in real cases, contamination of noises in the servo loop limits the achievable residual fluctuation.

In this section, we consider about the sensor noise $n_{\rm S}$ and the noise from the filter circuit $n_{\rm F}$ as shown in Fig. B.2. We discuss about how to estimate the residual fluctuation in the presence of noises, and about how to estimate the original external disturbances.

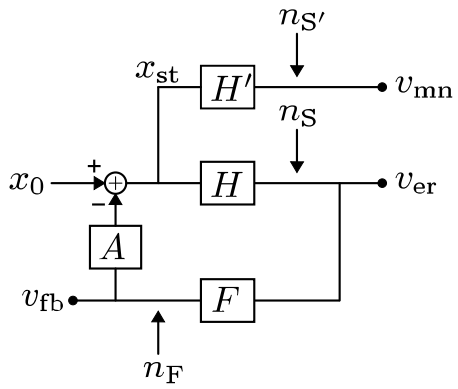

Figure B.2: Block diagram of a feedback control with noise injections and a monitor signal.

B.2.1 In-loop and out-of-loop

Feedback control loop try to control the error signal to be 0, but since the error signal includes sensor noises, the error signal in the servo loop (in-loop error signal) does not tell you the actual residual fluctuation.

For example, the error signal in the feedback system in Fig. B.2 is

$$v_{\rm er} = H[x_0 - A(Fv_{\rm er} + n_{\rm F})] + n_{\rm S}, \tag{B.3}$$

so,

$$v_{\rm er} = \frac{H}{1+G}x_0 - \frac{HA}{1+G}n_{\rm F} + \frac{1}{1+G}n_{\rm S}. \tag{B.4}$$

Thus, the estimated residual fluctuation from the error signal is

$$x_{\rm st}^{\rm (er)} = \frac{v_{\rm er}}{H} = \frac{1}{1+G}x_0 - \frac{A}{1+G}n_{\rm F} + \frac{1}{1+G}\frac{1}{H}n_{\rm S}. \tag{B.5}$$

When $|G| \gg 1$, $x_{\rm st}^{\rm (er)} \sim 0$.

However, actually,

$$x_{\rm st} = \frac{v_{\rm er} - n_{\rm S}}{H} = \frac{1}{1+G}x_0 - \frac{A}{1+G}n_{\rm F} - \frac{G}{1+G}\frac{1}{H}n_{\rm S}, \tag{B.6}$$

and even if $|G| \gg 1$, $x_{\rm st} \sim n_{\rm S}/H$ and not $x_{\rm st} \sim 0$. Therefore, by using the

in-loop error signal alone, we underestimate the residual fluctuation.

In order to estimate the residual fluctuation, we need the monitor signal $v_{\rm mn}$ which is out-of-loop, as shown in Fig. B.2. $v_{\rm mn}$ can be written as

$$v_{\rm mn} = H' x_{\rm st} + n_{\rm S'}, \tag{B.7}$$

and the estimated residual fluctuation from this monitor signal is

$$x_{\rm st}^{\rm (mn)} = \frac{v_{\rm mn}}{H'} = \frac{1}{1+G}x_0 - \frac{A}{1+G}n_{\rm F} - \frac{G}{1+G}\frac{1}{H}n_{\rm S} + \frac{1}{H'}n_{\rm S'}. \tag{B.8}$$

When $|G| \gg 1$, $x_{\rm st}^{\rm (mn)} \sim n_{\rm S}/H + n_{\rm S'}/H'$ and it will be a better estimation of the residual fluctuation.

B.2.2 Estimating external disturbance

Feedback control is also used when the sensor only has a high sensitivity at limited range. By regulating the fluctuation, we can operate the sensor with a high sensitivity and a linear response. The estimation of the external disturbance can be done by using the feedback signal which the control loop added in order to suppress the fluctuation.

The feedback signal $v_{\rm fb}$ can be calculated by the similar control loop calculation we have done above, and it is

$$v_{\rm fb} = \frac{FH}{1+G}x_0 + \frac{F}{1+G}n_{\rm S} + \frac{1}{1+G}n_{\rm F}. \tag{B.9}$$

Thus, the estimated external disturbance is

$$x_0^{\rm (fb)} = \frac{1+G}{FH}v_{\rm fb} = x_0 + \frac{1}{H}n_{\rm S} + \frac{A}{G}n_{\rm F}. \tag{B.10}$$

Estimation of the external disturbance from the feedback signal is good especially where the frequency region with $|G| > 1$, since the effect of $n_{\rm F}$ is small. Outside the control band, however, $n_{\rm F}$ term become large and the estimation is not so accurate.

So, outside the control band, it is better to use the error signal for estimating the external disturbance. From Eq. (B.4), the external disturbance

estimated from the error signal is

$$x_0^{(\mathrm{er})} = \frac{1+G}{H} v_{\mathrm{er}} = x_0 + \frac{1}{H} n_{\mathrm{S}} + A n_{\mathrm{F}}. \tag{B.11}$$

Appendix C
Optical Cavities and Hansch-Couillaud Method

We used the Hänsch-Couillaud (HC) method [70, 71] for extracting the error signal for locking the laser frequency to the cavity resonant frequency. Here, we briefly discuss about properties of optical cavities. Then, we explain the mechanism of waveplates which changes the polarization state of the beam, and show the principle of the HC method. Lastly, we discuss about advantages of the use of the HC method in our experiment.

C.1 Optical cavities

Optical cavities are made from multiple mirrors that are put against each other, so that the beam circulates inside many times. Especially, a cavity which consist from two parallel mirrors is called a Fabry-Perot cavity, and a cavity which consist from more than three mirrors is called a ring cavity. In a Fabry-Perot cavity, standing waves are formed inside the cavity, and in a ring cavity, travelling waves are formed.

Optical cavities has resonant frequencies, and only the beam with those laser frequencies resonates inside the cavity. Here, we summarize about this feature.

C.1.1 Reflectivity and transmissivity

Consider an optical cavity which consist from three mirrors M1, M2, and M3, as shown in Fig. C.1. The round-trip length of this cavity is L, and

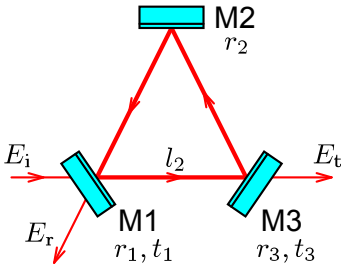

Figure C.1: Three mirror optical cavity.

amplitude reflectivities and amplitude transmissivities of each mirror are r_i and t_i, respectively.

If we set the electrical field amplitude of the incident laser beam to M1 to be E_i, the amplitude of the reflected light can be calculated by considering the propagation of the beam as

$$\begin{aligned} E_\mathrm{r} &= E_\mathrm{i}(-r_1) + E_\mathrm{i}t_1^2 r_3 r_2 e^{-i\phi} + E_\mathrm{i}t_1^2 r_3^2 r_2^2 r_1 e^{-2i\phi} + E_\mathrm{i}t_1^2 r_3^3 r_2^3 r_1^2 e^{-3i\phi} + \cdots \\ &= E_\mathrm{i}(-r_1) + E_\mathrm{i}t_1^2 r_3 r_2 e^{-i\phi} \sum_{n=0}^{\infty} \left(r_3 r_2 r_1 e^{-i\phi}\right)^n \\ &= E_\mathrm{i}\left(-r_1 + \frac{t_1^2 r_2 r_3 e^{-i\phi}}{1 - r_1 r_2 r_3 e^{-i\phi}}\right). \end{aligned} \tag{C.1}$$

Here, ϕ is the phase change accumulated when the beam makes a round-trip inside the cavity. Using the angular frequency of the laser beam, ϕ can be written as

$$\phi \equiv \frac{L\omega}{c}. \tag{C.2}$$

Similarly, the amplitude of the transmitted beam from M3 can be calculated as

$$\begin{aligned} E_\mathrm{t} &= E_\mathrm{i}t_1 t_3 e^{-i\phi_2} + E_\mathrm{i}t_1 r_3 r_2 r_1 t_3 e^{-i(\phi+\phi_2)} + E_\mathrm{i}t_1 (r_3 r_2 r_1)^2 t_3 e^{-i(2\phi+\phi_2)} + \cdots \\ &= E_\mathrm{i}t_1 t_3 e^{-i\phi_2} \sum_{n=0}^{\infty} \left(r_3 r_2 r_1 e^{-i\phi}\right)^n \\ &= E_\mathrm{i}\frac{t_1 t_3 e^{-i\phi_2}}{1 - r_1 r_2 r_3 e^{-i\phi}}. \end{aligned} \tag{C.3}$$

Here, $\phi_2 \equiv l_2\omega/c$ is the phase change of the beam accumulated between M1 and M3.

Thus, the amplitude reflectivity $r_{\rm cav}$ and the amplitude transmissivity $t_{\rm cav}$ of this ring cavity are

$$r_{\rm cav}(\phi) = -r_1 + \frac{t_1^2 r_2 r_3 e^{-i\phi}}{1 - r_1 r_2 r_3 e^{-i\phi}}, \tag{C.4}$$

$$t_{\rm cav}(\phi) = \frac{t_1 t_3 e^{-i\phi_2}}{1 - r_1 r_2 r_3 e^{-i\phi}}. \tag{C.5}$$

Now, from Eq. (C.1) and Eq. (C.3), intensities of the reflected light and transmitted light are

$$\begin{aligned} P_{\rm r} &= |E_{\rm r}|^2 \\ &= \frac{(r_2 r_3 - r_1)^2 + 4 r_1 r_2 r_3 \sin^2(\phi/2)}{(1 - r_1 r_2 r_3)^2 + 4 r_1 r_2 r_3 \sin^2(\phi/2)} |E_{\rm i}|^2, \end{aligned} \tag{C.6}$$

$$\begin{aligned} P_{\rm t} &= |E_{\rm t}|^2 \\ &= \frac{(t_1 t_3)^2}{(1 - r_1 r_2 r_3)^2 + 4 r_1 r_2 r_3 \sin^2(\phi/2)} |E_{\rm i}|^2. \end{aligned} \tag{C.7}$$

Here, we assumed $r_1^2 + t_1^2 = 1$.

When the intensity of the transmitted light is at the maximum, the intensity of the beam inside the cavity (intra-cavity power) is at the maximum, and we say that the incident laser beam resonates in the cavity. The resonance condition is

$$\phi = 2\pi m, \tag{C.8}$$

where m is a natural number. Therefore, from Eq. (C.2), the resonant frequencies of this cavity are

$$\nu = \frac{mc}{L}. \tag{C.9}$$

Fig. C.2 shows absolute value and phase of an amplitude reflectivity of an optical cavity near resonance. As we can clearly see from this plot, small change in ϕ drastically change the phase of the reflected light. This is because the change in ϕ is amplified when the beam circulates inside the cavity many times. Because of this feature, we can use optical cavities as interferometers to measure the frequency of the incident beam ν.

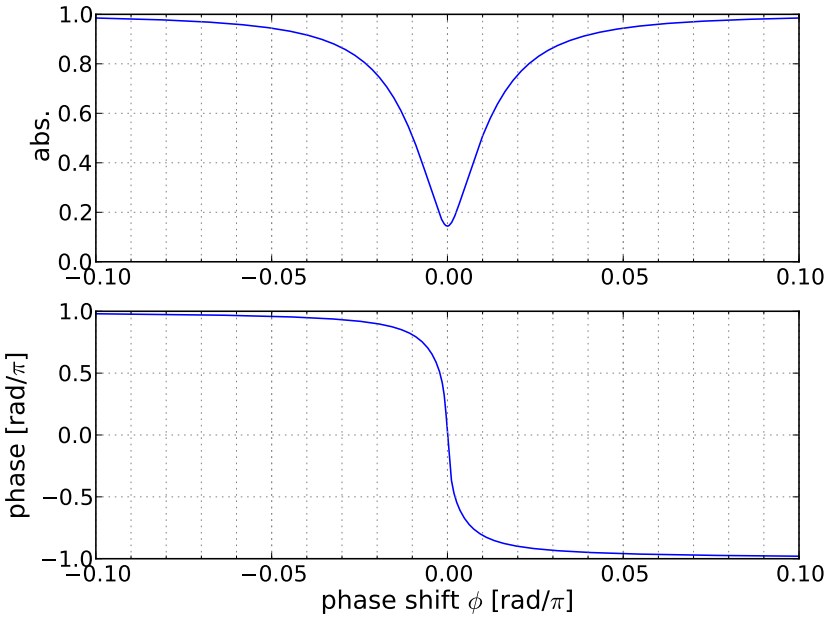

Figure C.2: Absolute value and phase of an amplitude reflectivity of an optical cavity.

However, as we can see from Eq. (C.2), we cannot distinguish if the change in ϕ is from the laser frequency change or the cavity round-trip length change. So, the fluctuation in the cavity length change is generally a noise source for frequency measurements.

C.1.2 Free spectral range and finesse

Fig. C.3 is a plot made from Eq. (C.7), and shows the change in the intensity of the transmitted light from an optical cavity, with respect to the laser frequency change. If we fix the cavity length L and change the laser frequency, the intensity of the transmitted light changes periodically. This period is called a free spectral range (FSR), and from Eq. (C.9), it is written as

$$\nu_{\mathrm{FSR}} = \frac{c}{L}. \tag{C.10}$$

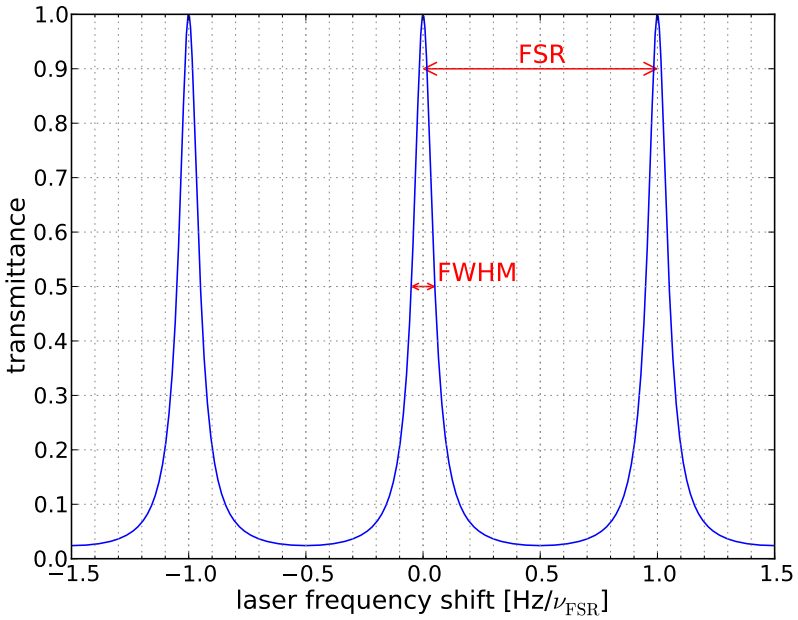

Figure C.3: Intensity of transmitted light from an optical cavity. Calculated under the conditions $r_1 = r_3$, $r_2 = 1$, and $\mathcal{F} = 10$.

Also, the full width at half maximum (FWHM) of the transmitted power peak can be obtained from Eq. (C.7), by solving

$$\frac{1}{1 + \dfrac{4r_1r_2r_3}{(1 - r_1r_2r_3)^2} \sin^2\left(\dfrac{\pi L \nu_{\mathrm{FWHM}}}{2c}\right)} = \frac{1}{2}. \tag{C.11}$$

Here, if we assume $\dfrac{\pi L \nu_{\mathrm{FWHM}}}{2c} = \dfrac{\pi \nu_{\mathrm{FWHM}}}{2\nu_{\mathrm{FSR}}} \ll 1$, we can Taylor expand sin term and

$$\nu_{\mathrm{FWHM}} \equiv \frac{c(1 - r_1r_2r_3)}{\pi L \sqrt{r_1r_2r_3}} \tag{C.12}$$

can be obtained.

The ratio between ν_{FSR} and ν_{FWHM} shows the sharpness of the resonance,

and the ratio is called a finesse. The expression of the finesse is

$$\mathcal{F} = \frac{\nu_{\mathrm{FSR}}}{\nu_{\mathrm{FWHM}}} = \frac{\pi\sqrt{r_1 r_2 r_3}}{1 - r_1 r_2 r_3}. \tag{C.13}$$

The finesse is larger, and the resonance is sharper when the reflectivities of the mirrors are close to 1. Since we usually make the finesse of the cavity sufficiently larger than 1, the assumption we made above is appropriate.

C.2 Waveplates

Waveplates are optics which transforms polarization states of laser beams by putting phase difference between two orthogonal optical axes with birefringent crystal. Half-wave plates put the phase difference of π, which corresponds to half of a wavelength. Quarter-wave plates put the phase difference of $\pi/2$, which corresponds to quarter of a wavelength. Two optical axes are called fast axis and slow axis, and a waveplate put a certain amount of phase delay to the slow axis with respect to the fast axis.

To show the behavior of waveplates, here we use Jones Calculus which Jones invented in 1941 [72]. In this method we set the amplitude of the incident electrical field to the waveplate to be

$$\boldsymbol{E}_{\mathrm{in}} = \begin{pmatrix} E^s \\ E^p \end{pmatrix}, \tag{C.14}$$

where E^s and E^p is the s-polarized and the p-polarized component, respectively. We calculate how this vector is transformed by waveplates.

If the slow axis of the waveplate is rotated by θ compared with the s-polarization axis, the transformation matrix $R(\theta)$ from the s/p-polarization basis and fast/slow basis is

$$\begin{pmatrix} E_{\mathrm{fast}} \\ E_{\mathrm{slow}} \end{pmatrix} = R(\theta) \begin{pmatrix} E^s \\ E^p \end{pmatrix} = \begin{pmatrix} \cos\theta & \sin\theta \\ -\sin\theta & \cos\theta \end{pmatrix} \begin{pmatrix} E^s \\ E^p \end{pmatrix}. \tag{C.15}$$

Half waveplates give the phase difference between fast and slow axes by π, so the transformation matrix for half waveplates in s/p-polarization basis can

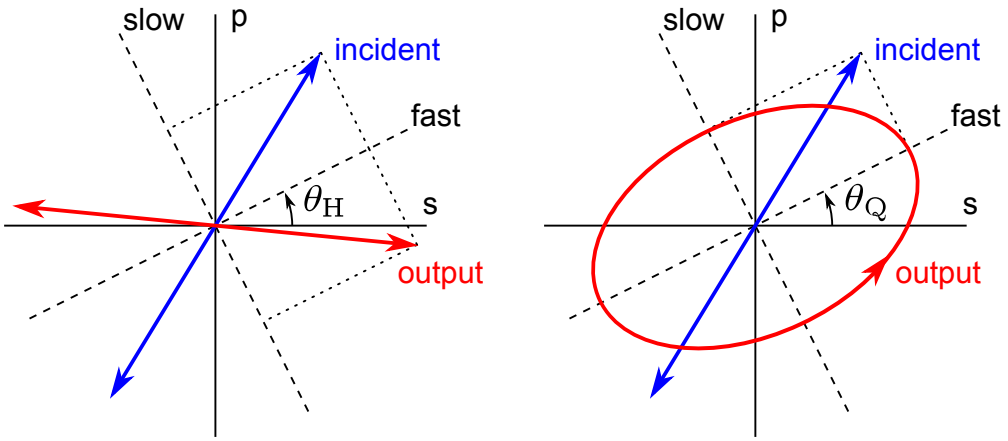

(a) Half-wave plate (b) Quarter-wave plate

Figure C.4: Transformation of polarization state with waveplates.

be written as

$$\begin{aligned} W_{\mathrm{H}}(\theta_{\mathrm{H}}) &= R^{-1}(\theta_{\mathrm{H}}) \begin{pmatrix} 1 & 0 \\ 0 & e^{-i\pi} \end{pmatrix} R(\theta_{\mathrm{H}}) \\ &= \begin{pmatrix} \cos 2\theta_{\mathrm{H}} & \sin 2\theta_{\mathrm{H}} \\ \sin 2\theta_{\mathrm{H}} & -\cos 2\theta_{\mathrm{H}} \end{pmatrix}. \end{aligned} \tag{C.16}$$

Thus, as shown in Fig. C.4(a), linearly polarized light will be transformed to line symmetric linearly polarized light where the symmetrical axis is the fast axis. Since we can rotate the fast axis freely, we can shift the polarization direction of the linearly polarized light.

Similarly, quarter waveplates give the phase difference between fast and slow axes by $\pi/2$, so the transformation matrix is,

$$\begin{aligned} W_{\mathrm{Q}}(\theta_{\mathrm{Q}}) &= R^{-1}(\theta_{\mathrm{Q}}) \begin{pmatrix} 1 & 0 \\ 0 & e^{-i\pi/2} \end{pmatrix} R(\theta_{\mathrm{Q}}) \\ &= \begin{pmatrix} \cos^2\theta_{\mathrm{Q}} - i\sin^2\theta_{\mathrm{Q}} & \sin\theta_{\mathrm{Q}}\cos\theta_{\mathrm{Q}}(1+i) \\ \sin\theta_{\mathrm{Q}}\cos\theta_{\mathrm{Q}}(1+i) & \sin^2\theta_{\mathrm{Q}} - i\cos^2\theta_{\mathrm{Q}} \end{pmatrix}. \end{aligned} \tag{C.17}$$

Although it is not obvious from the equation, as shown in Fig. C.4(b), linearly polarized light injected to a quarter-wave plate will be transformed to an el-

liptically polarized light. The two axes of the ellipse are the fast and slow axes components of the incident light.

C.3 The Hansch-Couillaud method

In order to lock the frequency of the laser to a cavity resonance, we need an error signal which is proportional to the laser frequency change and is zero at the cavity resonance. For example, the phase of the cavity reflected light as we saw in Fig. C.2 can be considered as one of candidates for this kind of signal, but photo detectors cannot directly measure the phase of the light. So, by mixing a component which is not resonant to the cavity, and by making a interference of that with the cavity reflection of the resonant light component. The cavity reflection of the resonant component has the phase information accumulated when making a round-trip inside the cavity, and we compare the phase with anti-resonant component by interference.

For the anti-resonant component, several candidates can be considered, but the HC method uses the orthogonally polarized component with respect to the resonant polarized component. This method can be used for polarization selective cavities, such as ring cavities with odd number of mirrors.

In this section, we will describe the principle of the HC method in the single-pass and double-pass configurations. We will also discuss about the advantages of the HC method over other methods.

C.3.1 Principle

In the HC method, there are several configurations for placing waveplates, but here we consider the configuration used in our experiment, as shown in Fig. C.5. The incident beam to the ring cavity is linearly polarized and the polarization direction is adjusted with the half-wave plate as

$$\boldsymbol{E}_{\mathrm{i}} = \begin{pmatrix} E_{\mathrm{i}}^{s} \\ E_{\mathrm{i}}^{p} \end{pmatrix} = \begin{pmatrix} \cos\theta \\ \sin\theta \end{pmatrix} E_0 \tag{C.18}$$

Using the amplitude reflectivity and transmissivity for s-polarized and p-polarized beam of the three mirrors, r_i^σ, and $t_i^\sigma (i = 1, 2, 3,\ \sigma = s, p)$, from

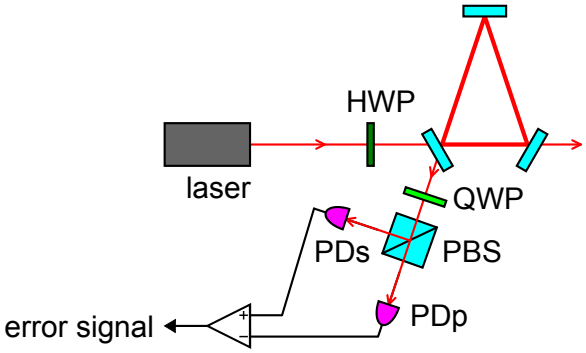

Figure C.5: Single-pass optical configuration of the Hänsch-Couillaud method.

Eq. (C.4), the amplitude reflectivities of the ring cavity are

$$r^s_{\rm cav}(\phi) = -r^s_1 + \frac{(t^s_1)^2 r^s_2 r^s_3 e^{-i\phi}}{1 - r^s_1 r^s_2 r^s_3 e^{-i\phi}} \tag{C.19}$$

$$r^p_{\rm cav}(\phi) = r^p_1 + \frac{(t^p_1)^2 r^p_2 r^p_3 e^{-i\phi}}{1 + r^p_1 r^p_2 r^p_3 e^{-i\phi}}. \tag{C.20}$$

Here, ϕ is the phase change accumulated when the beam makes a round-trip inside the cavity, and is given by Eq. (C.2). Some terms in the equations have different signs because sings of the mirror reflectivities are different between polarizations. From this reason, if the laser frequency is at the cavity resonance for s-polarized light, and thus $e^{-i\phi} \simeq 1$, the reflectivity for p-polarized light is

$$\begin{aligned} r^p_{\rm cav} &\simeq r^p_1 + \frac{(t^p_1)^2 r^p_2 r^p_3}{1 + r^p_1 r^p_2 r^p_3} \\ &= 1 - \frac{(1 - r^p_1)(1 - r^p_2 r^p_3)}{1 + r^p_1 r^p_2 r^p_3} \\ &\simeq 1. \end{aligned} \tag{C.21}$$

This means that the cavity is anti-resonant for p-polarized light.

Therefore, from this polarization selectivity, cavity reflectivity near resonance can be written as

$$\boldsymbol{E}_{\rm r} = \begin{pmatrix} E^s_{\rm r} \\ E^p_{\rm r} \end{pmatrix} = \begin{pmatrix} r^s_{\rm cav}(\phi)\cos\theta \\ r^p_{\rm cav}(\phi)\sin\theta \end{pmatrix} E_0 \simeq \begin{pmatrix} r^s_{\rm cav}(\phi)\cos\theta \\ \sin\theta \end{pmatrix} E_0. \tag{C.22}$$

If we split this beam with a polarizing beam splitter (PBS), resonant s-polarized component and anti-resonant p-polarized component do not interfere, but if we put a rotated quarter-wave plate in front of the PBS, they interfere. When the slow axis of the quarter-wave plate is tilted by $\theta_{\rm Q}$ with respect to the s-polarization axis, the transmitted light from the quarter-wave plate is

$$\boldsymbol{E}'_{\rm r} = W_{\rm Q}(\theta_{\rm Q}) \begin{pmatrix} E^s_{\rm r} \\ E^p_{\rm r} \end{pmatrix}. \tag{C.23}$$

For simplicity, here we set $\theta_{\rm Q}$ to be at the optimal point 45°. The equation above will be

$$\begin{aligned} \boldsymbol{E}'_{\rm r} &= W_{\rm Q}(\pi/4) \begin{pmatrix} E^s_{\rm r} \\ E^p_{\rm r} \end{pmatrix} \\ &= \frac{1}{2} \begin{pmatrix} (1-i)(E^s_{\rm r} + iE^p_{\rm r}) \\ (1+i)(E^s_{\rm r} - iE^p_{\rm r}) \end{pmatrix}. \end{aligned} \tag{C.24}$$

Thus, if we split this beam by a PBS and detect the s-polarization and the p-polarization components by different photo detectors, the intensity of the beam injection onto each photo diode can be written as

$$\begin{aligned} P_{\rm PDs} &= \left(\frac{1}{2}|1-i||E^s_{\rm r} + iE^p_{\rm r}|\right)^2 \\ &= P_{\rm DC} + {\rm Re}(E^s_{\rm r}(iE^p_{\rm r})^*), \end{aligned} \tag{C.25}$$

$$\begin{aligned} P_{\rm PDp} &= \left(\frac{1}{2}|1+i||E^s_{\rm r} - iE^p_{\rm r}|\right)^2 \\ &= P_{\rm DC} - {\rm Re}(E^s_{\rm r}(iE^p_{\rm r})^*). \end{aligned} \tag{C.26}$$

Here, $P_{\rm DC}$ is the DC component, and by defining $|E_0|^2 \equiv P_0$, this can be written as

$$\begin{aligned} P_{\rm DC} &= \frac{1}{2}(|E^s_{\rm r}|^2 + |E^p_{\rm r}|^2) \\ &= \frac{1}{2}P_0 \left[\frac{(r^s_2 r^s_3 - r^s_1)^2 + 4r^s_1 r^s_2 r^s_3 \sin^2(\phi/2)}{(1 - r^s_1 r^s_2 r^s_3)^2 + 4r^s_1 r^s_2 r^s_3 \sin^2(\phi/2)} \cos^2\theta + \sin^2\theta\right]. \end{aligned} \tag{C.27}$$

This DC component is not zero at at the cavity resonance $\phi = 2\pi m$, and is

$$P_{\mathrm{DC}}|_{\phi=2\pi m} = \frac{1}{2}P_0\left[\frac{(r_2^s r_3^s - r_1^s)^2}{(1 - r_1^s r_2^s r_3^s)^2}\cos^2\theta + \sin^2\theta\right]. \tag{C.28}$$

On the other hand, $\mathrm{Re}(E_{\mathrm{r}}^s(iE_{\mathrm{r}}^p)^*)$ is zero at the cavity resonance, and thus we can get the error signal which is zero at the cavity resonance by taking a differential signal of each photo detector output. This differential signal can be written down as

$$\begin{aligned} P_{\mathrm{diff}} &\equiv P_{\mathrm{PDs}} - P_{\mathrm{PDp}} \\ &= 2\mathrm{Re}(E_{\mathrm{r}}^s(iE_{\mathrm{r}}^p)^*) \\ &= -2P_0\cos\theta\sin\theta\frac{(t_1^s)^2 r_2^s r_3^s\sin\phi}{1 + (r_1^s r_2^s r_3^s)^2 - 2r_1^s r_2^s r_3^s\cos\phi}. \end{aligned} \tag{C.29}$$

Since it is always $P_{\mathrm{diff}} = 0$ when the laser frequency is prefectly locked to the cavity resonant frequency, this error signal has immunity to the laser intensity noise in principle. Also, the slope of this error signal near cavity resonance is

$$\left.\frac{\partial P_{\mathrm{diff}}}{\partial\phi}\right|_{\phi=2\pi m} = -2P_0\cos\theta\sin\theta\frac{(t_1^s)^2 r_2^s r_3^s}{(1 - r_1^s r_2^s r_3^s)^2}. \tag{C.30}$$

So, this error signal is linear to ϕ, and is suitable for the laser frequency lock. This is the principle of the HC method.

Fig. C.6 shows the actual error signal P_{diff} and the cavity transmitted beam intensity. The shape of the error signal looks like a differential of transmitted beam intensity, and we can see that the error signal is linear to ϕ near cavity resonance. We have also plotted the error signal when the angle of the quarter-wave plate θ_{Q} is not 45° in Fig. C.6. If θ_{Q} is not 45°, the error signal will not be zero at the cavity resonance. This is because the DC component of the incident beam is not canceled out by taking the differential signal of two photo detectors, and the error signal will lose its immunity to the laser intensity noise.

Also, as we can see from Eq. (C.30), the amplitude of the error signal can be changed by adjusting the polarization direction θ of the cavity incident beam with the half-wave plate. The slope of the error signal is at its maximum when

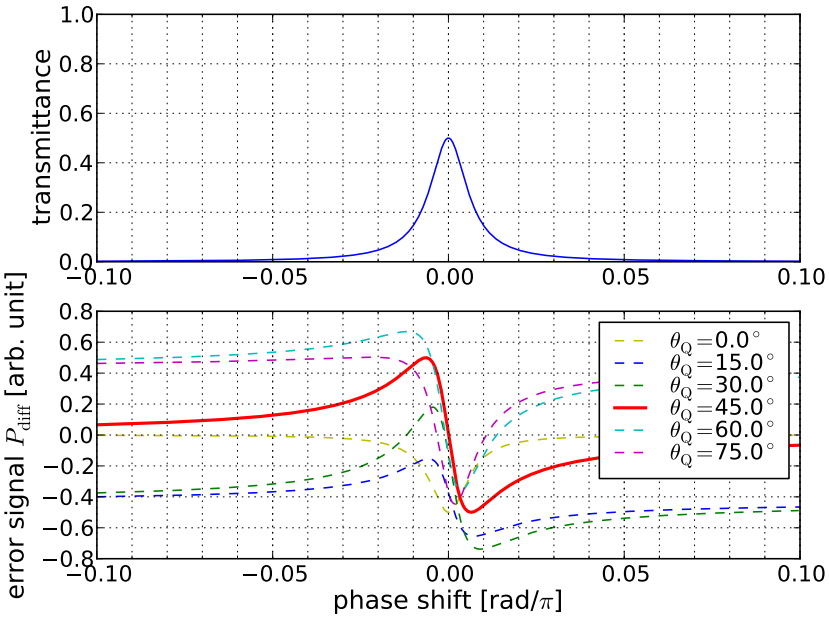

Figure C.6: Cavity transmitted beam intensity and the error signal of the Hänsch-Couillaud method.

$\theta = 45°$, which gives $\cos\theta \sin\theta = 1/2$. However, transmitted light intensity is at its maximum and reflected beam intensity is at its minimum when $\theta = 0$, and generally, signal to noise ratio is larger when θ is slightly off from zero.

Equations we show above can be used for general triangular cavities, but if we set $\theta = 45°$, and set $r_2^s = 1$ and $r_1^s = r_3^s$, as in our experiment, Eq. (C.28) and Eq. (C.30) can be simplified to

$$P_{\mathrm{DC}}|_{\phi=2\pi m} = \frac{1}{4}P_0 \tag{C.31}$$

$$\left.\frac{\partial P_{\mathrm{diff}}}{\partial\phi}\right|_{\phi=2\pi m} = \frac{1}{\pi}P_0\mathcal{F} \tag{C.32}$$

Here, $\mathcal{F}$ is the finesse for the s-polarized light and is

$$\mathcal{F} = \frac{\pi\sqrt{r_1^s r_2^s r_3^s}}{1 - r_1^s r_2^s r_3^s} = \frac{\pi r_1^s}{(t_1^s)^2}. \tag{C.33}$$

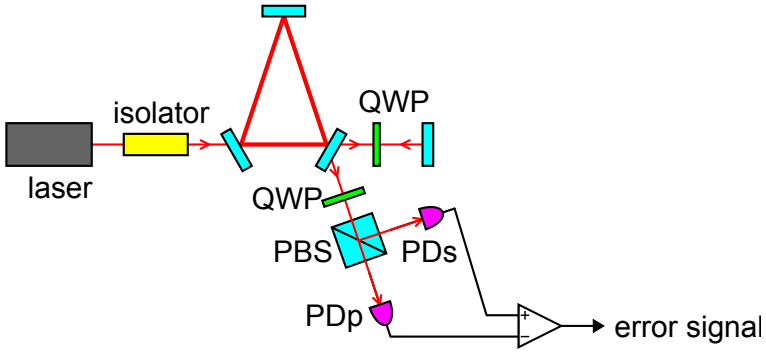

Figure C.7: Double-pass optical configuration of the Hänsch-Couillaud method.

C.3.2 Use in double-pass configuration

As we can see by comparing Eq. (C.16) and Eq. (C.17), passing through the same quarter-wave plate twice is equivalent to a half-wave plate. Thus, when applying the HC method in the double-pass configuration, placing wavelates as shown in Fig. C.7 works. From the polarization selectivity of the cavity, transmitted light is linearly polarized, but the quarter-wave plate placed in between the cavity and the reflection mirror makes anti-resonant polarization component.

C.3.3 Advantages

To acquire the error signal which is proportional to the difference between the incident laser frequency and the cavity resonant frequency, one of the most popular method is the Pound-Drever-Hall (PDH) method [73]. In the PDH method, we give phase modulation to the incident light, and use phase modulation sidebands generated for anti-resonant component. By acquiring the beat signal between this sidebands and the carrier which is resonant, the error signal can be obtained.

For PDH method, the frequencies of the sidebands should be set sufficiently away from the resonance. The cavity we used has short cavity length, and has the full width at half maximum of the resonant peak is large (12 MHz). So, the phase modulation frequency needed is as high as roughly 100 MHz, and

the PDH method is not handy for our experiment. The PDH method needs a phase modulator, a fast photo detector, and high speed op-amps, but the HC method does not.

We also used the HC method for acquiring the Lorentz violation signal with the double-pass configuration. In the double-pass configuration, we use the cavity transmitted beam which has less higher order modes for the error signal acquisition. As compared with the PDH method which deforms the spatial mode when giving a phase modulation, the HC method is especially suitable for use in double-pass configurations [39].

Note that here we use a term *mode* to say a spatial mode of a laser beam. Intensity distribution of an electrical field of a laser beam from a source is ideally Gaussian distribution in a plane perpendicular to the optical axis. This mode is called a fundamental mode, but actual laser beams are not perfectly in a fundamental mode, and has higher order modes. Optical cavities have mode selectivity when radius of curvatures of consisting mirrors and distances between mirrors are appropriately designed, since only fundamental modes resonates in those cavities. For more detailed discussion, see, for example, Refs. [53, 54].

Appendix D
Laser Frequency Actuation Efficiency Measurement

In the laser source we used in our experiment, there is a laser cavity made of a fiber, and the cavity length can be modulated with a piezoelectric transducer. In this way, we can modulate the laser frequency of the output beam. We locked the frequency of the laser to the counterclockwise resonant frequency of the ring cavity using this laser frequency actuation mechanism.

The efficiency of this laser frequency actuation, such as the change in the laser frequency per voltage put on the piezoelectric transducer can be measured with an asymmetric Michelson interferometer. Here, we present the principle of this measurement and the actual measurement result.

D.1 Asymmetric Michelson interferometer

In a Michelson interferometer, the beam from the laser source is split into two arms by a beamsplitter, and each of those is reflected by an end mirror toward the beamsplitter. Two beams are combined there and makes interference fringes depending on the phase difference.

Let's consider a Michelson interferometer shown in Fig. D.1. Using the angular frequency of the laser ω, an electric field of the incident beam can be written as

$$E_{\mathrm{in}} = E_0 e^{i\omega t}. \tag{D.1}$$

If we set the phase change accumulated when making a round trip between the beamsplitter and the mirror MX, MY, as ϕ_{x}, ϕ_{y}, respectively, the recombined

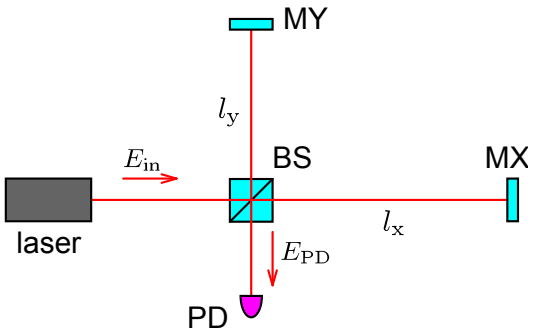

Figure D.1: Michelson interferometer.

beam onto the photo diode can be expressed as

$$E_{\mathrm{PD}} = \frac{1}{2}E_0 e^{i(\omega t - \phi_{\mathrm{x}})} - \frac{1}{2}E_0 e^{i(\omega t - \phi_{\mathrm{y}})}. \tag{D.2}$$

Here, we assumed ideal case in which the beamsplitter splits beam exactly in half, and the reflectivity of the mirrors MX and MY are 1.

The laser power on the photo diode can then be written as

$$P_{\mathrm{PD}} = |E_{\mathrm{PD}}|^2 = \frac{1}{2}P_{\mathrm{in}}(1 - \cos\phi_-). \tag{D.3}$$

Here, $\phi_- \equiv \phi_{\mathrm{x}} - \phi_{\mathrm{y}}$ and

$$\phi_- = \frac{2l_-\omega}{c} = \frac{4\pi l_-\nu}{c}, \tag{D.4}$$

where l_- is the length difference between two arms and ν is the laser frequency.

When the length difference between two arms changes by δl_-, and the laser frequency changes by $\delta\nu$, this phase difference changes by

$$\delta\phi_- = \phi_- - \frac{4\pi(l_- + \delta l_-)(\nu + \delta\nu)}{c} \simeq \frac{4\pi\delta l_-\nu}{c} + \frac{4\pi l_-\delta\nu}{c}. \tag{D.5}$$

Therefore, the change in δl_- gives P_{PD} change. This property can be used for the precise measurement of change in distances, so Michelson interferometers are used for devices such as gravitational wave detectors.

In gravitational wave detectors, we make the length difference between two

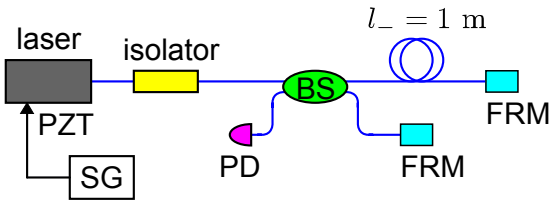

Figure D.2: The setup for measuring the actuation efficiency of the laser frequency. SG: signal generator, FRM: faraday rotator mirror.

arms to be $l_- \simeq 0$, so that the laser frequency fluctuation $\delta\nu$ does not change $P_{\rm PD}$ and affect the length measurement. However, if we intentionally make l_- to be large, $P_{\rm PD}$ changes with the laser frequency change. We used this asymmetric Michelson interferometer to measure the actuation efficiency of the laser frequency.

D.2 Measurement result

Fig. D.2 is the schematic of the setup for measuring the actuation efficiency of the laser frequency. We measured the power change in the output of the fiber made asymmetric Michelson interferometer, with respect to the voltage applied on the piezoelectric transducer in the laser source.

Assume the voltage applied on the piezoelectric transducer to be ΔV and this created the laser frequency change of $\Delta\nu$. From Eq. (D.5), the change in the phase difference between two arms $\Delta\nu$ can be written as

$$\Delta\phi_- = \frac{4\pi n l_- \Delta\nu}{c}, \tag{D.6}$$

where n is the refractive index of the fiber. One period change in $P_{\rm PD}$ correspond to the change in the phase difference of $\Delta\phi_- = 2\pi$. So, the laser frequency actuation efficiency A can be written with ΔV needed to change $P_{\rm PD}$ for one period,

$$A = \frac{\Delta\nu}{\Delta V} = \frac{c}{2nl_-}\frac{1}{\Delta V}. \tag{D.7}$$

By inserting the refractive index of the fiber $n = 1.47$, arm asymmetry intro-

duced $l_- = 1$ m, and the measured value of ΔV,

$$A = 12.9 \text{ MHz/V} \tag{D.8}$$

was obtained. This is the actuation efficiency of the laser frequency by the piezoelectric transducer in the fiber laser source we used for our experiment. The total uncertainty in this measurement is estimated to be 5% .

Appendix E
Photos of the Apparatus

Here are some photos of our experimental apparatus.

Figure E.1: The entire appearance of the apparatus. The vacuum enclosure on the turntable covered with black sheet is the main optical component, and the laser source is placed on top. Some electrical circuits and web camera are also put on the optical table. The rack on the left has the PZT driver and the data logger we used for the data acquisition. The rack on the right has the motor driver and the PC for controlling the motor for the turntable.

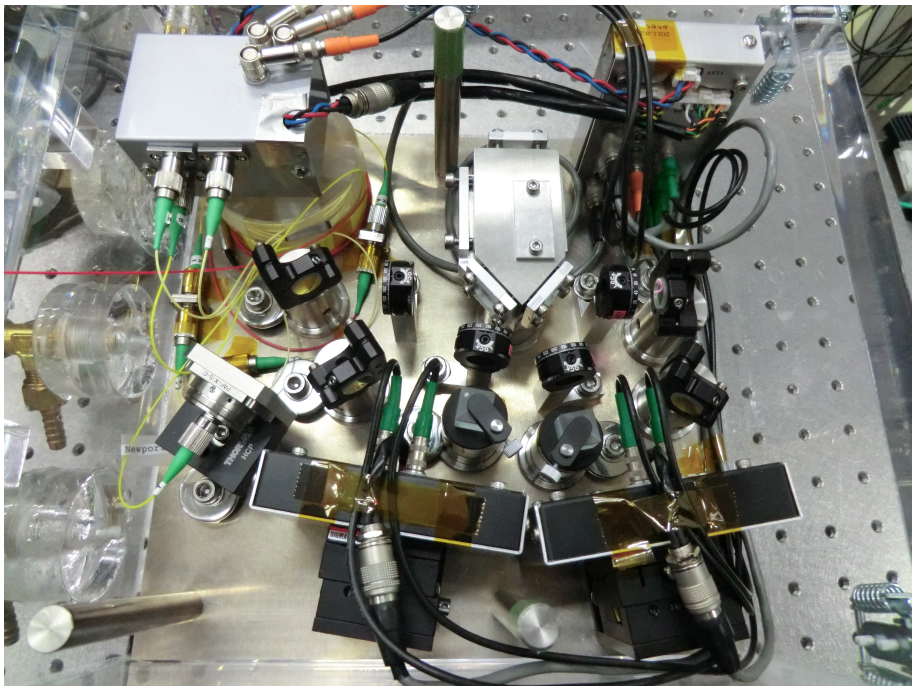

Figure E.2: Optics inside the vacuum enclosure. The fiber collimator is mounted on the left. The ring cavity with pentagonal spacer is mounted on the middle. The black box on the bottom has the photo detectors for extracting the error signals. The silver box on the top left has the photo detectors for monitoring the laser intensity. All the optics are fixed on a single aluminum plate.

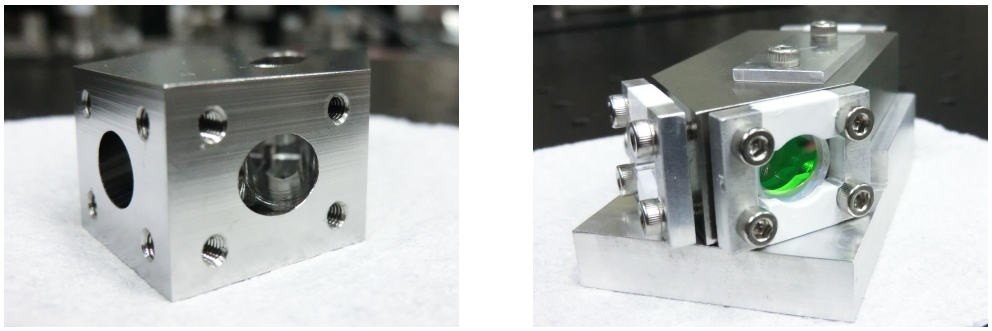

Figure E.3: The spacer and the ring cavity. The spacer made of Super Invar has holes for the optical path and for placing the silicon piece. The mirrors are fixed on the spacer with aluminum plates. The silicon piece is also fixed with a rubber and a aluminum plate on top.

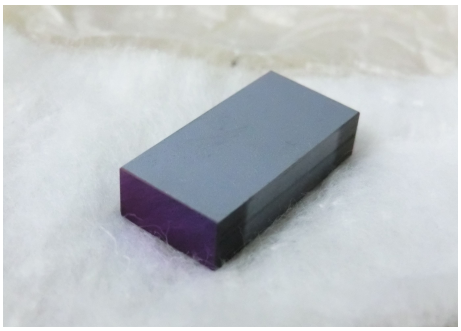

Figure E.4: The silicon piece. The edge surfaces look purple when viewed from an inclined direction because of the anti-reflection coating. Its size is $5 \times 10 \times 20$ mm, and was fabricated by Okamoto Optics.

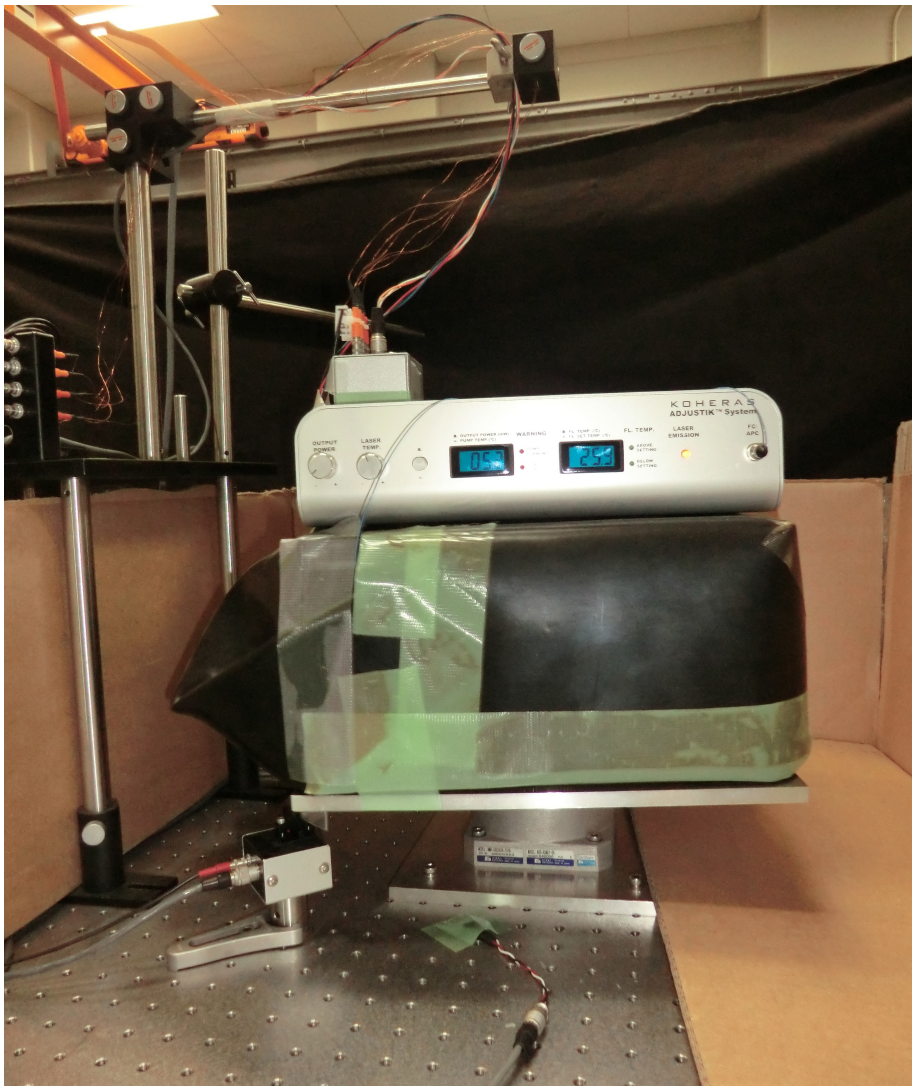

Figure E.5: The laser source, vacuum enclosure, and the turntable. The turntable was made of an aluminum plate and the motor, and it is fixed on the optical table. The vacuum enclosure with the optical setup inside is covered with a black sheet for light shielding. The laser source is placed on top of the vacuum enclosure, and the beam is fed into the enclosure with a fiber. The cables for extracting the signals and providing power are hang from the top. The little box beneath the turntable has the photo interrupter for obtaining the home signal. There is also a sensor on the optical table for monitoring the temperature.

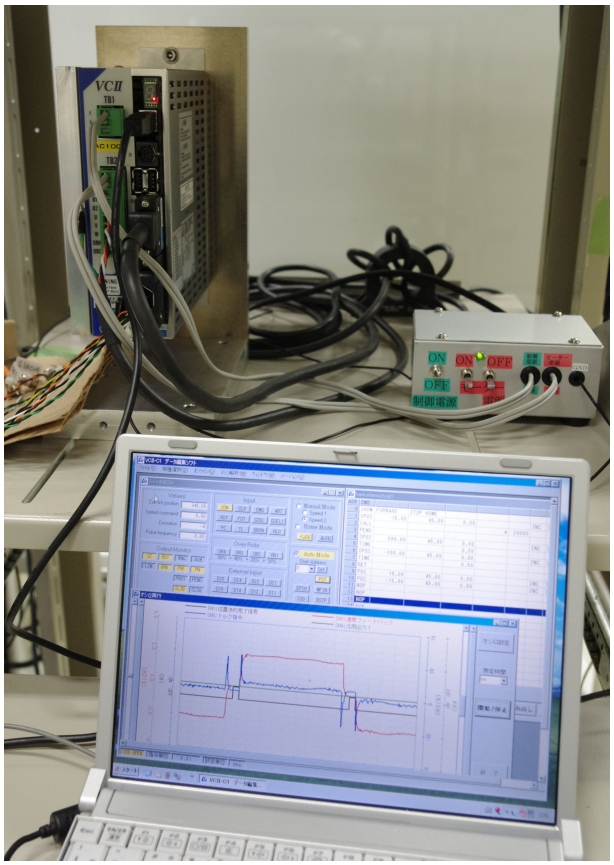

Figure E.6: The motor driver and the PC for controlling the motor. The box on the top left with a print "VCB" is the motor driver. The silver box on the right is the switching circuit for power. Application for controlling the motor and monitoring the motor signals are opened in the PC.

Bibliography

1 Introduction

[1] A. Einstein, Ann. Phys. (Leipzig) **17**, 891 (1905).
Zur Elektrodynamik bewegter Körper

[2] D. Mattingly, Living Rev. Relativity **8**, 5 (2005).
Modern Tests of Lorentz Invariance

[3] V.A. Kostelecký and N. Russell, Rev. Mod. Phys. **83**, 11 (2011); updated version available at arXiv:0801.0287.
Data Tables for Lorentz and CPT Violation

[4] V.A. Kostelecký, *Proceedings of the Sixth Meeting on CPT and Lorentz Symmetry* (World Scientific, Singapore, 2014).

[5] V. A. Kostelecký and S. Samuel, Phys. Rev. D **39**, 683 (1989).
Spontaneous Breaking of Lorentz Symmetry in String Theory

[6] V.A. Kostelecký and R. Potting, Nucl. Phys. B **359**, 545 (1991).
CPT *and strings*

[7] R. Gambini and J. Pullin, Phys. Rev. D **59**, 124021 (1999).
Nonstandard optics from quantum space-time

[8] C. H. Lineweaver, L. Tenorio, G. F. Smoot, P. Keegstra, A. J. Banday, and P. Lubin, Astrophys. J. **470**, 38 (1996).
The Dipole Observed in the COBE DMR Four-Year Data

2 Tests of Lorentz Invariance

[9] H. P. Robertson, Rev. Mod. Phys. **21** (1949) 378.
Postulate versus *Observation in the Special Theory of Relativity*

[10] R. Mansouri and R. U. Sexl, Gen. Relativ. Grav. **8**, 497 (1977).
A Test Theory of Special Relativity: I. Simultaneity and Clock Synchronization

[11] R. Mansouri and R. U. Sexl, Gen. Relativ. Grav. **8**, 515 (1977).
A Test Theory of Special Relativity: II. First Order Tests

[12] R. Mansouri and R. U. Sexl, Gen. Relativ. Grav. **8**, 809 (1977).
A Test Theory of Special Relativity: III. Second Order Tests

[13] D. Colladay and V. A. Kostelecký, Phys. Rev. D **58**, 116002 (1998).
Lorentz-violating extension of the standard model

[14] C. M. Will, Phys. Rev. D **45**, 403 (1992).
Clock synchronization and isotropy of the one-way speed of light

[15] Y. Michimura, Master Thesis, pp.7-9 (University of Tokyo, 2012).
「光リング共振器を用いた片道光速の異方性探査」(*Search for Anisotropy in the One-Way Speed of Light Using an Optical Ring Cavity*; in Japanese) http://granite.phys.s.u-tokyo.ac.jp/michimura/document/michimura_masterthesis.pdf

[16] V. A. Kostelecký and M. Mewes, Phys. Rev. D **80**, 015020 (2009).
Electrodynamics with Lorentz-violating operators of arbitrary dimension

[17] M. Hakayawa, Phys. Lett. B **478**, 394 (2000).
Perturbative analysis on infrared and ultraviolet aspects of noncommutative QED on R^4

[18] S. M. Carroll, J. A. Harvey, V. A. Kostelecký, C. D. Lane, and T. Okamoto, Phys. Rev. Lett. **87**, 141601 (2001).
Noncommutative Field Theory and Lorentz Violation

[19] H. E. Ives and G. R. Stilwell, J. Opt. Soc. Am. **28**, 215 (1938).
An experimental study of the rate of a moving atomic clock

[20] A. A. Michelson and E. W. Morley, Am. J. Sci. **34**, 333 (1887).
On the Relative Motion of the Earth and the Luminiferous Ether

[21] R. J. Kennedy and E. M. Thorndike, Phys. Rev. **42**, 400 (1932).
Experimental Establishment of the Relativity of Time

[22] A. Brillet and J. L. Hall, Phys. Rev. Lett. **42**, 549 (1979).
Improved Laser Test of the Isotropy of Space

[23] Ch. Eisele, A. Yu. Nevsky, and S. Schiller, Phys. Rev. Lett. **103**, 090401 (2009).
Laboratory Test of the Isotropy of Light Propagation at the 10^{-17} Level

[24] S. Herrmann, A. Senger, K. Möhle1, M. Nagel, E. V. Kovalchuk, and A. Peters, Phys. Rev. D **80**, 105011 (2009).
Rotating optical cavity experiment testing Lorentz invariance at the 10^{-17} Level

[25] M. E. Tobar, P. Wolf, S. Bize, G. Santarelli, and V. Flambaum, Phys. Rev. D **81**, 022003 (2010).
Testing local Lorentz and position invariance and variation of fundamental constants by searching the derivative of the comparison frequency between a cryogenic sapphire oscillator and hydrogen maser

[26] S. Reinhardt, G. Saathoff, H. Buhr, L. A. Carlson, A. Wolf, D. Schwalm, S. Karpuk, C. Novotny, G. Huber, M. Zimmermann, R. Holzwarth, T. Udem, T. W. Hänsch and G. Gwinner, Nat. Phys. **3**, 861 (2007).
Test of relativistic time dilation with fast optical atomic clocks at different velocities

[27] T. P. Krisher, L. Maleki, G. F. Lutes, L. E. Primas, R. T. Logan, J. D. Anderson, and C. M. Will, Phys. Rev. D **42**, 731 (1990).
Test of the isotropy of the one-way speed of light using hydrogen-maser frequency standards

[28] P. Wolf and G. Petit, Phys. Rev. A **56**, 4405 (1997).
Satellite test of special relativity using the global positioning system

[29] W. S. N. Trimmer, R. F. Baierlein, J. E. Faller, and H. A. Hill, Phys. Rev. D **8**, 3321 (1973).
Experimental Search for Anisotropy in the Speed of Light

[30] M. E. Tobar, P. Wolf, A. Fowler, and J. G. Hartnett, Phys. Rev. D **71**, 025004 (2005).
New methods of testing Lorentz violation in electrodynamics

[31] Q. Exirifard, Int. J. Mod. Phys. D **23**, 1450038 (2014); originally in arXiv:1010.2057.
Triangular Ring Resonator: Direct measurement of the parity-odd parameters of the photon sector of SME

[32] F. N. Baynes, A. N. Luiten, and M. E. Tobar, Phys. Rev. D **84**, 081101(R) (2011).
Testing Lorentz invariance using an odd-parity asymmetric optical resonator

[33] F. N. Baynes, M. E. Tobar, and A. N. Luiten, Phys. Rev. Lett. **108**, 260801 (2012).
Oscillating Test of the Isotropic Shift of the Speed of Light

[34] V. G. Gurzadyan *et al.*, Mod. Phys. Lett. A **20**, 19 (2005).
Probing the Light Speed Anisotropy with Respect to the Cosmic Microwave Background Radiation Dipole

[35] J.-P. Bocquet *et al.*, Phys. Rev. Lett. **104**, 241601 (2010).
Limits on Light-Speed Anisotropies from Compton Scattering of High-Energy Electrons

3 Optical Ring Cavity

[36] W. S. N. Trimmer, R. F. Baierlein, Phys. Rev. D **8**, 3326 (1973).
Anisotropic Modification of Maxwell's Equations

[37] F. Zarinetchi and S. Ezekiel, Opt. Lett. **11**, 6 (1986).
Observation of lock-in behavior in a passive resonator gyroscope

[38] B. J. Cusack, D. A. Shaddock, B. J. J. Slagmolen, G. de Vine, M. B. Gray, D. E. McClelland, Class. Quantum Grav. **19**, 1819 (2002).
Double pass locking and spatial mode locking for gravitational wave detectors

[39] Noriaki Ohmae, Doctoral Thesis, pp.58-69 (University of Tokyo, 2011).
Laser System for Second-Generation Gravitational-Wave Detectors

[40] N. Mio,『重力波をとらえる』edited by T. Nakamura, N. Mio, M. Ohashi, p.210 (Kyoto University Press, 1998).

[41] G. Sagnac, C. R. Acad. Sci. Paris **157**, 708 (1913).
The demonstration of the luminiferous aether by an interferometer in uniform rotation

[42] R. Wang, Y. Zheng, and A. Yao, Phys. Rev. Lett. **93**, 143901 (2004).
Generalized Sagnac Effect

[43] E. J. Post, Rev. Mod. Phys. **39**, 475 (1967).
Sagnac Effect

[44] P. R. Saulson, *Fundamentals of Interferometric Gravitational Wave Detectors*, p.127 (World Scientific, Singapore, 1994).

[45] H. B. Callen, T. A. Welton, Phys. Rev. **83**, 34 (1951).
Irreversibility and Generalized Noise

[46] T. Ushiba, Master Thesis, p.13 (University of Tokyo, 2013).
「低温シリコン光共振器を用いた高安定化光源の開発」(*Development of Highly Stabilized Laser using a Cryogenic Silicon Cavity*; in Japanese)
http://granite.phys.s.u-tokyo.ac.jp/theses/ushiba_m.pdf

[47] K. Numata , A. Kemery, and J. Camp, Phys. Rev. Lett. **93**, 250602 (2004).
Thermal-Noise Limit in the Frequency Stabilization of Lasers with Rigid Cavities

[48] N. Nakagawa, A. M. Gretarsson, E. K. Gustafson, and M. M. Fejer, Phys. Rev. D **65**, 102001 (2002).
Thermal noise in half-infinite mirrors with nonuniform loss: A slab of excess loss in a half-infinite mirror

[49] G. Cagnoli, L. Gammaitoni, J. Kovalik, F. Marchesoni, M. Punturo, Phys. Lett. A **255**, 230 (1999).
Low-frequency internal friction in clamped-free thin wires

[50] Matweb http://www.matweb.com/

[51] J. Komma, C. Schwarz, G. Hofmann, D. Heinert, and R. Nawrodt, Appl. Phys. Lett. **101**, 041905 (2012).
Thermo-optic coefficient of silicon at 1550 nm and cryogenic temperatures

[52] A. Sekiya, Master Thesis, p.36 (University of Tokyo, 2000).
「空間の等方性検証実験」 (*Experimental Test of Isotropy of Space*; in Japanese) http://granite.phys.s.u-tokyo.ac.jp/theses/sekiya_m.pdf

4 Experimental Setup

[53] S. Moriwaki, 『重力波をとらえる』 edited by T. Nakamura, N. Mio, M. Ohashi, p.339-361 (Kyoto University Press, 1998).

[54] H. Kogelnik and T. Li, Proc. IEEE **54**, 1312 (1966).
Laser Beams and Resonators

[55] S. Taniguchi, TAMA300 Report (1998).
「アナログ信号光伝達システムの性能評価」 (*Performance evaluation for the optical transport system of analog signals*; in Japanese) http://tamago.mtk.nao.ac.jp/tama/recom/general_lib/ADDA/houkoku.pdf

5 Data Analysis

[56] V. A. Kostelecký and M. Mewes, Phys. Rev. D **66**, 056005 (2002).
Signals for Lorentz violation in electrodynamics

[57] Time and Date of Vernal Equinox http://aom.giss.nasa.gov/srvernal.html.

6 Conclusion

[58] A. M. Nobili, M. Shao, R. Pegna, G. Zavattini, S. G. Turyshev, D. M. Lucchesi, A. De Michele, S. Doravari, G. L. Comandi, T. R. Saravanan, F. Palmonari, G. Catastini, and A. Anselmi, Class. Quantum Grav. **29**, 184011 (2012).

'Galileo Galilei' (GG): space test of the weak equivalence principle to 10^{-17} *and laboratory demonstrations*

[59] P. Amaro-Seoane *et al.*, GW Notes **6**, 4 (2013).
eLISA: Astrophysics and cosmology in the millihertz regime

[60] S. Kawamura *et al.*, Class. Quantum Grav. **28**, 094011 (2011).
The Japanese space gravitational wave antenna:DECIGO

[61] E. J. Elliffe, J. Bogenstahl, A. Deshpande, J. Hough, C. Killow, S. Reid, D. Robertson, S. Rowan, H. Ward, and G. Cagnoli, Class. Quantum Grav. **22**, S257 (2005).
Hydroxide-catalysis bonding for stable optical systems for space

[62] J. A. Lipa, S. Wang, J. Nissen, M. Kasevich, and J. Mester, Int. J. Mod. Phys. D **16**, 2393 (2007).
Detecting Lorentz invariance violations in the 10^{-20} *range*

A Standard Model Extension

[63] M. Mewes, Phys. Rev. D **85**, 116012 (2012).
Optical-cavity tests of higher-order Lorentz violation

[64] V. A. Kostelecký and M. Mewes, Phys. Rev. Lett. **110**, 201601 (2013).
Constraints on Relativity Violations from Gamma-Ray Bursts

[65] V. Vasileiou, A. Jacholkowska, F. Piron, J. Bolmont, C. Couturier, J. Granot, F. W. Stecker, J. Cohen-Tanugi, and F. Longo, Phys. Rev. D **87**, 122001 (2013).
Constraints on Lorentz invariance violation from Fermi*-Large Area Telescope observations of gamma-ray bursts*

[66] S. R. Parker, M. Mewes, P. L. Stanwix, and M. E. Tobar, Phys. Rev. Lett. **106**, 180401 (2011).
Cavity Bounds on Higher-Order Lorentz-Violating Coefficients

[67] P. L. Stanwix, M. E. Tobar, P. Wolf, C. R. Locke, and E. N. Ivanov, Phys. Rev. D **74**, 081101(R) (2006).

Improved test of Lorentz invariance in electrodynamics using rotating cryogenic sapphire oscillators

[68] A. A. Abdo *et al.*, Nature **462**, 331 (2009).
A limit on the variation of the speed of light arising from quantum gravity effects

B Feedback Control

[69] T. Katayama, 『新版 フィードバック制御の基礎』(Asakura Publishing, 2002)

C Optical Cavities and Hansch-Couillaud Method

[70] T. W. Hänsch and B. Couillaud, Opt. Commun. **35**, 441 (1980).
Laser frequency stabilization by polarization spectroscopy of a reflecting reference cavity

[71] S. Moriwaki, T. Mori, K. Takeno, and N. Mio, Appl. Phys. Express **2**, 016501 (2009).
Frequency Discrimination Method Making Use of Polarization Selectivity of Triangular Optical Cavity

[72] R. Clark Jones, J. Opt. Soc. Am. **31**, 488 (1941).
A New Calculus for the Treatment of Optical Systems

[73] R. W. P. Drever, J. L. Hall, F. V. Kowalski, J. Hough, G. M. Ford, A. J. Munley, and H. Ward, Appl. Phys. B **31**, 97 (1983).
Laser phase and frequency stabilization using an optical resonator